

Republic of Iraq
Ministry of Higher Education
& Scientific Research
University of Babylon
College of Education for Pure Sciences
Department of Physics



Efficient of Graphene Oxide-Based Hybrid Nanocomposites for Physical and Biological Applications

A Thesis

Submitted to the Council of the College of Education for Pure Sciences,
University of Babylon in Partial Fulfillment of the Requirements for the Degree of
Master in Education / Physics

By

Rand Waleed Abdul –Sada Hassan

B.Sc. in physics

(University of Babylon, 2022)

Supervised by

Prof. Dr. Ehssan Dhiaa Jawad Al-Bermany

2025 A.D.

1447 A.H.

بِسْمِ اللَّهِ الرَّحْمَنِ الرَّحِيمِ

يَرْفَعُ اللَّهُ الَّذِينَ آمَنُوا مِنْكُمْ وَالَّذِينَ

أُوتُوا الْعِلْمَ دَرَجَاتٍ

صدق الله العلي العظيم

(سورة المجادلة الآية ١١)

Acknowledgements

*In the name of God, the Most Gracious, the Most Merciful, I praise God, Lord of the earth and the heavens, for completing my research. I extend my thanks and gratitude to my supervisor, **Professor Dr. Ehssan Dhiaa Jawad Al-Bermany** who contributed his abundant knowledge, valuable time, sincere assistance, distinguished efforts, and sound advice and guidance, which helped me overcome all the difficulties I faced while preparing this thesis.*

I thank the Deanship of the College of Education for Pure Sciences at the University of Babylon and the Department of Physics for giving me this opportunity to complete my research. I also extend my sincere thanks to all the professors, instructors, and students in the Physics Department for their assistance.

Finally, I would like to extend my sincere thanks to Dr. Rawaa Adil Abdul-Nabi for her assistance in resolving the difficulties I encountered during my work, and to everyone who assisted me in preparing this thesis. I wish everyone success and prosperity.

And

Dedication

*To the one whose name I proudly carry, to the one who
paved the way for my learning, my dear father.*

To the tender heart and sincere prayers, my dear mother.

To my dear brother.

To my supervisor

Professor Dr. Ehssan Dhiaa Jawad Al-Bermany

And to everyone who has helped me...

With my deepest respect.

Rand...✍

Supervisor's Certification

I certify that the preparation of this dissertation, entitled "*Efficient of Graphene Oxide-Based Hybrid Nanocomposites for Physical and Biological Applications*" by "*Rand Waleed Abdul –Sada Hassan*" under my supervision at the College of Education for Pure Sciences University of Babylon as partial fulfillment of the requirement for the Degree Master in Education / Physics.

Signature:

Name: Dr. Ehssan Dhiaa Jawad Al-Bermany

Title: Professor

Address: University of Babylon

College of Education for Pure Sciences

Date: / / 2025

Head of the Department Certificate

In view of the available recommendations, I forward this dissertation for debate by the examining committee.

Signature:

Head of Physics Department:

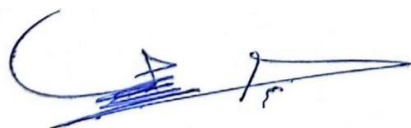
Prof. Dr. Ahmed Hashim Mohaisen

Date: / / 2025

Certification of Scientific Expert

I certify that I have read the scientific content of this dissertation " *Efficient of Graphene Oxide -Based Hybrid Nanocomposites for Physical and Biological Applications*" and I have approved this dissertation is qualified for debate.

Signature:



Name: Dr. Saleem Azara Hussain

Title: Professor

Address: University of Al-Qadisiyah

Date: 23 / 6 / 2025

Certification of Scientific Expert

I certify that I have read the scientific content of this dissertation "*Efficient of Graphene Oxide-Based Hybrid Nanocomposites for Physical and Biological Applications*" and I have approved this dissertation is qualified for debate.



Signature:

Name: Dr. Aref Saleh Baron

Title: Professor

Address: University of Al-Kafeel

Date: 23 / 6 / 2025

Certification of linguistic Expert

I certify that I have read this dissertation entitled "*Efficient of Graphene Oxide-Based Hybrid Nanocomposites for Physical and Biological Applications*" and corrected its grammatical mistakes; therefore, it has qualified for debate.

Signature:



Name: Dr. Rafel Hassoon Ubaid

Title: Assist Professor

Address: University of Babylon / College of Education / Department of English

Date: 23 / 6 / 2025

SUMMARY

In this study work, novel hybrid nanocomposites were developed based on a K30 poly vinylpyrrolidone (PVP) matrix blended with polypyrrole (PPY), a conductive polymer, and reinforced with graphene oxide (GO) and indium tin oxide (ITO) nanoparticles. Samples containing polymer ratios were prepared, representing 90% PVP and 10% PPY. To enhance the properties of the blended polymer, 1% GO nanoparticles were first introduced, followed by the addition of hybrid nanomaterials comprising GO and ITO nanosheets at 1% each. These nanocomposites (NCs) were fabricated using a solution casting technique, with the dispersion process enhanced by mechanical stirring and ultrasonication.

The samples were studied using several analytical techniques, where it was revealed Fourier transform infrared (FTIR) analysis results of the sample films showed strong physical interactions. X-ray diffraction (XRD) demonstrated the quasicrystalline behavior of PVP, which was strongly influenced by the contribution of nanoparticles. Field-emission scanning electron microscopy (FESEM) images demonstrated a homogeneous surface and excellent dispersion of nanoparticles within the polymer matrix. UV-Vis spectroscopy results showed a significant improvement in absorbance, increasing from 0.06 to 0.85 after the contribution of GO-ITO nanoparticles to the blended polymers, demonstrating the effectiveness of using two nanoparticles instead of one. The optical energy gap decreased significantly from 3.43 to 1.63 eV for the allowed indirect transitions and from 3.21 to 0.62 eV for the forbidden indirect transitions. The absorption coefficient, refractive index, extinction coefficient, real and imaginary dielectric constant, and photoconductivity were improved by adding goat indium tin oxide (GO-ITO) nanoparticles to the blended polymers. The AC dielectric constant, loss, and conductivity were measured in different frequency ranges, revealing significant

improvements. The dielectric constant improved significantly from 2.16 to 4.63, and the AC electrical conductivity improved significantly from 1.31×10^{-11} to 4.64×10^{-11} S. cm⁻¹.

The potential of the developed nanocells was studied in three main applications, in a sensing system for ammonia (NH₃) reduction and oxidation nitrogen dioxide (NO₂) gases with a sensitivity of up to 25% after the addition of conductive PPY polymers and nanomaterials, which provide excellent adsorption sites for gas molecules. Furthermore, the well-dried solid membranes exhibited superior antibacterial activity, with inhibition zones increasing by 53.8% against *Staphylococcus aureus* and 46.1% against *Escherichia coli*. Electrochemical studies (cyclic voltammetry (CV) and electrochemical impedance spectroscopy (EIS)) indicated that the PVP-PPY/GO-ITO NCs biosensor exhibited exceptional performance in the non-enzymatic detection of urea. A pronounced response was observed after the addition of 0.1 M urea biosolvent, characterized by a significant increase in redox currents and a sharp decrease in resistance values, especially at a nanocomposite concentration of 15 mg/L. These results highlight the novelty and multifunctionality of the developed NCs, showing strong potential in flexible optoelectronic devices, antibacterial coatings, tissue engineering, and sensing applications, addressing current societal needs in the health, environmental, and medical sectors.

List of Contents

Subject		Page
Summary		I
List of Contents		III
List of Figures		IX
List of Tables		XIII
List of Symbols		XV
List of Abbreviations		XIX
Chapter One: Introduction and Literature Survey		
1.1	Introduction	1
1.2	Literature Survey	5
1.3	Aims of the Work	12
Chapter Two: Theoretical Part		
2.1	Introduction	13
2.2	Polymers	13
2.2.1	Classification of polymers	14
2.2.2	Crystallinity of Polymers	15
2.2.3	Conductive polymers	16

2.2.4	Preparation of polymers	19
2.2.5	Polymer Blends	19
2.3	Nanocomposites(NCs) and Their Applications	20
2.4	The Raw Materials	21
2.4.1	Polyvinyl pyrrolidone (PVP)	21
2.4.2	Polypyrrole (PPY)	22
2.4.3	Indium tin oxide (ITO)	24
2.4.4	Graphene oxide (GO)	26
2.5	Solvents	27
2.6	Characterizations	27
2.6.1	Fourier transform infrared (FTIR) spectroscopy	27
2.6.2	X-ray diffraction (XRD)	29
2.6.3	Field emission scanning electron microscope (FE-SEM)	31
2.7	Properties of samples	32
2.7.1	Optical Properties	32
2.7.1.1	Absorbance (A) and transmittance (T)	33
2.7.1.2	Absorption coefficient (α)	34
2.7.1.3	The fundamental absorption edge	34
2.7.1.4	The electroinc transitions	35
2.7.1.5	Refractive index (n)	37

2.7.1.6	Extinction coefficient (k_o)	37
2.7.1.7	Dielectric constant (ϵ)	38
2.7.1.8	Optical conductivity (σ_{op})	38
2.7.2	Electrical properties	38
2.7.2.1	Alternating current electrical conductivity (A.C)	39
2.8	Applications	41
2.8.1	Gas sensor	41
2.8.1.1	The adsorption mechanism	43
2.8.1.2	Ammonia gas NH_3	44
2.8.1.3	Nitrogen dioxide gas NO_2	45
2.8.1.4	Sensitivity	45
2.8.1.5	Response and recovery times	46
2.8.2	Antibacterial effect systems	47
2.8.2.1	Escherichia coli (<i>E. coli</i>)	49
2.8.2.2	Staphylococcus aureus (<i>S. aureus</i>)	49
2.8.3	Biosensors and their applications	50
2.8.3.1	Urea	51
Chapter Three: Experimental		
3.1	Introduction	53
3.2	The Utilized Materials	54

3.2.1	Polypyrrole (PPY)	54
3.2.2	Polyvinyl Pyrrolidone (PVP)	54
3.2.3	Indium tin oxide nanoparticles (ITO)	54
3.2.4	Graphene oxide (GO)	54
3.3	preparation of the nanocomposites (NCs)	54
3.4	Characterizations	57
3.4.1	Fourier-transform infrared spectroscopy (FTIR)	57
3.4.2	UV-visible spectrophotometer (UV-Vis.)	57
3.4.3	X-Ray diffraction (XRD)	57
3.4.4	Field emission scanning electron microscope (FE-SEM)	57
3.4.5	Measurements of A.C. electrical properties	58
3.5	Applications	58
3.5.1	Gas sensing applications	58
3.5.2	Antibacterial activity	60
3.5.3	Urea biosensor	61
Chapter Four: Results, Discussion and Conclusions		
4.1	Introduction	64
4.2	Structure properties	64
4.2.1	Morphological properties	64
4.2.2	FTIR measurement	67

4.2.3	X-Ray diffraction measurement	68
4.3	Optical properties	71
4.3.1	Absorbance	71
4.3.2	Transmittance	74
4.3.3	Absorption coefficient	75
4.3.4	Optical energy gap	76
4.3.5	Refraction index	80
4.3.6	The Extinction coefficient	81
4.3.7	The real and imaginary dielectric constant	82
4.3.8	Optical conductivity (σ_{op})	85
4.4	The A.C electrical properties	86
4.4.1	dielectric constant	86
4.4.2	The Dielectric loss	88
4.4.3	Electrical conductivity	89
4.5	Applications	91
4.5.1	Oxidizing NO ₂ gas and reducing NH ₃ gas sensing	91
4.5.2	Antibacterial activity	100
4.5.3	Urea biosensor	103
4.5.3.1	Cyclic voltametry properties (CV)	103
4.5.3.2	Electrochemical impedance spectroscopy [EIS]	108

Chapter Five: Conclusion and Future Works		
5.1	Conclusion	112
5.2	Future Works	114
	References	115

List of Figures

No.	Caption	Page
Chapter Two: Theoretical Part		
(2-1)	Polymer chains come in a variety of shapes and sizes.	15
(2-2)	The crystallinity region in the polymers	16
(2-3)	Alternation of double and single bonds in Poly pyrrole.	17
(2-4)	Diagram illustrating the band gap energy model for insulators, semiconductors, and conductors.	19
(2-5)	The chemical structure of polyvinyl pyrrolidone (PVP) .	21
(2-6)	The chemical structure of Polypyrrole (PPY).	23
(2-7)	The ITO model with a 9:1 ratio: Atomic distribution of Indium, Tin, and Oxygen.	25
(2-8)	The chemical structure of graphene, GO, and rGO.	26
(2-9)	Types of molecular vibrations	29
(2-10)	Bragg's Diffraction.	31
(2-11)	Ray Diagram for a system of FE- SEM	32
(2-12)	Absorption edge variation with absorption regions.	35
(2-13)	Classifications of electronic transitions.	36

(2-14)	A diagram showing the gas sensing mechanism of an n-type and p-type metal oxide semiconductor in the presence of a reducing gas.	42
(2-15)	A diagram illustrating the metal oxide thin film gas sensor mechanism.	43
(2-16)	The chemoreceptive response curve.	46
(2-17)	Schematic representation of the three different GO antibacterial mechanisms of action.	48
(2-18)	Schematic of the electrochemical biosensing system.	51
(2-19)	The chemical structure of Urea.	52
Chapter Three: Experimental Part		
(3-1)	Scheme of experimental part.	53
(3-2)	Samples preparation steps in this study.	56
(3-3)	The diagram of the structures of gas sensors(a), and (b) gas sensor system.	59
(3-4)	Evaluation of the inhibition activity of the Nanoantigen using the agar disk diffusion method.	61
(3-5)	Diagram for connecting electrochemical screen-printed electrode(A), and steps of setting up and connecting electrochemical cell(B).	63
Chapter Four: Results, Discussions and Conclusions		
(4-1)	FE-SEM images of samples with two different magnifications (left-microsize) and (right-nanosize).	65
(4-2)	samples FTIR spectra at the wavenumber.	68
(4-3)	XRD patterns for the samples.	70

(4-4)	The Absorbance Spectra with the Wavelength of S1 to S4 Nanocomposite.	74
(4 -5)	The transmittance spectra of the samples.	75
(4-6)	The relation between photon energy and the absorption coefficient of samples.	76
(4-7)	The optical energy band gap $(\alpha h\nu)^{1/2}$ of allowed indirect transition for samples versus E_{ph} .	78
(4-8)	The energy band gap $(\alpha h\nu)^{1/3}$ of the forbidden indirect transition for samples versus E_{ph} .	78
(4-9)	The refractive index (n) of S1-S4.	81
(4-10)	Extinction coefficient versus wavelength for samples S1-S4.	82
(4-11)	Real dielectric constant with wavelength for samples.	84
(4-12)	Imaginary dielectric constant with wavelength for samples.	84
(4-13)	Optical conductivity with the incident photon wavelength for samples.	86
(4-14)	The dielectric constant versus (a) frequency and (b) impact of PPY, GO, and GO@ITO nanomaterials in nanocomposites .	88
(4-15)	Dielectric loss versus (a) frequency and (b) impact of PPY, GO, and GO@ITO nanomaterials in nanocomposites .	89
(4-16)	Electrical conductivity versus (a) frequency and (b) impact of PPY, GO, and GO@ITO nanomaterials in nanocomposites at 100 Hz.	90

(4-17)	Resistance changes versus time of PVP-PPY/GO@ITO sensor upon exposure to NH ₃ gas at various operating temperatures RT, 150 and 250 °C.	92
(4-18)	Resistance changes versus time of PVP-PPY/GO@ITO sensor upon exposure to NO ₂ gas at various operating temperatures RT, 150 and 250 °C.	94
(4-19)	The sensitivity versus the various operating temperatures 25, 150 °C, and 250 °C.	97
(4-20)	Images of the inhibition zones of (A) E. coli and (B) S. aureus, and (C) comparison diagram of results for samples.	101
(4-21)	Mechanism of bacterial inhibition by PVP-PPY/GO-ITO nanocomposite via light-induced ROS generation (According to UV-Vis and FTIR peaks). 102	103
(4-22)	Cyclic voltammetry analysis of electrode modified with different ratios of PVP-PPY/GO-ITO nanocomposite before adding urea.	105
(4-23)	Cyclic voltammetry analysis of an electrode modified with different concentrations of PVP-PPY/GO-ITO nanocomposites after adding a 0.1 M concentration of urea.	107
(4-24)	Nyquist plots of electrochemical isotherm (EIS) analysis of PVP-PPY/GO composite on ITO substrate with different masses A. 5 mg/L, B. 10 mg/L, C. 15 mg/L showing the change in the isotherm response before and after adding urea at a concentration of 0.1 M.	110

List of Tables

No.	Title	No.
Chapter Two: Theoretical Part		
(2-1)	Physical and chemical properties of polyvinyl pyrrolidone (PVP)	22
(2-2)	Shows physical and chemical properties of Poly pyrrole (PPY)	23
(2-3)	Physical properties of ITO	25
(2-4)	The resistance of a semiconductor when exposed to oxidation or reduction gases	42
Chapter Three: Experimental Part		
(3-1)	shows the sample preparation ratio	56
Chapter Four: Results, Discussions and Conclusions		
(4-1)	Energy gap of the indirect allowed and forbidden transitions for the samples.	79
(4-2)	Optical conductivity values at short, medium, and high wavelengths.	85
(4-3)	Sensitivity, response time and recovery of the S4 nanocomposite sensor cell at three temperatures based on exposure to NO ₂ and NH ₃ gases.	98

(4-4)	Presented a comparison of the results between literatures used the similar nanomaterials and nanocomposites used the same materials in this study.	99
(4-5)	Peak values of current and voltage for the electrode modified with PVP–PPY/GO-ITO nanocomposite concentrations before adding urea.	105
(4-6)	Peak current and voltage values for an electrode modified with different concentrations of PVP-PPY/GO-ITO nanocomposites after adding a 0.1 M concentration of urea.	107

List of Symbols

Symbol	Physical Meanings	Unites
A	Absorbance	%
A_a	Area	cm ²
a	Lattice constants	-
B	constant depending on the type of material	-
β	Full width at half maximum (FWHM)	radian
c	Speed of light	m/s
C_o	Capacitance vacuum	F
C_p	Capacitance	F
D	Crystallite size	nm
D'	The dispersion Factor	-
d	The distance between widened plates	-
E	Energy	eV
E_{ph}	Energy of phonon	eV
F	Frequency	HZ
h	Planck's constant	J. s
I	Electrical current	A
I_p	Conduction current	A

Symbol	Physical Meanings	Unites
I_A	Absorbed light intensity	Lux
I_o	The incident intensity of light	Lux
I_q	Capacitate current	A
k_o	Extinction coefficient	-
M	The linear absorption coefficient	cm^{-1}
N	Complex refractive Index	-
n	Refractive index	-
n	Diffraction rating	-
N_o	Number of transmitted particles	-
ρ	Density	g/mL
r	Exponential constant	-
R	Reflectance	-
R_P	Parallel resistance	Ohm
R_v	Volume electrical resistance	Ohm
S	Sensitivity	%
t	The thickness of the film	μm
T	Transmittance	-
T_g	Glass transition temperature	$^{\circ}\text{C}$
T_m	Melting temperature	$^{\circ}\text{C}$

Symbol	Physical Meanings	Unites
V_m	Maximum voltage	V
V	Voltage	-
W	Weight of the sample	g
Z	Total prohibition	ohm
α	Absorption coefficient	cm^{-1}
ν	Photon frequency	Hz
ϵ_0	Vacuum permittivity	F/cm
I_T	Light transmission intensity	Lux
d_{hkl}	Distance to miller	Å
E_g^{OPT}	Optical energy gap	eV
σ_{ac}	Electrical conductivity	S/cm
ΔK	Wave number	cm^{-1}
ϵ	Complex dielectric constant	-
ϵ''	Dielectric loss Factor	-
ϵ_i	Imaginary dielectric constant	-
ϵ_r	Real dielectric constant	-
$\hat{\epsilon}$	Dielectric constant	-
λ	Wavelength of light	nm

Symbol	Physical Meanings	Unites
μ_m	The mass absorption coefficient	cm^2/g
σ_{op}	Optical conductivity	S^{-1}
$(\alpha h\nu)^{1/2}$	Allowed indirect transition	$\text{cm}^{-1}.\text{eV}^{1/2}$
$(\alpha h\nu)^{1/3}$	Forbidden indirect transition	$\text{cm}^{-1}.\text{eV}^{1/3}$
$\chi^{1/2}$	The half-thickness	cm
θ	The incident angles	Degree
ω	Angular frequency	Rad. s^{-1}
δ	Dielectric loss angle	-

List of Abbreviations

Abbreviations	Physical Meanings
AC	Alternating current
B	blend polymers
CB	Conductive band
CV	Cyclic voltammetry
E.coli	Escherichia coli
EIS	Electrochemical Impedance Spectroscopy
E_{pa}	Oxidation peak potential
E_{pc}	Reduction peak potential
FE-SEM	Field emission scanning electron microscope
FTIR	Fourier transform infrared
GO	Graphene oxide
IR	Infrared
I_{pa}	Oxidation peak current
I_{pc}	Reduction peak current
ITO	Indium tin oxide
MW	Molecular weights
NO₂	Nitrogen dioxide
NPS	Nanoparticles
PPY	Polypyrrole
PVP	Poly Vinyl pyrrolidone
ROS	Reactive Oxygen Species
RT	Room Temperature

S1	Pure PVP polymer solution
S2	PVP + PPY polymer blend solution
S3	Nanocomposites with 1% of GO
S4	Nanocomposite containing 1% of GO and 1% of ITO
<i>S aureus</i>	Staphylococcus aureus
UV	Ultraviolet spectrum
VB	Valence band
Vis	Visible
XRD	X-Ray diffraction

Chapter One

Introduction and Literature Survey

1.1 Introduction

Hybrid materials have recently demonstrated trends to overcome challenges and weaknesses and enhance their properties for advanced applications compared to their original materials or individual components[1]. Researchers are increasingly blending known polymers or hybrid nanomaterials to create new matrix properties. Different types and more than two polymers have been used to blend polymers to modify their structures and enhance the properties of the blend or matrix for unique applications such as biological applications, solar cells, medical devices, optical filters, sensors, etc. [2].

Conductive polymers are being extensively researched for their exceptional properties, such as electrical and optical tunability, high mechanical strength, ease of fabrication, and better environmental stability compared to traditional inorganic materials [3]. Although there are some limitations in pure conductive polymers, these can be overcome by blending them with other materials to produce hybrid composites with distinct, synergistic properties, making them suitable for applications in electrical, optical, and electronic fields. Conductive polymers containing conjugated carbon chains with alternating double and single bonds are responsible for conductivity due to delocalized π electrons and polarization. Among the most common of these polymers are polyfuran (PF), poly(phenylene vinylene) (PPV), poly(para-phenylene) (PPP), polypyrrole (PPY), polyaniline (PANI), polythiophene (PTH), and polyacetylene (PA) [4].

Since the early 1980s [5], conductive polymers such as PPY have been used as active layers in gas sensors. This is due to their many properties, including high visible light absorption, good conductivity, low weight, energy storage potential, and unique electrochemical properties. These polymers are also easy to prepare and affordable. The chemical structure of pyrrole is C_4H_5N , a five-membered ring

containing one nitrogen atom and four carbon atoms, highlighting its essential chemical properties [6]. This polymer has been used to improve the non-conductive properties of polyvinyl pyrrolidone (PVP), also known as polyvidone or povidone. Its hydrophilic properties and biocompatibility characterize it. PVP is available in various molecular weights and viscosities, allowing it to be selected according to the desired application characteristics. It is used in many biological applications, including industrial and medical applications, and as a binder in battery applications [7]. PVP can form hydrogen bonds, which raises melting points and exhibits better compound stability under physiological conditions and characteristics. Medium molecular weight polyvinylpyrrolidone (K30) is often used as a binder in tablets, capsules, and granules, as a stabilizer for oral solutions, as a film-forming agent, as a solvent, a dispersant for dyes, as an enzyme immobilizer, and to enhance bioavailability [8].

Nanoparticles are effective materials for reducing the band gap, allowing for narrower bandwidths. Modern electronics uses crystalline graphene oxide to produce microelectronic devices and semiconductors. One of the many graphene derivatives, graphene oxide (GO), has many oxygen-containing functional groups attached to its carbon lattice, such as hydroxyl (-OH), epoxy (-O-), and carboxyl (-COOH) [9]. Graphene oxide, or GO, is a carbonaceous material with a flat, two-dimensional shape and a hexagonal crystal structure, similar to chicken wire or honeycomb [10]. Graphene oxide is much more amenable to chemical modifications due to the presence of these oxygen groups, making it more hydrophilic than graphene and easier to disperse in solvents [11].

Another interesting nanomaterial is the Indium Tin Oxide (ITO) which is highly degenerate n-type semiconductor, thin ITO films, deposited under different oxygen pressures and temperatures, exhibit low electrical resistivity ranging from 2×10^{-4}

to $4 \times 10^{-4} \Omega \text{ cm}$, depending on the deposition conditions and film thickness, the low resistance of films is due to the high carrier concentration, as the Fermi level (EF) lies above the conduction level (EC). The degeneracy results from oxygen vacancies and substitutional tin impurities generated during film deposition. The carrier concentration of highly conductive ITO films ranges from 10^{20} - 10^{21} cm^{-3} . Therefore, ITO nanoparticles are used in a variety of applications, thanks to their unique combination of transparency and conductivity. These applications include transparent electrodes in flat panel displays and solar cells, surface heaters for automotive windows, camera lenses and mirrors, and transparent heat-reflecting materials in building windows, lamps, and solar collectors [12].

A gas sensor is an advanced chemical device used to detect and analyze gases in the surrounding environment. It has numerous applications, such as air quality monitoring, industrial safety, household appliances, and even medical diagnostics such as breathing monitoring [13]. A gas sensor converts the presence or concentration of a gas into a measurable and processable electrical signal. This type of sensor typically consists of a receiver that interacts with the target gas molecules and a transducer that converts this interaction into an analytical signal. The mechanism of action lies in the adsorption of the gas onto the surface of the active material, resulting in a change in physical or electrical properties, such as conductivity or voltage [14]. These changes are then translated into digital data. They are often manufactured using nanomaterials due to their large surface area, enhancing their sensitivity and ability to detect very low concentrations of hazardous gases such as ammonia (NH_3) and nitrogen dioxide (NO_2), which are harmful gases. NH_3 is a common chemical component naturally released by humans, animals, and plants, making it one of the most widely used compounds. Nitrogen oxides, which are mainly produced from the combustion of fossil fuels and vehicle emissions, are

a major source of nitrogen dioxide (NO₂), making it essential to develop sensitive and efficient gas sensors [15]. Biosensors are an important branch of this field and are classified according to the type of bioreceptor (such as enzymes, antibodies, or nucleic acids) or the type of transducer (such as electrochemical, optical, thermal, or mechanical). The effectiveness of these sensors depends on basic properties such as sensitivity, selectivity, speed, and stability under different operating conditions. Biosensors and gas sensors are compatible with several key criteria that must be considered to improve their performance, such as high sensitivity, selectivity, response time, recovery time, long-term stability, ease of manufacturing, and low cost [16] .

Nanoparticle-based biosensors have revolutionized the accurate detection of chemical compounds. Nanoparticles such as carbon nanotubes and noble metal nanoparticles have become both receptors and receptors thanks to their unique properties, such as enzyme-like catalytic activity [17]. One of the most prominent applications of these sensors is measuring blood urea levels, an important indicator of liver and kidney health. Normal blood urea levels range between 3.3 and 6.7 mM, and abnormal levels can lead to serious diseases [18]. Urea is also widely used in agriculture, necessitating the development of accurate monitoring techniques due to its environmental and health impact. Furthermore, bacterial resistance to antibiotics has become a serious global challenge, especially with strains such as *E. coli* and *Staphylococcus aureus* becoming resistant to conventional treatments. This highlights the importance of nanotechnology, which enables the design of smart drug delivery systems, early diagnosis of infections, and even the production of bacterial-resistant medical materials. This represents a fundamental step in combating this threat and protecting the future of modern medicine [19].

1.2 Literature Survey

1- In 2016, Ashraf Salmanipour *et al.* [20] demonstrated the development of urea sensors using polymers. The conductive polymer polypyrrole (PPY) was employed to immobilize the urease enzyme within the matrix during electrochemical polymerization, enabling the fabrication of amperometric, potentiometric, and optical sensors with a detection range of 2–400 μM , high sensitivity, response time of less than one minute, and applicability to real samples such as blood and urine. Their efficiency was further improved by incorporating supporting materials such as Laponite and functional polymers. In contrast, the non-conductive polymer polyvinylpyrrolidone (PVP) was used as a matrix in the form of nanofibers prepared via electrospinning, providing a high surface area and microporous structure that enhanced absorption and response efficiency. These sensors exhibited a linear range of 0.5–2.5 mM and a fast response time of 10–30 seconds, making them suitable for rapid and accurate analysis in both biological and environmental applications.

2- In 2018, Harish Modilla *et al.* [21] fabricated an advanced polypyrrole-graphene oxide (PPY-GO) nanocomposite electrode for efficient detection of urea without using enzymes. The researchers relied on cyclic voltammetry (CV) and square-wave voltammetry (SWV) techniques to determine urea concentration in an alkaline 0.1 M potassium hydroxide solution over a 0–0.6 V voltage range. The modified electrode demonstrated high efficiency in catalyzing the urea oxidation process, resulting in an electrical response consistent with the urea concentration, particularly in the 0.5–3.0 $\mu\text{mol/L}$ range. The lower detection limit (LOD) was very low, reaching 0.27 $\mu\text{mol/L}$, demonstrating the device's high sensitivity and accuracy. The electrode surface was analyzed using scanning electron microscopy (SEM) and four-transform infrared (FTIR) spectroscopy, and the results revealed

that the nanomaterial exhibits distinctive properties, such as high conductivity, rapid electron transfer, and self-catalytic ability.

3- In 2018, Farhan Lafta Rashid *et al.*[22] developed novel nanofluids by blending PVP and PEG (1:1) with varying concentrations of MgO nanoparticles (0–12 wt%) in water. Increasing MgO content enhanced optical absorbance, thermal conductivity, and antimicrobial activity, with the strongest inhibition zones observed at 12% MgO. These findings demonstrate the nanofluids' thermal and biological efficiency, making them promising for applications in medical, industrial, and energy systems.

4- In 2019, Amany. M. El Nahrawy *et al.*[23] showed that polystyrene-supported ITO nanocomposites doped with CuO exhibited excellent thermal stability, dielectric behavior, and strong antibacterial activity. Structural analyses confirmed well-crystalline, uniformly distributed nanoparticles, while electrical tests revealed a decrease in dielectric constant with higher CuO content. The composites demonstrated the strongest antimicrobial effect at 7 wt% CuO, making them promising for transparent electronics and bioprocessor applications.

5- In 2021, Xiaohong Zheng *et al.* [24] developed a cost-effective NO₂ sensor using nanoporous ITO film prepared by electrochemical corrosion of commercial ITO glass. The sensor showed excellent performance at low temperatures across a wide range (0.1–500 ppm) with a strong response (12.34 at 1 ppm). Structural analyses confirmed a unique nanoporous network that enhanced gas diffusion and surface utilization, while increased hydroxyl groups improved NO₂ adsorption. These results highlight electrochemically corroded ITO as a promising, low-cost sensor for environmental and industrial applications.

6- In 2022, A. M. Alsaad *et al.* [25] synthesized graphene oxide sheets using Hummer's established method, then employed the casting technique to fabricate thin films by amalgamating PEO with GO. The samples were analyzed, and FTIR indicated a slight shift in the peaks and a variation in intensity at the C-O-C bond. XRD showed a peak at 14.68, corresponding to the 001 plane. The phenomena of absorption and permeability were examined. Differential scanning calorimeter (DSC) analyses indicated a reduction in the degree of crystallinity of the fabricated films, ultimately resulting in an increase in electrical conductivity with the addition of 8% graphene.

7- In 2022, Tao Li *et al.* [26] upsed nanostructured metal oxides and two-dimensional (2D) materials in the production of gas sensors, highlighting their advantages of rapid response, cost-effectiveness, and superior sensitivity. However, they exhibit drawbacks, including high operating temperatures, high power consumption, and poor selectivity. Consequently, metal oxides have been combined with 2D materials to create heterostructures, which enhance sensitivity and selectivity. This study used indium tin oxide (ITO) to improve 2D graphene. ITO is a ternary compound composed of 90% indium oxide (In_2O_3) and 10% tin oxide (SnO_2). It exhibits excellent transparency and conductivity, and has a cubic bixbite structure similar to that of ITO. ITO is an n-type dopant that provides free electrons and is widely used in various electrical and optoelectronic applications. They can be designed for specific purposes such as gas sensing or biological sensing.

8- In 2022, Zexin Liu *et al.* [27] fabricated a $\text{Cu}_2\text{O}/\text{ZnO}$ composite layer on ITO glass via electrodeposition and atomic layer deposition. The coating achieved 71.5% light transmittance, meeting touchscreen requirements, and generated more reactive oxygen species (ROS) under solar irradiation due to a p–n junction that enhanced charge separation. Photocatalytic tests showed 92.5% antibacterial

efficiency against *Staphylococcus aureus* after just 3 minutes of sunlight exposure, highlighting its potential as a transparent antibacterial material for preventing hand-to-hand infections.

9- In 2023, Simin Khataee *et al.*[28] developed a highly sensitive non-enzymatic urea sensor using a La-CoFe LDH/rGO nanocomposite prepared by hydrothermal synthesis and integrated into a carbon paste electrode. The sensor exhibited an ultrafast response (5 s), high sensitivity ($1.07 \mu\text{A}/\mu\text{mol}\cdot\text{cm}^2$), and a very low detection limit ($0.33 \mu\text{mol}$) in alkaline medium. It showed excellent accuracy in serum and milk samples (94.8–102% recovery, $\text{RSD} < 3\%$), long-term stability (>3 months), and strong resistance to interference. These results demonstrate its potential for medical and food applications requiring precise, rapid, and enzyme-free urea detection.

10- In 2024, Míriam Bautista Cases *et al.* [26] designed a multilayer polymeric coating composed of ϵ -poly-L-lysine and hyaluronic acid (ϵ -PLL/HA) and applied it to indium tin oxide (ITO) surfaces, aiming to impart antibacterial properties. The biological efficacy of the coating against the Gram-positive bacterium *Staphylococcus aureus* was tested, with results showing that increasing the number of layers significantly improved the antibacterial activity, with a killing rate of 93.75% when using 24 layers. The researchers used multiple characterization techniques to confirm the success of the coating and its properties, including contact angle measurement to assess wettability, X-ray photoelectron spectroscopy (XPS) to examine the surface chemical composition, and confocal fluorescence microscopy (CFM) and scanning electron microscopy (SEM) to study the distribution and interaction of bacteria on the surface. These results confirm the effectiveness of the proposed coating in reducing bacterial adhesion and its potential for use in medical applications to combat infections associated with implanted devices.

11- In 2024, Rawaa A. Abdul-Nabi and Ehssan Al-Bermamy. [29] formed a NO₂ gas sensor and its possible uses in industrial fields by mixing 2D graphene oxide at a rate of 0.8% with Si₃N₄ at varied ratios (0.2%, 2.2%, and 4.2%). The findings demonstrated that raising the Si₃N₄ ratio lowered the dielectric constant and energy loss while improving the electrical characteristics of AC. The sensitivity was applied at several temperatures, room temperature (RT), 100 °C, and 200 °C, exhibiting the behavior of p-type semiconductors. The sensors were subjected to NO₂ gas; the electrical resistance was reduced. The optimal sensitivity at room temperature was 6.89%, accompanied by a reaction time of 16 seconds and a recovery time of 19 seconds while using 3% hybrid nanomaterials.

12- In 2025, Arunima Verma *et al.* [30] developed a novel gas sensor based on a polypyrrole (PPY) hybrid nanocomposite supported by silver and copper nanoparticles (Ag/Cu) for the detection of ammonia (NH₃) at room temperature. The composite was prepared using oxidative chemical polymerization, with the silver and copper concentrations adjusted to optimize performance. Structural and microscopic analyses (XRD, FTIR, UV-vis, FE-SEM, EDS, and TGA) revealed that the homogeneous distribution of metals within the polymer enhanced electrical conductivity and increased adsorption sites. The PPY@Ag/Cu5 sensor achieved the highest response of 73% at 300 ppm NH₃, with a fast response and recovery rate (11 s). The sensor also demonstrated high selectivity towards NH₃ compared to other gases such as CO, CO₂, H₂S, and ethanol, and stable performance under various humidity conditions. The sensitizing performance is attributed to the charge interactions between NH₃ and PPY, and the synergistic effect between the nano-metals.

13- In 2025, Rawaa A. Abdul-Nabi and Ehssan Al-Bermany.[31] developed a hybrid nanocomposite with improved structural, optical, and biological properties. XRD analysis revealed a stable semicrystalline structure, FTIR revealed strong bonds, while FESEM and TEM images revealed a homogeneous nanodistribution. The composite exhibited high absorption in the UV range (200–280 nm) with a gradual decrease in the energy gap from 3.55 to 3.1 eV. Biologically, it demonstrated antibacterial activity against *E. coli* and inhibited the growth of lung cancer cells (A549) with signs of apoptosis, making it promising for applications in sensors, biocoatings, and antibacterial and anticancer therapies.

14- In 2025, Seda Gungordu Er *et al.*[32] developed multifunctional conductive nanofibers for a self-powered bioelectrical glucose sensor. Polycaprolactone (PCL) was combined with polypyrrole (PPy) and graphene derivatives (GO, PG, GF) using fabrication methods such as direct mixing, core-sheath nanoencapsulation, and dip-coating. Among the composites, PCL/PPy/GO fibers exhibited the best performance, offering high electrical conductivity, mechanical strength, and efficient glucose sensing due to improved electron transport. These fibers also functioned as a triboelectric nanogenerator (TENG), generating up to 63 V, and enabled accurate detection of glucose levels in sweat. The work introduces an innovative, flexible, and sustainable platform that integrates biosensing with energy harvesting for wearable diabetes monitoring.

15- In (2025), Ayisha Jemshiya Kalladi and M. T. Ramesan.[33] researchers fabricated three-component nanocomposites (NCs) composed of polyvinyl alcohol (PVA), cashew gum (CG), and polypyrrole (PPy), reinforced with zinc oxide (ZnO) nanoparticles via in situ green polymerization. Characterization confirmed strong component interactions and uniform ZnO dispersion. Incorporating ZnO decreased the optical bandgap, enhanced thermal stability, and significantly improved

mechanical and electrical performance, with 3 wt% ZnO identified as the optimal loading. These findings demonstrate the potential of the NCs for eco-friendly, high-performance nanoelectronic applications.

1.3 Aims of the work

1. Study the effect of graphene oxide and indium tin oxide (ITO) nanoparticles on the structural, morphological, optical, and electrical properties of newly synthesized PVP-PPY NCs.
2. Evaluate the performance of the NCs as gas sensors for NH_3 and NO_2 .
3. Investigate the antibacterial activity of the composites against *E. coli* and *S. aureus*.
4. Develop a non-enzymatic electrochemical sensor for urea detection.

Chapter Two

Theoretical part

2.1 Introduction

This chapter addresses the overarching notions of several theoretical areas of research, including physical principles, scientific elucidations, interrelations, laws, raw materials, and optical and electrical characteristics.

2.2 Polymers

Polymers were first discovered in the 1920s; there are numerous synthetic polymers, including well-known ones like polyesters, as well as lesser-known ones utilized in medical applications for organs and degradable sutures [34]. The term "polymer" refers to units of high molecular mass molecules that are made up of numerous isolated structural elements and is derived from the Greek terms poly (many) and mars (parts). In other terms, polymers are enormous, highly molecularly weighted molecules or macromolecules. A variety of little molecules or monomers connect that. The process of monomers reacting to create polymers is known as polymerization. Two or more substances combine with or without the addition of another substance, such as heat, water, or another solvent, to create a high-molecular-weight molecule [35].

Enhancing the properties of conventional polymers by incorporating small amounts of nanofillers is an effective and cost-effective strategy for modifying polymer structures. These additives contribute to improving the thermal, tensile, and barrier properties of polymers, and reducing their flammability [36]. With current developments, polymer NCs are gaining increasing importance in energy applications due to their high flexibility, ease of fabrication, and compatibility with many industrial designs. Nanoparticles incorporated within the polymer matrix directly influence the physical, mechanical, and electrical properties of the host material, making these hybrid materials promising in multiple fields [37]. These

hybrid systems exhibit distinct functional behaviors, including optical, electrical, thermal, and mechanical properties, as well as antibacterial capabilities, qualifying them for use in biomedical applications, flexible electronics, and sensors [38].

2.2.1 Classification of polymers

Polymers cannot be classified into a single category due to their complex structures, diverse behaviors, and wide applications. Therefore, polymers are classified according to their source into natural polymers composed of proteins, carbohydrates, cellulose, and rubber, derived from plants and animals, and synthetic polymers produced by chemical processes. The vast majority of basic polymers are synthetic polymers, such as plastics and synthetic leather. Synthetic polymers also exhibit enhanced thermal stability, mechanical and physical properties. Their molecular weight and structure determine the physical properties of polymer materials [39].

They are classified into linear polymers, which are linearly organized polymers and only bifunctional monomers can form linear polymers. Branched polymers which form side branches extending from the main polymer chain affect elasticity and density. Conjugated polymers whose chains are linked by covalent bonds through the addition of atoms or molecules are also known as network polymers. Network polymers consist of trifunctional layers forming three-dimensional networks. Polymers can be classified based on their homogeneity (repeating units) into homopolymers, which form a composed of a single type of monomer. Copolymers composed of different monomers, i.e., two repeating units, are classified as random polymers. Additionally, polymers are classified based on intermolecular forces into elastomers, which exhibit high elasticity due to weak intermolecular forces. Fibers with strong intermolecular forces provide high tensile

strength and toughness, as well as thermoplastics, which can be reshaped after melting due to weak intermolecular forces. Thermosetting polymers form rigid structures upon processing and cannot be recycled due to their strong cross-linking forces [40]. Figure (2-1) shows polymer chains in a variety of shapes and sizes [41].

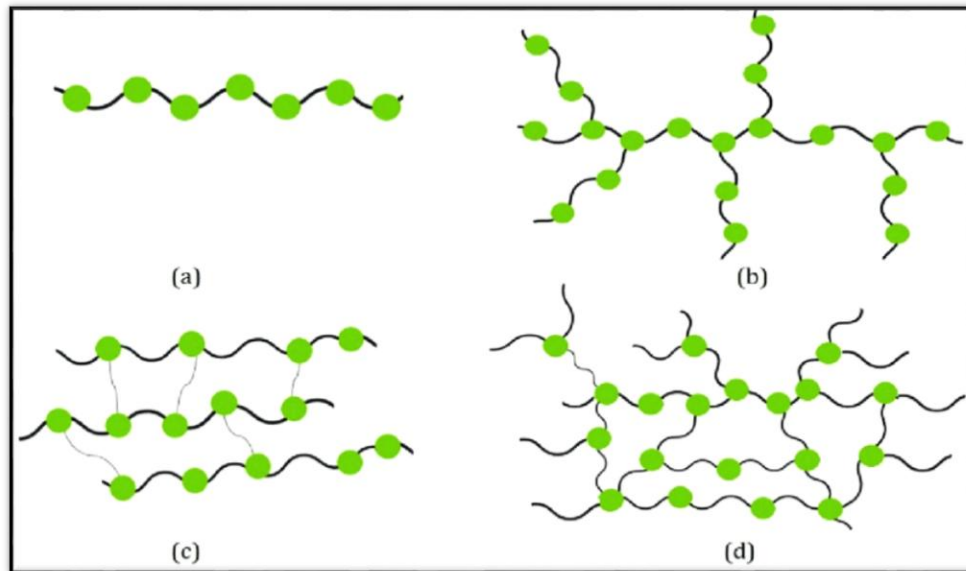


Figure (2-1). Polymer chains come in a variety of shapes and sizes[41].

2.2.2 Crystallinity of polymers

The crystallization of polymers is a phenomenon associated with the partial alignment of their molecular chains. These chains assemble to form ordered regions known as lamellae, which then form larger spherical structures. Polymers may crystallize during cooling after melting, mechanical stretching, or solvent evaporation. Crystallization affects the optical, mechanical, thermal, and chemical properties of the polymer [42].

In a molten polymer, the elongated chains of the material are twisted and intertwined in a network-like formation. The polymer chains exhibit significant

irregularity (stereoclastic disorder), resulting in a continuous, intertwined, chaotic structure for selected polymers. Even when a molten polymer transforms from a liquid to a solid, it is referred to as an amorphous polymer. Moreover, assuming that there are parts of the chain in which branching has occurred, this will lead to a lack of stereoregularity, which hinders crystallization. This material is called a semi-crystalline polymer because part of it is not exposed to crystallization [43], as shown in fig (2.2).

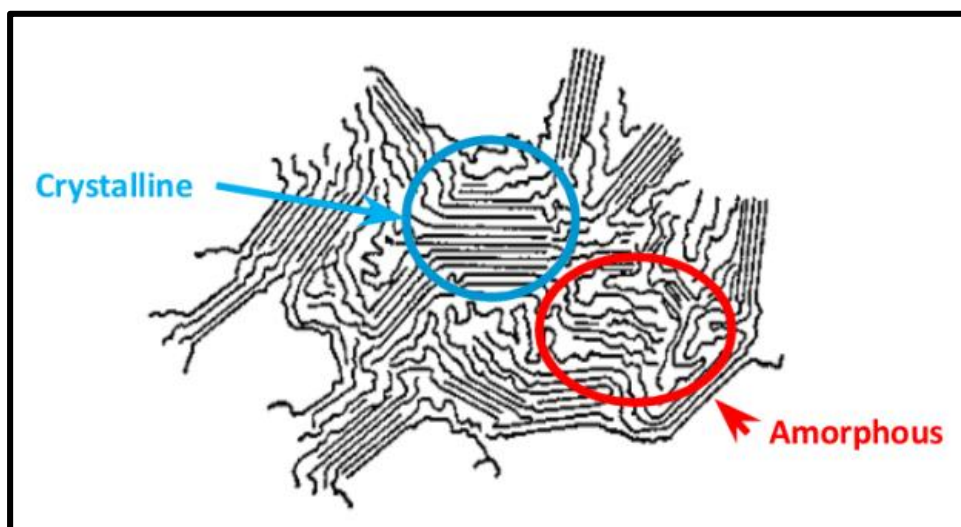


Figure (2-2). The crystallinity region in the polymers [44].

2.2.3 Conductive polymers

Conductive polymers are polymers that exhibit electrical conductivity due to the presence of alternating single (C-C) and double (C=C) bonds along the polymer's main chain [45], as illustrated in Figure (2-3).

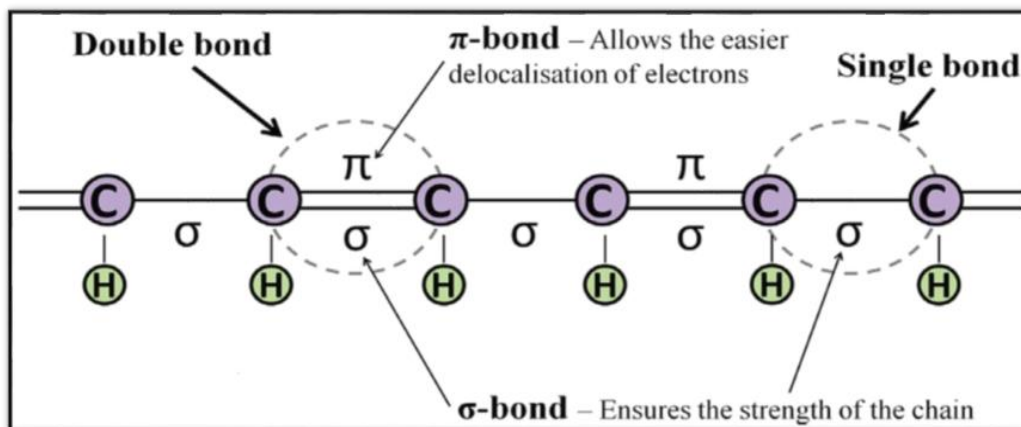
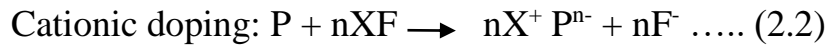
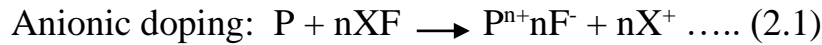


Figure (2-3). Alternation of double and single bonds in Poly pyrrole [45].

The electrical conductivity of materials is based on the band gap model (BGM), as shown in Figure (2-4), which illustrates the energy difference between the valence and conduction bands. The band gap (E_g) is defined as the difference between the top of the valence band and the bottom of the conduction band. Materials are classified into three types based on the energy gap: insulators ($E_g \geq 10$ eV), where the energy difference between the valence band and conduction band is very large, and a large gap prevents the transfer of electrons and therefore does not conduct electricity; semiconductors ($E_g \approx 1.0$ eV), where the band gap is intermediate so that electrons can cross the gap at room temperature; conductors, on the other hand, have almost no band gap, allowing electrons to move easily. These materials conduct electricity excellently, as the conduction band overlaps with the valence band, reaching nearly 0 eV ($E_g \approx 0$ eV). The energy gap in conducting polymers lies within the semiconductor range. This was demonstrated by Bridas and Streit in 1985, who found that the E_g value in these polymers was close to 1.0 eV. Conductivity in polypyrrole arises from the formation of mobile charge states, such as polarons and dipoles, during oxidation or reduction processes that electrons

undergo within the polymer [46]. When the polymer is oxidized, an electron is removed from the chain, creating a free radical and a positive charge that is stabilized via charge resonance. This state is known as a polaron. As the oxidation process increases, dipoles are formed, which are more stable than having two separate polarons. These polarons and dipoles move along the polymer chain or between chains, giving the material its electrical conductivity [47].

To compensate for the charges generated during oxidation or reduction, anionic or cationic species are added to the polypyrrole polymer matrix in a process known as doping. This doping improves conductivity by creating more mobile charges along the chain, similar to a railway track. The following equations represent the ionic doping process [48].



P represents the polymer in its neutral state, P^{n+} in the oxidized state, and P^{n-} in the reduced state. X^{+} represents the cations and X^{-} the anions. F^{-} is the conjugated anion, while n is the number of moles of added salt. The doping process generates new energy levels within the band gap, ultimately reducing E_g and merging it with the valence and conduction bands, making the material more like a metallic [48].

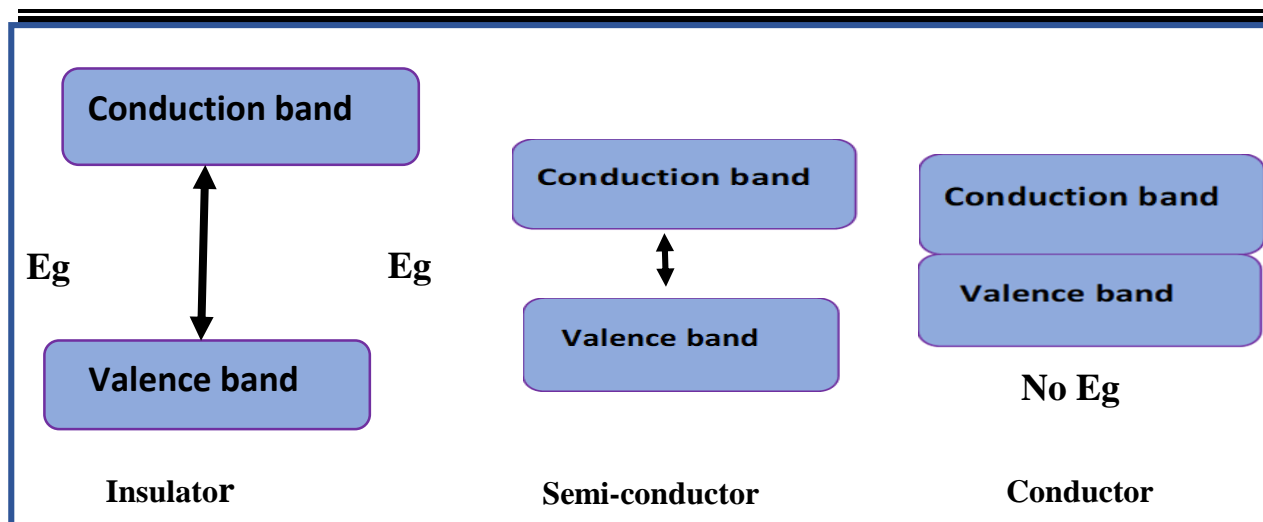


Figure (2-4). Diagram illustrating the band gap energy model for insulators, semiconductors, and conductors [48].

2.2.4 Preparation of polymers

The polymer manufacturing process is divided into two processes. The first is addition polymerization, where monomer molecules of the same type with double or triple bonds are repeatedly combined to produce polymers. This process produces no by-products. The second process is condensation polymerization, which results from combining different monomers after removing ammonia, alcohol, or water molecules [49] .

2.2.5 Polymer Blend

It is a traditional method through which two or more polymers In solid, liquid or molten state are blended to develop new materials with superior properties and at a lower cost than inventing new polymerization methods [50] . In addition to the need to improve the mechanical and functional properties of polymeric materials, the process of blending polymers is important and is used in medical applications, drug delivery systems, bone repair, wound dressings, and enzyme stabilization . The process of blending polymers depends on the free energy of blending ΔG_m [51] .

$$\Delta G_m = T \Delta S_m - \Delta H_m \dots\dots\dots (2.3)$$

Where ΔG_m is the free energy of mixing, T is the temperature of mixing, ΔS_m is the entropy of mixing, ΔH_m is the enthalpy.

For mixing to occur, $\Delta G_m < 0$ must be negative (less than zero). Controlling the morphological structure and phase behavior of polymer blends is essential for improving performance, as most polymers have high molecular weights and are immiscible when mixed, this separation weakens the material's mechanical properties [52].

2.3 Nanocomposites (NCs) and their Applications

Nanocomposites are mixtures of two or more phases with different compositions or structures, where at least one of these phases has dimensions less than 100 nanometers in zero, one, two, or three dimensions, or are thin films and layers. NCs have a high surface-to-volume ratio, and their dimensions and shape can influence their physical and chemical properties. These materials exhibit different behavior from conventional microstructured composites, which are among the most important materials in modern technology [53]. Composites are generally classified into three basic categories based on the size of the reinforcements in the structures: polymer-matrix NCs (PMNC), metal-matrix NCs (MMNC), and ceramic-matrix NCs (CMNC). The matrix and additives are the two main components of the chemical material. An integrated system can be created by encapsulating additional components within the matrix, enhancing its cohesion in scientific fields such as chemistry, physics, materials science, engineering, and manufacturing [54]. The following are some of the potential applications of nanotechnology.

1. Antibacterial dressings and coatings.
2. Precise gas and biological sensors for more effective treatment.

3. Barriers for thermal and optical applications.

2.4 The Raw Materials

2.4.1 Polyvinyl pyrrolidone (PVP)

Poly vinyl pyrrolidone (PVP), often known as polyvidone or povidone, is a polymer characterized by its ability to interact with many hydrophilic and hydrophobic substances [55]. The pyrrolidone structure gives this polymer functions similar to those of proteins. PVP k30 is a semi-crystalline synthetic polymer with a high glass transition temperature (T_g) because it contains the rigid pyrrolidone group, which is known to form various complexes with inorganic salts [56]. Figure (2.5) shows the chemical formula of polyvinylpyrrolidone, and Table (2.1) shows some of its physical and chemical properties.

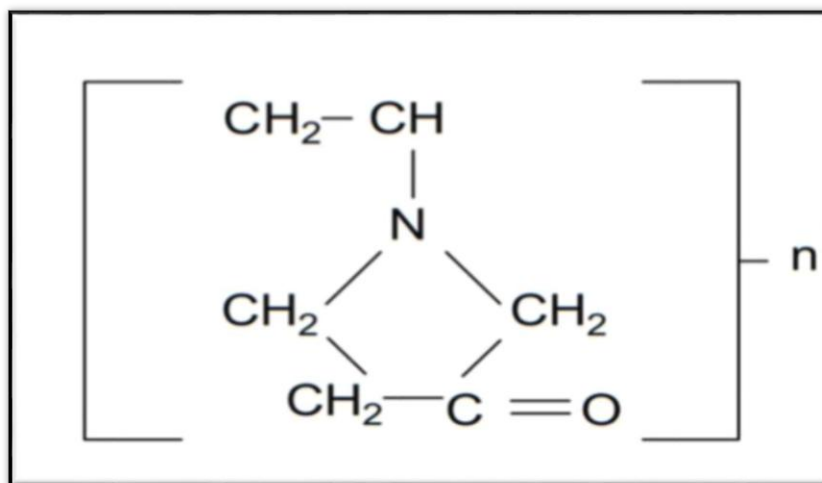


Figure (2-5).The chemical structure of polyvinyl pyrrolidone (PVP) [57].

Table (2-1). Physical and chemical properties of polyvinyl pyrrolidone(PVP) [58].

Property	Value and description
Molecular formula	(C ₆ H ₉ NO) _n
M.W	~ 40,000 g mol ⁻¹
Appearance	white color to light yellow powder
Solubility	Freely soluble in water, ethanol, methanol, and chloroform and very slightly soluble in acetone.
Density	1.25 g/cm ³
Refractive index	1.53
Melting temperature (T_m)	150-180 C°
Glass transition temperature (T_g)	109 C°
Toxicity	Non-toxic

2.4.2 Polypyrrole (PPY)

Polypyrrole, initially known as black pyrrole in the 1960s, is an amorphous, electrically conductive polymer widely used in various commercial applications due to its superior thermal stability, excellent electrical conductivity, relative ease of fabrication, and environmental flexibility [59]. Conductive polymers possess intrinsic conductivity owing to the existence of a conjugated electron system or alternating single and double bonds within their chemical structures. This distinctive chemical feature has garnered the interest of several academics and experts across diverse academic and industrial fields globally. Polypyrrole has been extensively used in several prospective applications, including electrical devices, sensors, batteries, microactuators, antistatic coatings, and biological applications [60].

It has been synthesized and produced using several methods, including electrochemical oxidation and chemical oxidation of pyrrole monomer in diverse organic solvents and aqueous environments. The many uses of chemically

synthesized PPY need enhancements in key features, including processability, thermal stability, and conductivity, for future advanced applications [61] . Figure (2-6) shows the chemical structure of poly pyrrole, and Table (2-2) shows the physical and chemical properties.

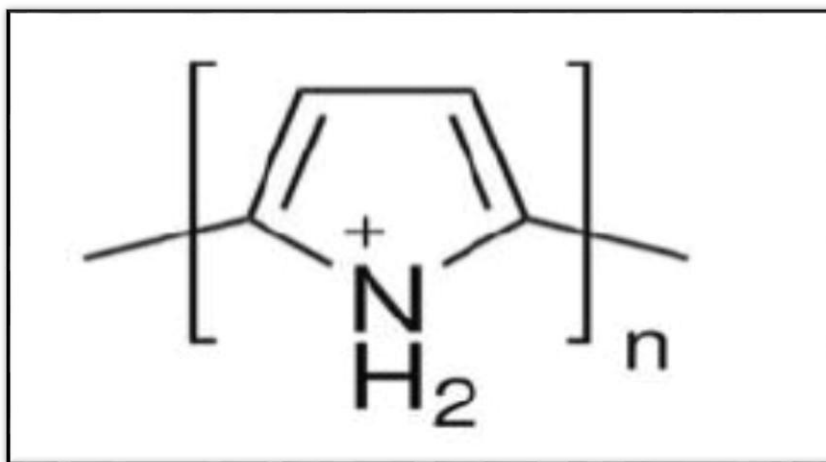


Figure (2-6).The chemical structure of Polypyrrole (PPY) [61,47].

Table (2-2).Shows physical and chemical properties of Poly pyrrole (PPY) [62].

Property	Value
Molecular formula	C ₄ H ₅ N
Appearance	Black powder
Density	1.60 g/cm ³
Conductivity	10-50 S/cm
Melting temperature (T_m)	129.7 C°
Glass transition temperature (T_g)	201- 300 C°
Toxicity	Non-toxic

2.4.3 Indium tin oxide (ITO)

Indium tin oxide (ITO) nanopowder is a modern, high-performance inorganic material with diameters ranging from 1 to 100 nm, designed for the 21st century [63]. It is a mixture of rare metal oxides (indium and tin), which are then blended to form a ceramic composite with outstanding electrical properties. ITO particles are Spherical on the outside (due to deposition or reaction conditions), and their atoms are arranged internally in a cubic bis-site structure, $\text{In}_2\text{O}_3:(\text{SnO}_2)$ in a ratio of 9:1, i.e., nine parts indium oxide to 1part tin oxide. The grains of these crystals have a surface electronic structure that produces surface, volume, and quantum effects, remarkable tunneling effects, high transparency, and high dispersion—features not found in macroscopic objects [64].

ITO nanopowder exhibits high light sensitivity, unique properties, and applications, including conductive coatings, gas sensors, biosensors, photodetectors, liquid crystal displays, and other uses. Nano powder has a highly reactive surface and contains many free radicals. This leads to the aggregation of large clusters of nanoparticles when additives are added, significantly affecting optical, electrical, magnetic, and other properties. Therefore, it is essential to distribute the powder well before use to achieve the best properties of the nanoparticles [65] Figure (2-7) and Table (2-3) shows the chemical composition of indium tin oxide (ITO) and some of its physical properties.

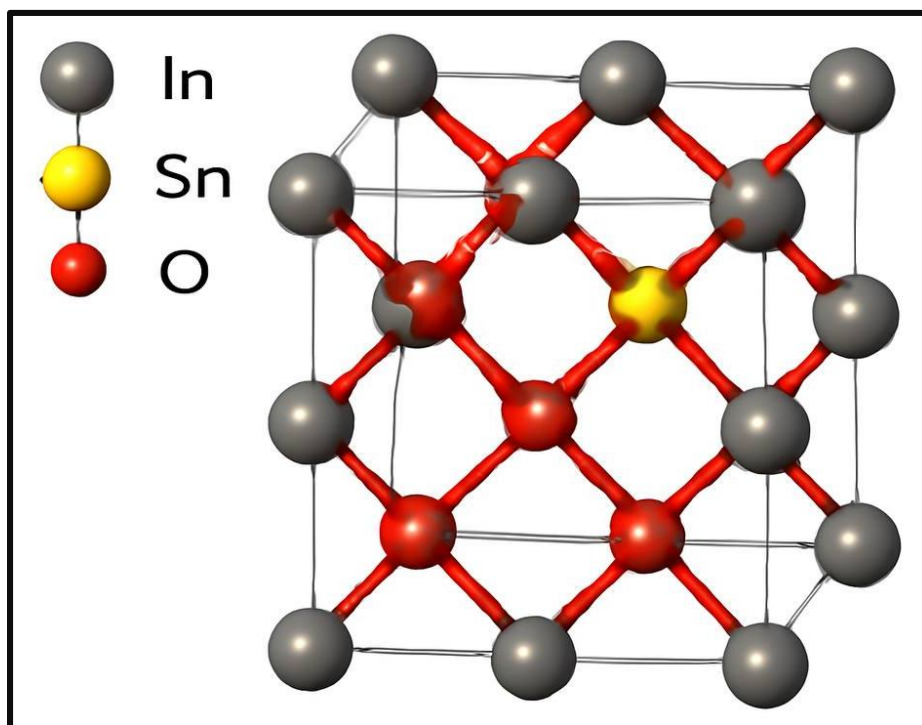


Figure (2-7). The ITO model with a 9:1 ratio: Atomic distribution of Indium, Tin, and Oxygen.

Table (2-3). Physical properties of ITO [67].

Property	Description
Chemical formula	$\text{In}_2\text{O}_3:(\text{SnO}_2)$
Crystal form	Spherical
Density	7.12 -7.16 g/cm ³
Appearance	yellow powder
purity	99.99 %
Melting point	1800 – 1926 C°
Specific surface area	40-15 g/cm ³

2.4.4 Graphene oxide (GO)

Graphene is a two-dimensional nanomaterial consisting of a single layer of carbon atoms arranged in a regular hexagonal lattice. It represents the basic structure of most other carbon materials. This unique structure gives it exceptional properties, such as high electrical and thermal conductivity and superior mechanical strength, making it a pivotal material in the fields of electronics, energy, and nanotechnology. The most prominent derivatives of graphene are graphene oxide (GO) and reduced graphene oxide (rGO), which are two-dimensional carbon materials derived from graphene through oxidation and chemical conversion processes [68].

Graphene oxide (GO) is characterized by the presence of a large number of oxygen functional groups, such as hydroxyl (-OH), carboxyl (-COOH), carbonyl (C=O), and epoxide (-C-O-C-), which are distributed on the basal surface and edges of the grain [69]. These groups give GO hydrophilic properties and high chemical activity, but they reduce electrical conductivity due to the disruption of the sp^2 domains in the carbon lattice. Therefore, chemical, thermal, or photoreduction processes are used to remove some of these groups and restore part of the original graphene structure, producing reduced graphene oxide (rGO) with superior electrical properties [70]. These materials are widely used in the fabrication of NCs, sensors, and energy applications due to their large surface area, structural flexibility, and functional modifiability. Graphene and its derivatives also have high light absorption, particularly in the near-infrared (NIR) range, making them suitable for photothermal conversion applications [7]. Figure (2-8) presents a schematic model of the molecular structure of G, GO, and rGO [71].

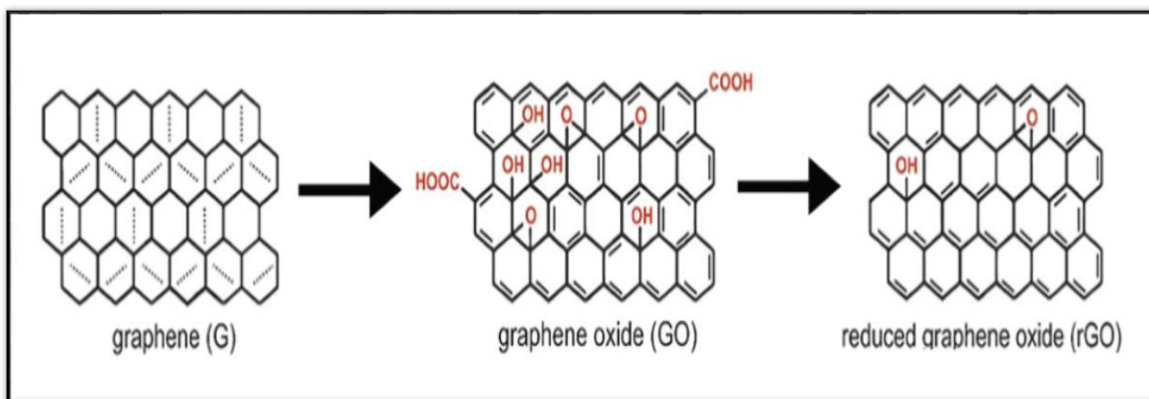


Figure (2-8). The chemical structure of graphene, GO, and rGO [71].

2.5 Solvents

Solvents are chemicals used to dissolve other substances without causing a chemical change. They are important in many industrial, medical, and laboratory applications. Solvents vary in their polarity, which affects their ability to dissolve different types of compounds. Types of solvents include polar solvents, nonpolar solvents, protic solvents, aprotic solvents, organic solvents, and inorganic solvents. Chloroform, whose chemical name is trichloromethane (CHCl_3), was used as the solvent in this work. It is a nonpolar organic solvent used in laboratories to extract organic compounds. It was also used in the past as a medical anesthetic, but it is no longer used for this purpose due to its toxic effects on the liver and nervous system. Chloroform is a colorless liquid with a distinctive odor. It is volatile and must be handled carefully, as prolonged exposure can cause health problems [72].

2.6 Characterizations

2.6.1 Fourier transforms infrared (FTIR) spectroscopy

Infrared (IR) spectrometry has undergone significant transformation in the last 40 years. In the 1960s, undergraduate chemistry students were taught that the principal use of infrared spectroscopy was for the structural elucidation of organic

molecules. Complex molecules possess more than one bond and various types of different vibrations, such as vibrations resulting from stretching, where the bond length changes at regular intervals by increasing or decreasing. Consequently, these stretches may be symmetrical or asymmetrical as in Figure (2-9) a [74]. The second type of vibrations is bending vibrations, which are known as deformation vibrations because the atoms remain in their positions within the group, but the shape of the molecule changes due to changing angles between the bonds. Bending vibrations are divided into two types: in-plane bending vibrations, where a change in the bond angle occurs within the same plane, including shear bending, where the bond angle decreases, and rocking bending, where the bond angle remains constant, but the bonds move within the same plane [75].

The other type is out-of-plane bending vibrations, which occur outside the plane of the molecule, and include oscillation, in which two atoms move to one side of the plane, and torsion in which one atom is below the plane and the other above the plane [76] as in Figure (2-9) b. Fourier transform infrared (FTIR) spectroscopy is an effective method for detecting the types of chemical bonds within a molecule by generating an infrared absorption spectrum that serves as a molecular "fingerprint." The concept of this approach is based on molecular bonding. Molecular bonds oscillate at different frequencies, depending on the atoms involved and the nature of the bonds. FTIR analysis provides a deeper understanding of the chemical bonds and molecular structure of materials without damaging them. This enables the identification of unknown substances, the detection of organic additives and some inorganic substances at low concentrations, and the characterization of changes in chemical structure and solvent residues [74].

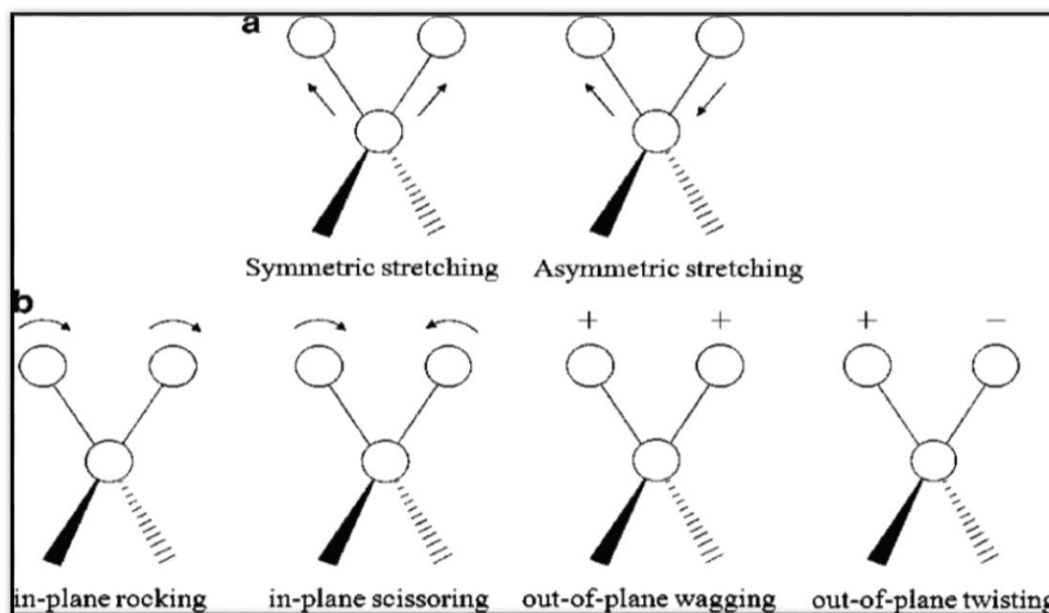


Figure (2-9). Types of molecular vibrations [77].

2.6.2 X-ray diffraction (XRD)

X-ray diffraction is a powerful and rapid analytical technique widely used to study crystal structure, determine phase, measure the degree of crystallinity, and estimate the crystal size of a material. This technique relies on the interaction of a single-wavelength X-ray beam with the crystalline atomic planes within a sample. The beams are reflected at specific angles resulting from the periodic arrangement of atoms, generating a distinctive diffraction pattern. X-ray diffraction peaks are formed when the beam strikes the crystal planes at a specific angle [78]. The reflected rays interfere constructively if Bragg's law is met (2.4). Figure (2-10) shows Bragg diffraction [80].

$$2d \sin \theta = n \lambda \quad \dots\dots\dots (2.4)$$

Where d is the interplanar spacing, θ theta is the diffraction angle, λ lambda is the wavelength of the incident X-ray beam, and n is the order of diffraction (usually taken as 1).

The cubic structure, which exemplifies the predominant pattern of the samples, may be computed using equation (2.5) [78].

$$a = d \sqrt{h^2 + k^2 + l^2} \quad \dots\dots(2.5)$$

(a) represent the lattice constants, and (h, k, l) represent the Miller indices. The lattice constant is given in the following equation [81].

$$\frac{1}{d_{hkl}^2} = \frac{h^2}{a^2} + \frac{k^2}{b^2} + \frac{l^2}{c^2} \quad \dots\dots\dots (2.6)$$

The crystal size (D) is measured in nanometers by the Scherrer equation (2.7) [82].

$$D = k\lambda/\beta \cos(\theta) \quad \dots\dots\dots (2.7)$$

where $k = 0.9$, λ for the wavelength of the X-ray radiation (Cu K- α_1) $\lambda = 1.54 \text{ \AA}$, while β represents the full width at half maximum (FWHM) of the diffraction peak (in radians), and θ for the Braggs diffraction peaks diffraction angle .

An X-ray diffraction apparatus consists of three basic components: an X-ray tube, a sample holder, and an X-ray detector. The cathode ray tube generates X-rays by heating the filament to generate electrons, which are then driven toward a target using an electrical voltage, bombarding the target material with electrons. X-ray spectra are generated when the electrons have sufficient energy to eject inner-shell electrons from the target material. Figure (2-10) shows Bragg diffraction [80].

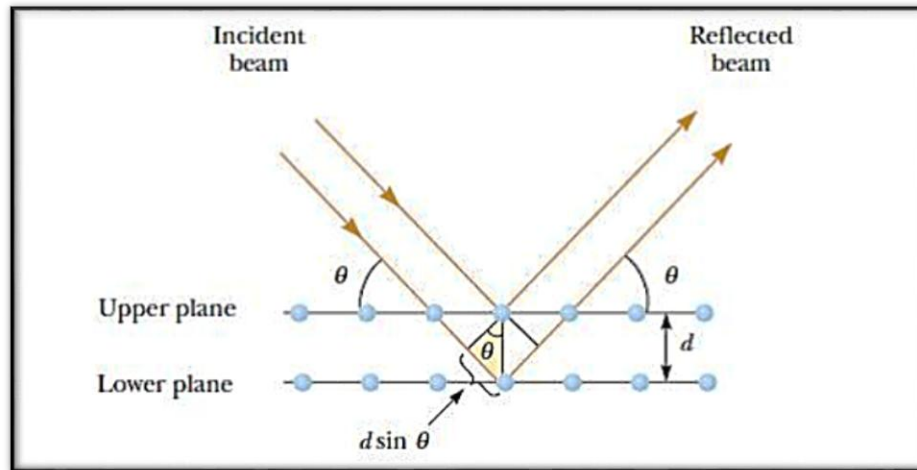


Figure (2-10). Bragg's Diffraction [80].

2.6.3 Field emission scanning electron microscope (FE-SEM)

A field emission scanning electron microscope (FE-SEM) is an electron microscope that utilizes an electron beam to generate pictures. In an electron microscope, light is substituted by electrons, which are negatively charged particles. A discharge A source of electrons is used. Electrons traverse the element in a zigzag manner [83]. Figure (2-11) the structural diagram of the field emission scanning electron microscope (FE-SEM) system is shown [84].

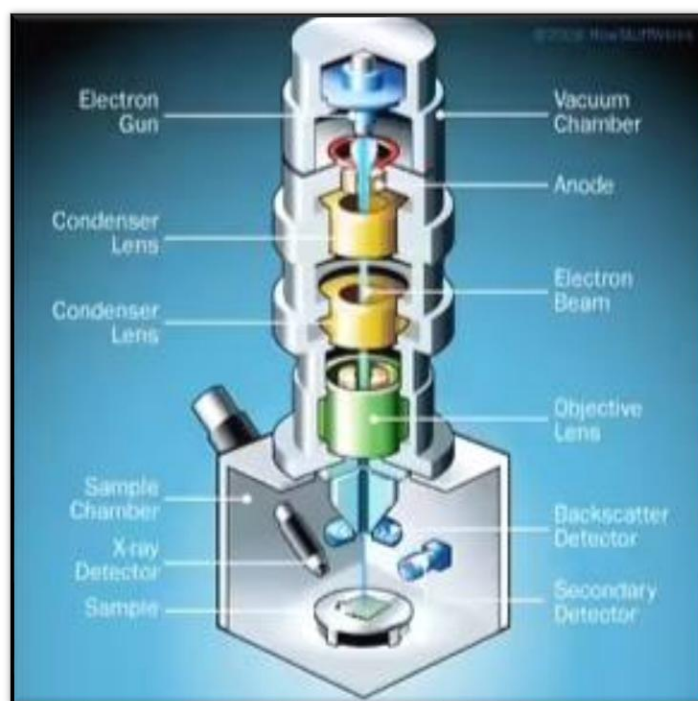


Figure (2-11). Ray Diagram for a system of FE- SEM [84].

2.7 Properties of samples

2.7.1 Optical properties

The optical properties of composite materials are studied to enhance understanding of the internal structure of polymers and the nature of their bonds, as well as to expand the scope of polymer applications. Understanding the absorption and transmittance spectra of a polymer composite facilitates the detection of diverse optical properties across a wide spectrum of wavelengths. Bond types, orbitals, and energy emission can be identified by analyzing them within the ultraviolet spectrum. The infrared spectrum is essential for understanding the overall structure of a polymer composite and its chemical components [85]. Diagram and image of UV-visible Spectrophotometer (UV-Vis.), as shown in Figure (2.12).

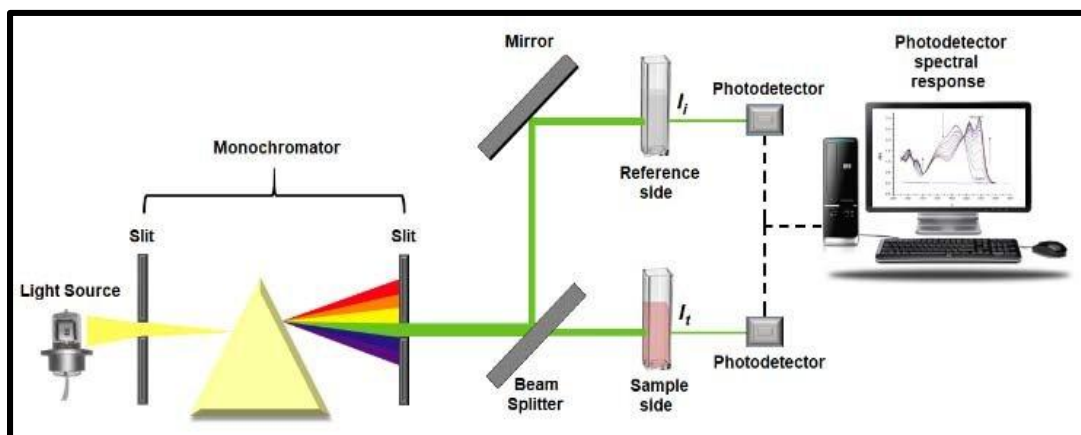


Figure (2-12). Diagram and image of double-beam UV-vis. spectrophotometer [86].

2.7.1.1 Absorbance (A) and transmittance (T)

It is a quantitative assessment of a material's absorption of light, represented by the ratio of the intensity of the absorbed light to the intensity of the incident light. A large optical depth at energies above the band gap will give the material good absorption while minimizing reflectance. Absorption is calculated using Equation (2.8),(2.9) [87].

$$A = \frac{I_A}{I_0} \dots\dots\dots(2.8)$$

$$A = \log \frac{1}{T} \dots\dots\dots(2.9)$$

Transmittance (T) is defined as the ratio of the intensity of transmitted rays (I_T) to the intensity of incident rays (I_0) on the material, as expressed by the following connection [88]:

$$T = \frac{I_T}{I_0} \dots\dots\dots (2.10)$$

Electrons of atoms vibrate on the surface of a material and radiate energy as a reflected wave when light falls on them. This reflected ray can be calculated from the law of conservation of energy (2.11) [89].

$$A+T+R=1 \dots\dots\dots(2.11).$$

2.7.1.2 Absorption coefficient (α)

The photon energy ($h\nu$) determines the absorption coefficient, the forbidden energy gap, and the properties of the material. The concentration of incident rays in the direction of wave propagation per unit distance leads to a decrease in energy, and the equation for photon energy is given by the following relationship (2.12) [90].

$$\alpha = \frac{2.303 \cdot A}{t} \dots\dots\dots (2.12)$$

(t) represents the thickness of the samples.

2.7.1.3 The fundamental absorption edge

It represents the sudden increase when the amount of absorbed radiant energy is approximately equal to the energy gap, and the energy difference between the highest point in the valence band and the lowest point in the conduction band is known as the fundamental absorption edge. Figure (2.13) shows three types of absorption regions.

- High absorption region: (α) in part (a) is equal to or greater than 10^4 cm^{-1} . The forbidden optical energy gap value (E_g^{opt}) is given by this region [129].
- Exponential region: (α) in B is $1 \text{ cm}^{-1} < \alpha < 10^4 \text{ cm}^{-1}$. This region is represented by the transition of the electron from higher energy levels in V.B. to lower energy levels in C.B., and vice versa, in addition to its reverse transition from lower energy levels in V.B. to higher energy levels in C.B. [90].

- Low absorption region: (α) in C is relatively small, approximately $\alpha < 1 \text{ cm}^{-1}$. This transition occurs as a result of structural defects that cause the density of states to move within the vacuum in this region [90].

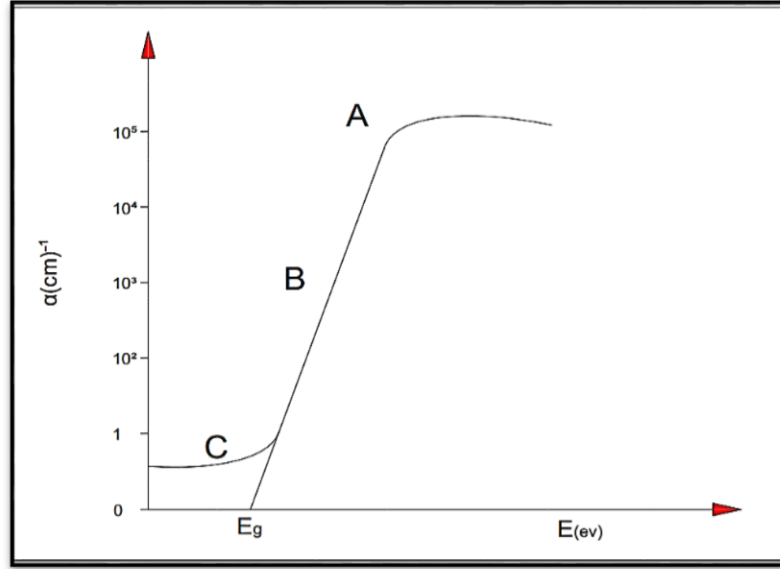


Figure (2-13). Absorption edge variation with absorption regions [91].

2.7.1.4 The electronic transitions

It is divided into two categories.

1. Direct transition: The absorption occurs in this condition when the energy of the incident photons ($h\nu$) is equal to or larger than the energy of the bandgap (E_g). This transition type necessitates preserving energy and momentum as dictated by the laws of physics. This transformation happens when the C.B. bottom is directly aligned with the top of the V.B., suggesting they share the same wave vector K , specifically $\Delta K = 0$, in the semiconductor's context. It can be classified into two distinct types [92].

A. Allowed Direct transition: It occurs from the valence band's highest points to the conduction band's lowest point, as shown in Figure (2.14.A) [93].

B. Direct forbidden transition: It happens near the top points of (V.B.) and the bottom points of (C.B.), as exposed in Figure (2.14. B) [93].

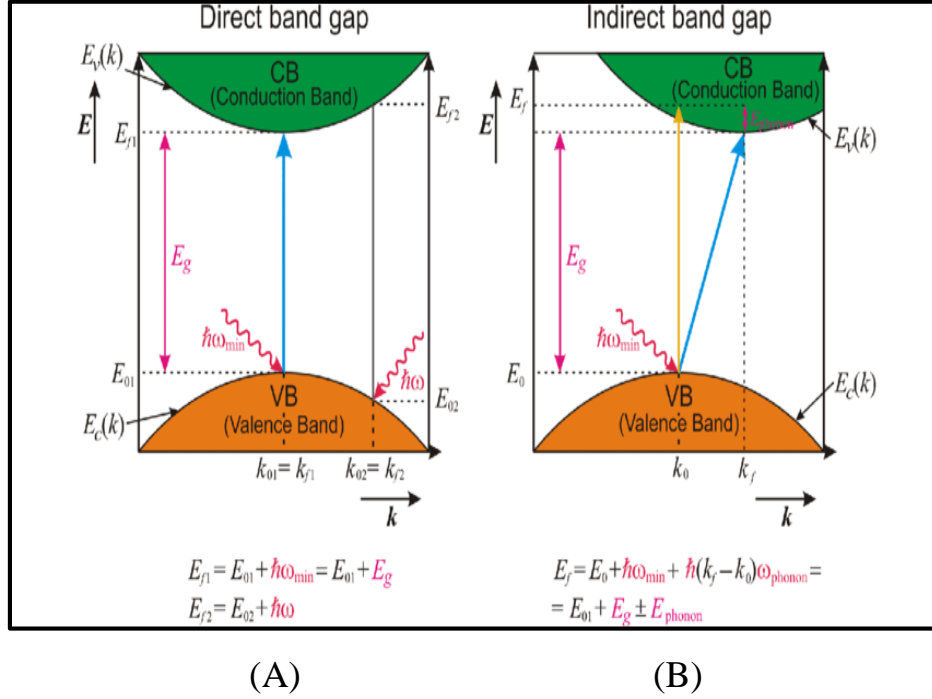


Figure (2-14). Classifications of electronic transitions [93].

2. The indirect transitions

The valence band (V.B) peak at different k vectors is the conduction band (C.B) minimum. The C.B band has no lower bound above the V.B peak in an indirect band gap. Therefore, in this case ($\Delta K \neq 0$), this type of transition must involve the emission or absorption of a phonon according to the laws of conservation of energy and momentum. It includes two types [94].

Allowed indirect transition: It occurs between the highest point in the valence band and the lowest point in the conduction band in a distinct area of K -space, as in Figure (2.14) A.

Forbidden indirect transition: It occurs between the nearest location at the top of the valence band and the nearest point at the bottom of the C.B. band.

These transitions are driven by phonon absorption, as shown in Figure (2.14) B. The absorption coefficient is calculated using Equation (2.13) [95].

$$\alpha_{hv} = B (h\nu - E_g^{opt} \pm E_{ph})^r \dots\dots\dots(2.13)$$

Where (E_{ph}) denotes the phonon energy, (B) is a constant depending on the material type, (-) denotes the phonon absorption, (+) denotes the phonon emission, (r) denotes the exponential transition m , and (r) = 1/2 and 1/3 represent the allowed indirect transitions, and (r) = 1/3 denotes the forbidden indirect transitions, respectively.

2.7.1.5 Refractive index (n)

The ratio of the speed of light in a vacuum to its speed within a material is known as the refractive index (n), according to equation (2.14) [96].

$$n = \frac{1+\sqrt{R}}{1-\sqrt{R}} \dots\dots\dots (2.14)$$

where (R) represents the reflectivity of the material.

2.7.1.6 Extinction coefficient (k_o)

The extinction coefficient is the imaginary component of the complex refractive index (N) [86] .

$$N = n - iK_o \dots\dots\dots(2.15)$$

(n) represents the real part of the refractive index. The extinction coefficient is calculated using Equation (2.16) [86].

$$K_o = \alpha\lambda/4\pi \dots\dots\dots(2.16)$$

(λ) represents the wavelength of the incident beam.

2.7.1.7 Dielectric constant (ϵ)

The dielectric constant represents the ability of a material to be polarized. It may be difficult to respond to many frequencies, and electronic polarity dominates over other polarizations. The real (ϵ_r) and imaginary (ϵ_i) dielectric constants are calculated using the following equations [97].

$$\epsilon_r = (n^2 - K_o^2) \dots\dots (2.17)$$

$$\epsilon_i = (2nK_o) \dots\dots\dots (2.18)$$

2.7.1.8 Optical conductivity (σ_{op})

Optical conductivity depends directly on the refractive index, absorption coefficient, and the speed of light in vacuum (c) as in Equation (2.19) [97].

$$\sigma_{op} = \alpha n c / 4\pi \dots\dots\dots (2.19)$$

2.7.2 Electrical properties

Materials are classified according to their electrical conductivity into insulators, semiconductors, and conductors. Electrical properties depend largely on the preparation process and deposition conditions. Furthermore, the electrical properties of a material depend on its chemical composition, the arrangement of atoms within the solid, and the energy gap defects. Electrical properties aim to describe the amount of electric charge, its behavior, and its sources. Defects can be reduced using several techniques, including annealing [98], including the material's microstructure, physical form, and chemical content [99].

2.7.2.1 Alternating current electrical conductivity (A.C)

AC conductivity differs from DC conductivity in that the electric field frequency during DC conductivity is constant, while during AC conductivity, the electric field frequency varies. The electric field frequency is determined by the polarization frequency, so complex dielectric constants can be used. The dielectric constant is defined as the ratio of the capacitance of a capacitor containing dielectric material between two conducting plates to the capacitance of a capacitor containing a vacuum between the plates, such that both capacitors are of equal volume. When an insulator is exposed to a low-frequency electric field, newly formed or permanent dipoles can easily form, easily adapting to the changing electric field without leaving any residue. Thus, the dielectric constant reaches equilibrium, where the ohmic conductivity is zero [99].

Alternating potential (voltage) $V = V_m e^{i\omega t}$ is given to a capacitor filled with an insulator. Where the current flowing by the capacitor leads to the potential by a phase of $\pi/2$ [100].

$$I = i\omega C_p V \dots\dots\dots(2.20)$$

(ω) is the angular frequency of the applied field ($\omega = 2\pi f$), (i) is an imaginary integer ($i = \sqrt{-1}$), (C_p) is the amplitude, (V) is the voltage and V_m is the maximum voltage [101].

$$I = I_p + iI_q \dots\dots\dots(2.21)$$

The electrical current is equal to the amount of current (I_p) in the similar stage with (V) and (I_q) with the difference in the phase ($\pi/2$), (I_p) represents the short capacity stream to charge the current capacity or the best-charging current for the condenser

and (I_q) where the connection stream in the conductors due to flow the electron under the applied electrical capabilities. The equation (2.22) determines an intense capacity consisting of two parallel panels [141].

$$C_P = \epsilon_o \frac{A_a}{d} \dots\dots\dots(2.22)$$

Where ϵ_o the void is the void, (A_a) the region, and (d) represents the distance between the expanded panels.

Electrical energy is dispelled as thermal energy in electrical applications. Understanding the energy factor is extremely necessary for high-frequency insulation, the excessive energy factor generates, and works on energy outage [102].

In low frequencies, the cap (C) has a perfect condensation that is closely related to parallel to resistance [102].

$$\epsilon = \frac{C_p}{C_o} \dots\dots\dots(2.23)$$

The insulating loss (ϵ'') is calculated with the frequency of samples according to the equation (2. 24) [103].

$$\epsilon'' = \epsilon' D \dots\dots\dots(2.24)$$

(D) is the dispersion factor.

$$\sigma_{a.c} = \omega \epsilon'' \epsilon' \dots\dots\dots(2.25)$$

Alternative conductivity ($\sigma_{a.c}$) is a measure of lost capacity.

2.8 Applications

2.8.1 Gas sensor

The problem of pollution resulting from harmful gases emitted from industrial facilities and their negative impact on human health makes it important to detect these toxic gases, such as ammonia, nitrogen dioxide, hydrogen sulfide, and nitrogen monoxide. Sensor cells monitor the leakage of these gases in laboratories and environments requiring high safety and quality standards. Detection in sensors involves a chemical reaction between the sensor and the gas, converting the chemical signal into an electrical signal. Chemicals improve the sensitivity of sensors and are low-cost [104].

The sensor relies on the adsorption of gases on the surface of semiconductor oxides. Metal oxides are widely used in the manufacture of gas sensors, as oxygen atoms adsorb on the surface of the crystals when heated, creating a negative charge that affects the flow of electrons across grain boundaries. In the presence of a reducing gas, the potential barrier decreases due to the reduced density of the negative oxygen charge, leading to increased conductivity [105]. In the presence of an oxidizing gas, the number of free electrons decreases, reducing conductivity. The sensitivity of the sensor is primarily dependent on temperature, which controls the rate of the chemical reaction between the adsorbed oxygen and the gas molecules. At low temperatures, the reaction rate determines the sensor's response, while at high temperatures, the rate of gas diffusion across the surface influences it. While at medium temperature, a balance occurs between the two processes, which achieves the maximum response of the sensor [106].

In addition, the type of semiconductor affects its response mechanism. In n-type semiconductors, the reducing gas increases the conductivity, while the

oxidizing gas reduces it. In p-type semiconductors, the number of holes increases in the case of oxidizing gases, which leads to an increase in conductivity thus, the reducing gas reduces their number, so the resistance increases [107,108]. Figure (2.15) shows an example of how gas affects the gas-sensing mechanism of n-type and p-type metal oxide semiconductors.

Table (2-4). The resistance of a semiconductor when exposed to oxidation or reduction gases [108].

kind	oxidation Gases	reduction Gases
n-type	resistance rise	resistance drop
p-type	resistance drop	resistance rise

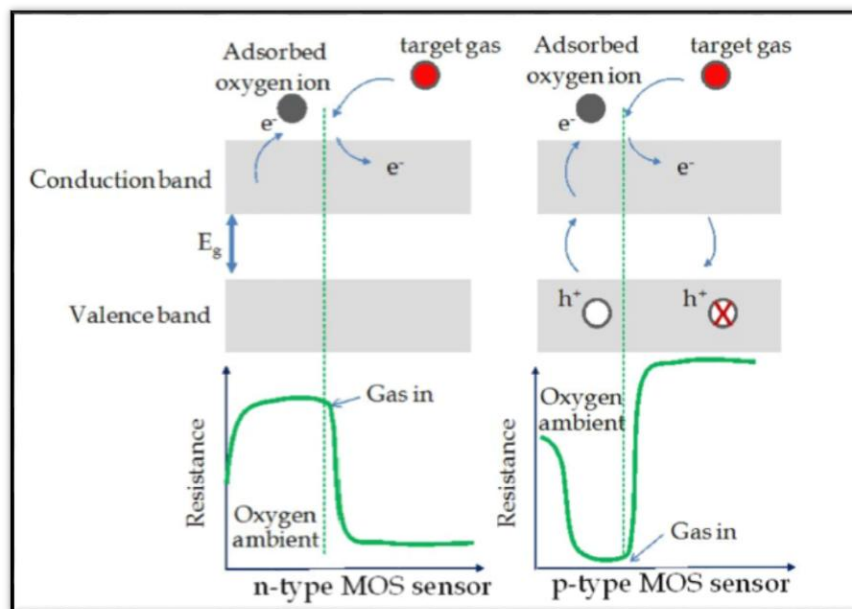


Figure (2-15). A diagram showing the gas sensing mechanism of an n-type and p-type metal oxide semiconductor in the presence of a reducing gas [109].

2.8.1.1 The adsorption mechanism

Adsorption is a physical or chemical process in which molecules or atoms from a gaseous or liquid phase are adsorbed onto a solid or liquid surface, forming a thin layer of adsorbent. Adsorption is a surface phenomenon where the reaction occurs at the surface without molecules penetrating the adsorbent[110] . This distinguishes it from absorption, which involves the penetration of molecules into the adsorbent. Physical adsorption occurs through weak van der Waals forces, is often reversible, occurs at low temperatures, and does not involve the formation of new chemical bonds between the molecules and the surface. Chemical adsorption occurs through strong chemical bonds (covalent or ionic) between the molecules and the surface. It occurs at higher temperatures, results in a change in the electronic structure of the adsorbed molecules, and is usually irreversible. Several factors influence the adsorption process, including temperature, pH, ionic strength of the solution, surface area of the adsorbent, nature of the adsorbent, equilibrium time, and adsorbent concentration. [111]. Adsorption is shown in Figure (2.16).

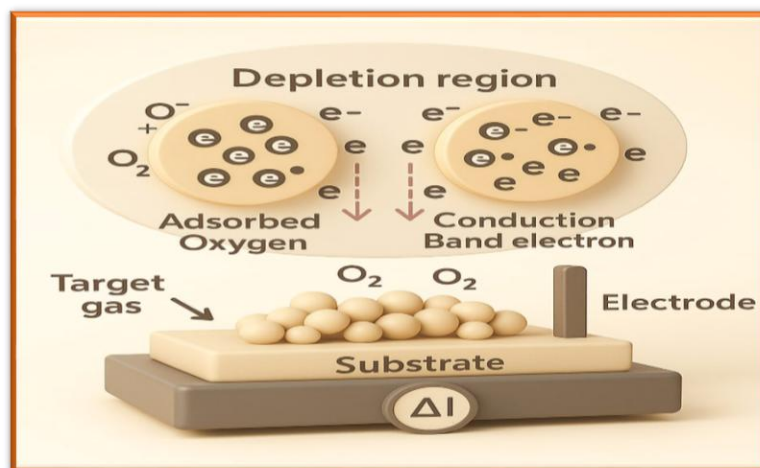


Figure (2-16). A diagram illustrating the metal oxide thin film gas sensor mechanism.

2.8.1.2 Ammonia gas NH₃

Ammonia is an essential chemical molecule in everyday life, especially after the development of nitrogen fixation technology developed by Fritz Haber and Carl Bosch, which facilitated the manufacture of artificial fertilizers that alleviated hunger for millions of people. Approximately 80% of global ammonia production is allocated to agriculture, while the remainder is used in military and commercial sectors, including explosives, refrigerants, pharmaceuticals, plastics, synthetic fibers, and cleaning agents [112]. Moreover, ammonia's high hydrogen density makes it an effective hydrogen carrier in fuel cells, including alkaline cells, phosphoric acid cells, and polymer electrolyte membrane cells [113]. Its carbon-free nature also makes it an efficient energy source for solid-state fuel cells. Due to growing global demand, annual ammonia production has exceeded 150 million metric tons and is expected to increase by 4% over the next four years [112].

Ammonia emissions are a serious environmental pollutant, negatively impacting health and the ecosystem. This colorless gas, with a pungent odor and high vapor pressure, causes eye, skin, and respiratory irritation even at low doses. The Occupational Safety and Health Administration (OSHA) has lowered the maximum permissible exposure level to ammonia from 50 parts per million (ppm) to 35 ppm for short-term exposure [114]. Ammonia reacts in the atmosphere with nitrogen and sulfur oxides to produce fine particulate matter (PM_{2.5}), which causes premature death. It also acidifies coastal waters and disrupts marine ecosystems. Ammonia concentrations in industrial and laboratory settings must be strictly regulated [115].

2.8.1.3 Nitrogen dioxide gas NO₂

NO₂ gas is formed when nitrogen (N₂) and oxygen (O₂) molecules decompose into their atoms at high temperatures, causing them to react to form this gas. It is a toxic gas that is harmful to human and plant health. It is widely distributed in the environment because it is primarily used in fertilizer production at high temperatures [116]. Nitrogen dioxide has a reddish-brown color and a pungent odor, making it a major air pollutant. It is largely produced through combustion processes such as coal-fired power plants, metallurgical plants, and automobiles. The natural decomposition of nitrates in the soil by microbes releases NO₂ into the atmosphere. Exposure to large amounts of the gas causes breathing problems for people with chronic respiratory diseases. Furthermore, it reacts with other air pollutants to form ground-level ozone, which is harmful to human and plant health [117].

2.8.1.4 Sensitivity

It is the rate of change in the resistivity of a thin film in the presence and absence of a gas. Sensitivity is affected by several factors, such as the sensor temperature, the response time of the sensor, the exposure time of the membrane to the gas, and the film thickness. The following equation gives the gas sensitivity [118].

$$S = \frac{R_a - R_g}{R_0} \times 100\% \dots\dots (2-26)$$

Where R_a represents the resistance in dry air, R_g represents the resistance at the inlet of the analyte gas, R₀ represents R_a, and R_g represents the oxidizing and reducing gases.

2.8.1.5 Response and recovery times

Response time is the period during which the resistance of the sensor material exceeds a constant value from the previous value (often 90%) when the sensor is exposed to the highest possible gas concentration. In applications where low-quality response times are very good, such as when detecting flammable materials, [109] when the gas used is turned off, the recovery time begins, which represents the period during which the sensor resistance drops to 10% of the saturation rate. Figure(2.17) illustrates how this is calculated using sensor data by showing the resistance as a function of time and the sensor being in artificial air. For subsequent measurements, the sensor's recovery time must be short [162].

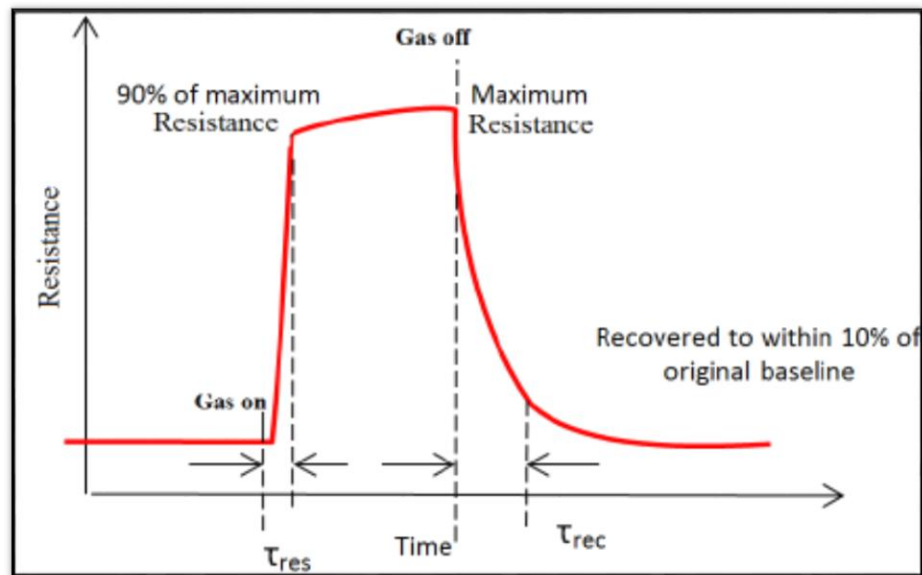


Figure (2-17). The chemoreceptive response curve [119].

2.8.2 Antibacterial effect systems

Antimicrobial drug resistance has increased in recent years due to the overuse of antibiotics. Researchers are working to construct and develop NCs with effective antibacterial methods, reducing the likelihood of antibiotic resistance spreading to nanomaterials. Researchers have shown interest in metal oxide-based materials to develop new hybrid systems with enhanced antibacterial properties. Thermally or chemically modified metal oxides can act as functional electrolytes, enabling the use of their physical and chemical properties or the synthesis of different molecules. Furthermore, research into hybrid antibacterial agents continues, including metals, metal oxides, and matrix components such as polymers [120].

The use of graphene nanosheets (such as graphite, graphene oxide (GO), and reduced graphene (rGO)) in the field of antibacterial activity is based on a sophisticated mechanism through the deposition of nanosheets on the surface of bacteria. The sharp edges of graphene oxide (GO) cause it to adhere to the bacterial cell wall, resulting in cell membrane rupture, allowing the cell contents of DNA, proteins, and cellular metabolism to leak out, causing cell death. The process of destroying the bacterial cell membrane involves reactive oxygen species (ROS) formed by graphene oxide, which oxidizes lipids and proteins within the bacterial cell, disrupting its essential functions through reactive oxidation, as shown in Figure (2.18). The absorption of nutrients and moisture occurs through the large surface area of graphene oxide, preventing bacteria from absorbing essential nutrients. Water and moisture surrounding the cell are absorbed, leading to cell dehydration and death [121]. This mechanism represents a physical interaction. In addition, bacteria are Gram-positive bacteria are less resistant to this damage than Gram-negative bacteria because of their different membrane structures [122].

ITO nanoparticles produce reactive oxygen species (ROS) (such as superoxide anions and hydroxyl radicals), especially when exposed to light. These species damage bacterial cell walls, proteins, and DNA, leading to bacterial death. Indium tin oxide (ITO) particles interact with bacterial membranes, disrupting the cell membrane and precipitating essential components of the cell. These molecules may release In^{3+} or Sn^{4+} ions, which are toxic to bacteria by interfering with enzymatic functions. ITO nanoparticles may carry a surface charge that interacts electrostatically with negatively charged bacterial membranes, causing destabilization. Furthermore, ITO has a wide band gap, and when doped or exposed to UV or light, it enhances its antibacterial photocatalytic effects [123].

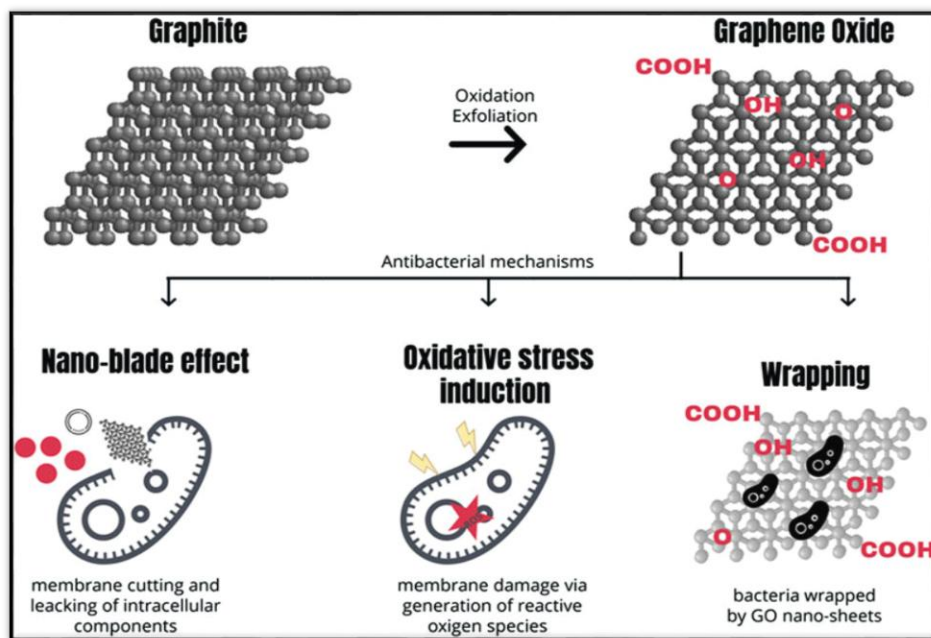


Figure (2-18). Schematic representation of the three different GO antibacterial mechanisms of action [124].

2.8.2.1 Escherichia coli (*E. coli*)

Escherichia coli is a naturally occurring microorganism found in the human gut and is a ubiquitous Gram-negative bacterium. It is a facultative anaerobe that can survive in either aerobic or anaerobic conditions. It is also the characteristic bacterium responsible for lactose fermentation, is rod-shaped, motile, and does not produce spores. *E. coli* Bacteria grow best in culture at 37°C and in a pH range of 6.0 to 7.0. For optimal bacterial growth, the optimal pH ranges from 4.4 to 9.0 [125]. However, some strains can become serious pathogens, causing food poisoning, urinary tract infections, and sometimes serious complications such as kidney failure, especially in children and the elderly. Their danger lies in their ability to develop antibiotic resistance, making treatment difficult and rapid [24].

2.8.2.2 Staphylococcus aureus (*S. Aureus*)

Staphylococcus aureus is a type of bacteria that lives harmlessly on the skin or in the nasal passages. These live bacteria can grow with or without oxygen, a trait known as facultative anaerobes. They can reduce nitrate and are known to be catalase-positive as part of the body's normal microflora [126]. These Gram-positive bacteria are characterized by their round shape, ranging from 0.5 to 1.0 µm in diameter, which is typical of non-motile, non-nuclear Gram-positive cocci. However, when they enter the body through a wound or surgery, they can cause severe infections such as dermatitis, sepsis, or even pneumonia. They can be seen alone or in pairs or clusters. The risk is even greater when it comes to methicillin-resistant strains (MRSA), which are among the most dangerous and difficult to treat [23].

2.8.3 Biosensors and their applications.

Biosensors are advanced technologies used to detect physical, chemical, and biological changes and convert them into measurable signals. The introduction of nanomaterials and nanostructures improves the performance of these sensors by enhancing sensitivity, reducing detection limits, and accelerating response times. This is achieved through the use of small sensor sizes, low cost, and ease of use.

An electrochemical biosensor consists of two components: a biological receptor (such as an antibody, enzyme, or other element) that targets the analyte and a transducer, which converts the biological signal generated by the reaction into a signal that is displayed on a special screen after amplification. These signals include light intensity, mass, voltage, current, capacitance, and resistance. They are used in various fields, such as medical diagnostics, food safety, and environmental applications [127].

The most important characteristics of biosensors are high sensitivity, selectivity, chemical stability, biocompatibility, and rapid performance. Therefore, highly efficient electrical, optical, and mechanical nanosensors have been developed. Electrochemical transducers play an important role in this type of sensor, as they can operate using amperometric or potentiometric pathways. With the development of direct electron transfer (DET) technologies, it has become possible to fabricate more precise and selective biosensors without the need for chemical mediators [128].

Nanomaterials such as graphene oxide (GO) and indium tin oxide (ITO) are among the most promising in this field due to their unique properties, such as high surface area, high adsorption capacity, rapid electron transfer, and biocompatibility. These properties make them ideal for developing precise and direct biosensors, which are difficult to achieve with conventional large-scale systems [129]. Figure (2.19) represents the schematic of the electrochemical biosensor's working mechanism.

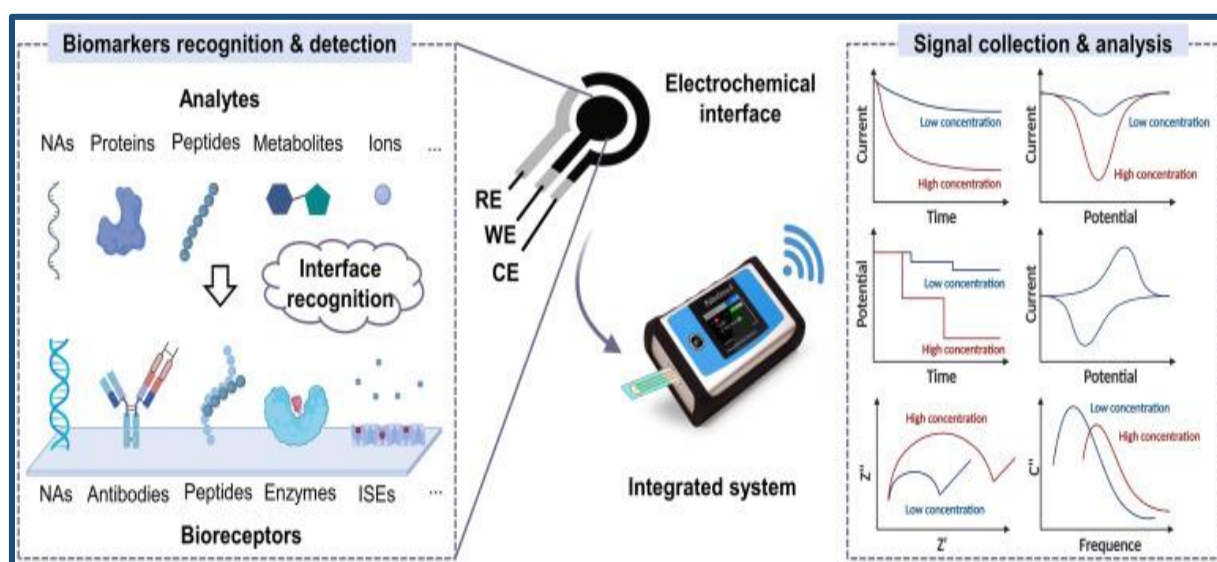


Figure (2-19). Schematic of the electrochemical biosensing system [130].

2.8.3.1 Urea

Urea, or carbamide, is a simple nitrogenous compound that plays an important role in the body's nitrogen balance. Produced from the breakdown of proteins, urea dissolves in the blood and is excreted by the kidneys as urine. A small amount of urea is also excreted from the body in sweat, along with water and salts. Figure (2.20) illustrates the structure of urea. It is a colourless, odourless, primarily neutral solid that is highly soluble in water [131]. It is also widely used in agriculture as a rich source of nitrogen in the fertilizer industry, making monitoring its environmental levels crucial. Conventional methods exist for estimating urea

concentration, but they are often complex and require prior sample preparation. Therefore, biosensors have emerged as a more effective alternative, especially in clinical applications. These sensors typically rely on the enzyme urease, which catalyzes the decomposition of urea into ammonia, which can be detected electrically or optically [132].

These biosensors have been integrated into various supporting materials, such as polymers and nanomaterials, to provide stability and measurement efficiency. However, the use of enzymes in the matrix makes the process more complex, time-consuming, and expensive. Furthermore, environmental chemical changes, thermal factors, toxicity, and humidity contribute to the decreased sensitivity and activity of enzymatic biosensors. In contrast, the use of non-enzymatic biosensors has been successful in detecting many biological substances, including urea [133].

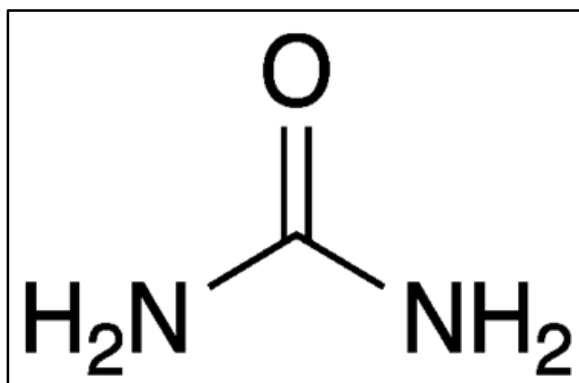


Figure (2-20). The chemical structure of Urea [134].

Chapter Three

Experimental

3.1 Introduction:

This chapter describes the materials used, the preparation process, the instrumentation, and the measuring techniques as shown in Figure (3-1).

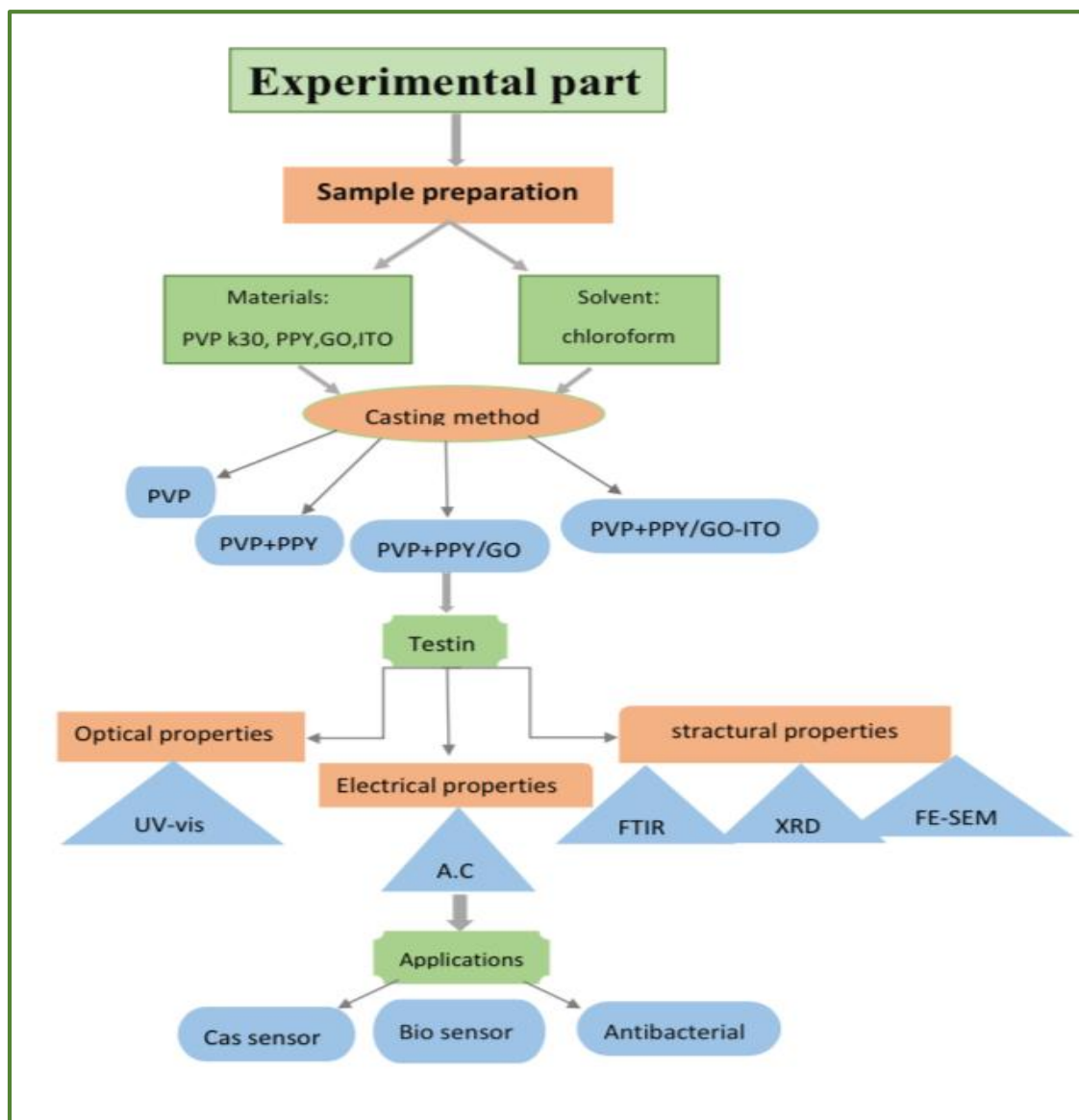


Figure (3-1). Scheme of experimental part.

3.2 The Utilized Materials

3.2.1 Polypyrrole (PPY)

Polypyrrole (PPY) with the chemical formula $(C_4H_5N)_n$, with a molecular weight of 68.098 g.mol⁻¹ supplied by Sigma Aldrich ,USA.

3.2.2 Polyvinyl Pyrrolidone (PVP)

Polyvinyl pyrrolidone (PVP) is a white, hygroscopic powder with a molecular weight of 40,000 g/mol and a molecular formula of $(C_6H_9NO)_n$, produced by Glentham Life Sciences, England, UK.

3.2.3 Indium tin oxide nanoparticles (ITO)

ITO nanopowders (yellow) are 50 nm in size and have a purity of 99.99%. They are made in the Hongwu International Group, China.

3.2.4 Graphene oxide (GO)

Synthesized GO used a modified Hummer process following our group's modified procedure, with full characterizations from a previous publication [9].

3.3 preparation of the nanocomposites (NCs)

Sample composition and mixing were fabricated using the solution casting method according to the following steps:

1. Both polymers were dissolved independently using chloroform. At room temperature, 9 g was dissolved in 150 mL of PVP K30 using a magnetic stirrer for 24 hours to ensure complete dissolution. 1 g of the PPY polymer was dissolved in 150 ml of chloroform using the same method.
2. Both nanomaterials were dispersed in chloroform independently using a magnetic stirrer and a gentle ultrasonication bath to improve dispersion before

loading and mixing. 50 mg of GO was dispersed for 72 h with a stirrer interspersed with ultrasonication for 10 min in an ultrasonic bath for every hour of stirrer time for the first three hours of collection, which was 30 minutes of ultrasonication in total. ITO was distributed in the same way as GO.

3. Fabricating the blended polymer by mixing PVP and PPY conductive polymers in proportions of 90% PVP and 10% PPY in proportions of (9:1).
4. To fabricate PVP-PPY/GO, GO nanosheets were added to the blended PVP-PPY and mixed for 36 hours. During the mixing, ultrasound assistance using an ultrasound bath was applied for 20 minutes each hour in the first 24 hours to achieve fine dissipation of nanomaterials in the homogenous matrix of blended polymers.
5. To fabricate PVP-PPY/GO-ITO, the GO and ITO nanomaterials were mixed with a loading ratio of 1:1 and sonicated for 24 hours to get hybrid (GO@ITO) nanomaterials before adding to the blended PVP-PPY; then the same procedure in step 4 was applied.
6. Finally, the samples were poured into silicone, cellophane and glass Petri dish molds with a thickness of 0.05 cm and some drops were poured onto glass slides with a thickness of 0.06 cm.

Figure (3-2) shows the detailed stages of sample preparation, while Table (3-1) shows the concentration ratio of the fabricated polymer, their blended polymers and NCs.

Table (3-1). shows the sample preparation ratio.

Sample	Code	Concentration, %			
		PVP	PPY	GO	ITO
PVP k30	S1	100	0	0	0
PVP-PPY	S2	90	10	0	0
PVP-PPY/GO	S3	90	9	1	0
PVP-PPY/GO@ITO	S4	90	8	1	1

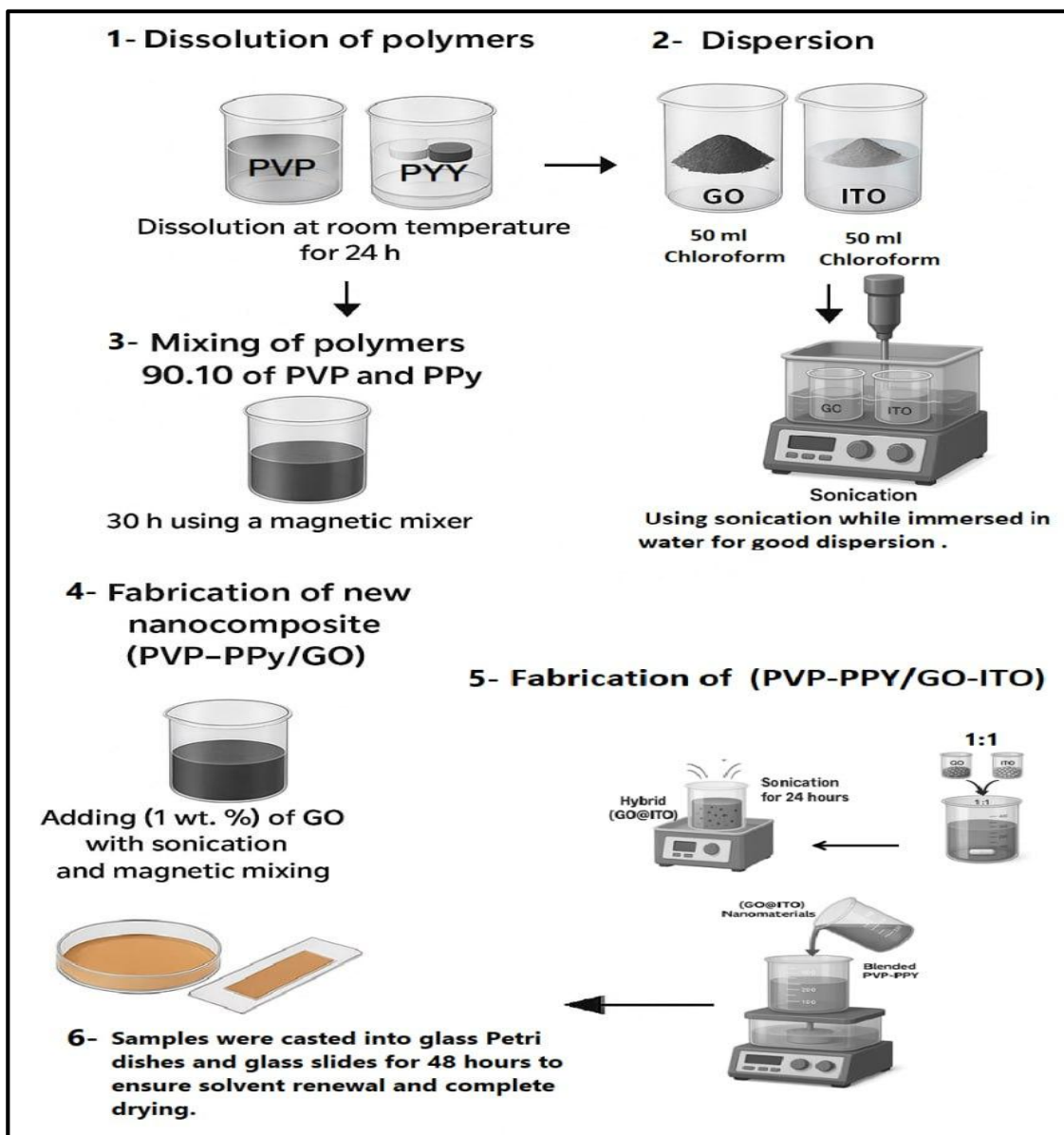


Figure (3-2). Samples preparation steps in this study.

3.4 Characterizations

3.4.1 Fourier-transform infrared spectroscopy (FTIR)

Spectrum IR-10.6.2 FTIR worked between $400 - 4000 \text{ cm}^{-1}$ and was made by PerkinElmer Company, USA. FTIR was located at Phi Nanoscience Center (PNSC) in Baghdad, Iraq.

3.4.2 UV-visible spectrophotometer (UV-Vis.)

The optical properties of pure PVP polymers, (PVP-PPY), (PVP-PPY/GO), and (PVP-PPY/GO-ITO) NCs were measured using a Shimadzu UV-18000A dual-beam spectrometer at wavelengths ranging from 300 to 1100 nm. The instrument is located in the University of Babylon/College of Education for Pure Sciences/Department of Physics.

3.4.3 X-ray diffraction (XRD)

An AERIS XRD device characterizes the crystallinity of materials with a 40 kV, 7.5 MW copper target tube, produced by Malvern Pan Analytical Company in the Netherlands. The device is situated in the Al-Khora Nano Research Laboratory in Baghdad, Iraq.

3.4.4 Field emission scanning electron microscope (FE-SEM)

An Inspect F50 FE-SEM, manufactured by FEI, Netherlands, was used to capture surface images of the materials. The device is situated in the Al-Khora Nano Research Laboratory in Baghdad, Iraq.

3.4.5 Measurements of A.C. electrical properties

The AC electrical current measurement method was used in the research. The capacitance (CP) and dissipation coefficient (D) were recorded for all sample films with a thickness of 0.05 cm at a frequency of 100 Hz to 5 MHz at room temperature. The device located in the Physics Department, University of Babylon, College of Education for Pure Sciences, LCR Hi TESTER, a HIOKI 3532-50, made in Japan, was used to evaluate the AC electrical conductivity.

3.5 Applications

3.5.1 Gas sensing applications

The gas sensors were prepared by depositing the film on a substrate using the drop-casting technique and depositing aluminum electrodes with a mesh structure with a thickness (about 300 nm) on the sample's surface using thermal evaporation under vacuum conditions. The thermal evaporation process was carried out using an (Edward 306-Thermal Evaporation Coating Unit) system. The basin type was (Spiral Tungsten (w)). If the sedimentation was carried out under a vacuum or high sedimentation pressure of 10^{-5} mbar, The attainment of a high vacuum level was accomplished by utilizing rotary and diffusion pumps. The monitoring was conducted using Berani and Penning gauges. The two electrodes were linked with slender wires, and a silver conductive paste was applied.

The gas sensing system shown in Figure (3-3) consists of a cylindrical stainless-steel chamber with a diameter of 20 cm and a height of 10 cm. The sensing system contains a gas inlet pipe and an air inlet pipe. The integrity of the pipes is checked before each test. Pins are placed on the base to help position the electrical wires for the heater, the sensing electrodes, and the thermometer at a temperature of K. The test chamber is then closed, and the sensing system contains a computer that

monitors the time and resistance of the sensor when exposed to the gas. Using the control panel, the temperature required to evacuate the test chamber is set by operating the rotary pump to about 1×10^{-1} bar. Then, the two-way valve (which connects the gas mixing chamber and the test chamber) is opened to allow the gas of known concentration to enter the test chamber. The change in the sensor resistance for the test gas-to-air ratio is measured using the flow meter. After the measurement, the test gas valve is closed, and the sensor returns to the original current value, R° . This process is repeated for the required temperatures (25, 150, and 250 C°). The equation below measures the response ratio of a gas sensor (S), where R_a is the sensor's resistance in dry air and R_g is the sensor's resistance in the optional gas. The equation(2.26)below measures the response ratio of a gas sensor (S) [135].

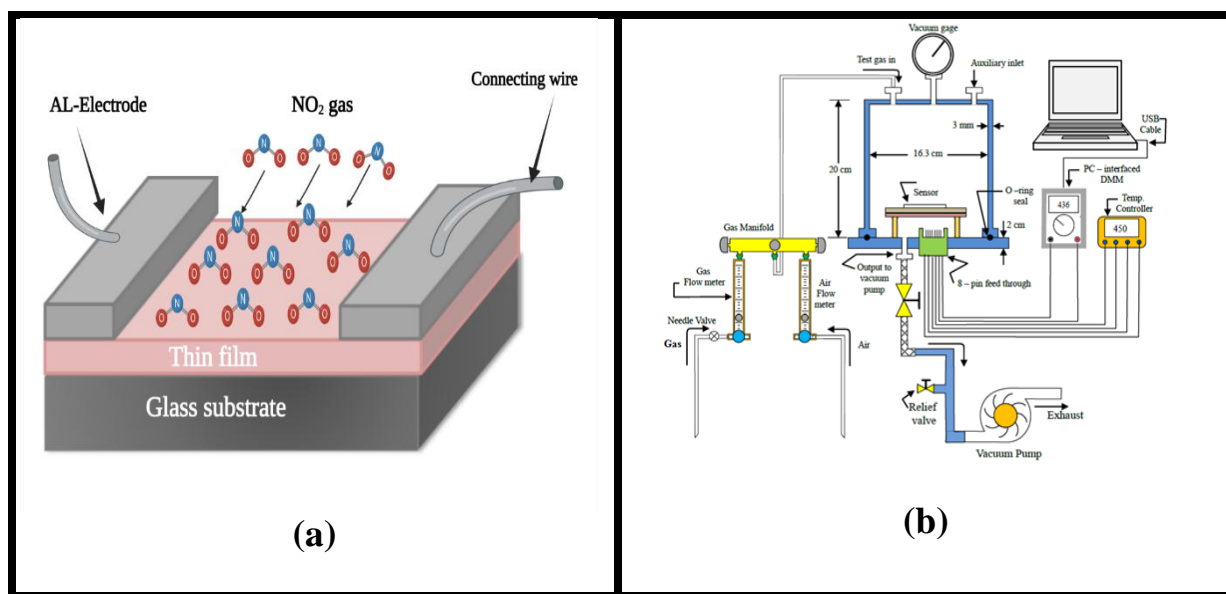


Figure (3-3). The diagram of the structures of gas sensors(a), and (b) gas sensor system [136].

The test was performed at the Phi Nanoscience Center (PNSC) laboratories in Baghdad, Iraq.

3.5.2 Antibacterial activity

Bacterial inhibition is the process of stopping bacterial growth using several methods. One such method is cellophane film diffusion, which tests the ability of a film of manufactured solid samples to exhibit antibacterial activity[137]. This is illustrated in detail in Figure (3-4)

Culture Medium Preparation

1. Mueller-Hinton (M-H) agar was prepared by adding 38 grams of powder to one liter of distilled water, then heating it on a stovetop with good stirring.
2. Mueller-Hinton (M-H) agar was sterilized in a steamer for 15 minutes at 121°C to sterilize it [138].
3. The medium was then allowed to cool to 50°C before being poured into a Petri dish. It was left to solidify for approximately 15 minutes, then inverted in the dish and stored in a refrigerator at 4°C.
4. The antibacterial activity of the prepared samples (S1, S2, S3, and S4) against strains of *Staphylococcus aureus* and *Escherichia coli* was studied in a separate dish using an agar well diffusion assay. Bacterial species were collected from their original cultures using a sterile wire loop. A sample of each bacterium was taken and seeded onto the agar surface in a uniform manner to form a bacterial layer.
5. Nanofilm Preparation: The nanomaterial (e.g., PVP-PPY/GO) was deposited onto the cellophane surface using the drop-casting method. The film was then allowed to dry completely (it can be dried in an oven at 60°C).
6. Cut the cellophane into 13 mm long pieces. Using sterile forceps, gently grasp the end of the cellophane film and place it over the bacterial culture area so that the deposited surface touches the bacterial culture medium.

7. Place the Petri dish in an incubator for 24 hours at 37°C.

8- The results are evaluated to record the inhibition zone by recording the average diameter of the inhibition zones using the (image j) program [139].

The test was performed at the Phi Nanoscience Center (PNSC) laboratories in Baghdad, Iraq.

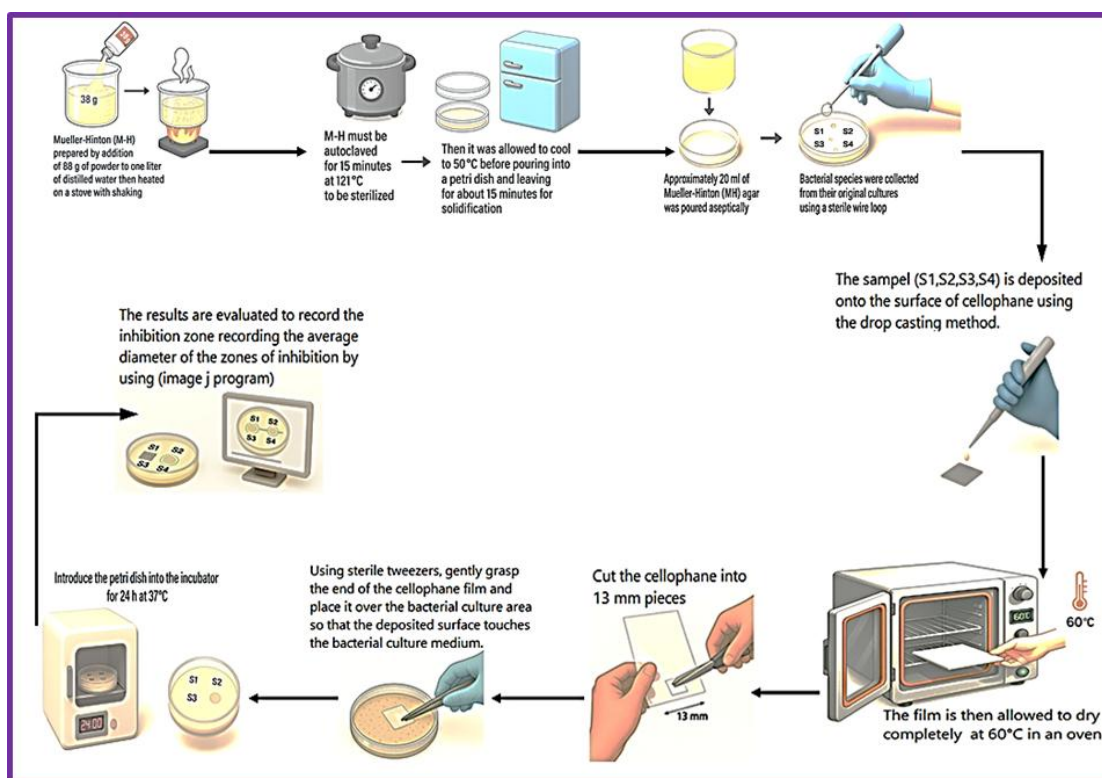


Figure (3-4). Evaluation of the inhibition activity of the Nanoantigen using the agar disk diffusion method.

3.5.3 Urea biosensor

The urea biosensor test was performed using an electrochemical cell based on a three-electrode system. The system consists of a carbon working electrode, an Ag/AgCl reference electrode, and a carbon auxiliary electrode. Initially, the electrolyte and sample solutions were prepared by dissolving three different amounts

of the studied substance (5 mg, 10 mg, and 15 mg) in 0.5 ml of 0.1 M hydrochloric acid, then subjecting them to ultrasonication for 15 minutes to ensure complete homogeneity. A 0.1 M urea standard solution was also prepared to serve as the analyte in the test. The printed electrodes were then connected to a potentiostat, and good electrical contact was ensured between the electrodes and the electronic system. The appropriate electrochemical technique was chosen according to the type of information required[140].

Cyclic voltammetry (CV) was used to analyze the redox properties, electrochemical impedance spectroscopy (EIS) was used to calculate the interface resistance between the electrode and the solution, and chronoamperometry (CA) was used to analyze the current over time. Test conditions, such as voltage range, scan speed, and signal frequency, were entered, and the test was initiated and data recorded. After measurements were performed on the sample without urea, the same tests were repeated after adding 10 microliters of a 0.1 M urea solution to the electrode surface. Following the experiment, the results were analyzed using plots such as the CV voltammogram or the Nyquist plot for EIS and compared with measurements from the blank (control) sample. In the case of EIS, the data were fitted using an equivalent circuit model, while in the case of CV, peak currents were calculated to assess the response efficiency. Finally, the electrodes were thoroughly cleaned with distilled water and ethanol and stored appropriately for future use [141]. Figure (3-5) illustrates the steps involved in conducting the test.

The test was performed at the Phi Nanoscience Center (PNSC) laboratories in Baghdad, Iraq. The Vertex-One device from Ivium Technologies was used.

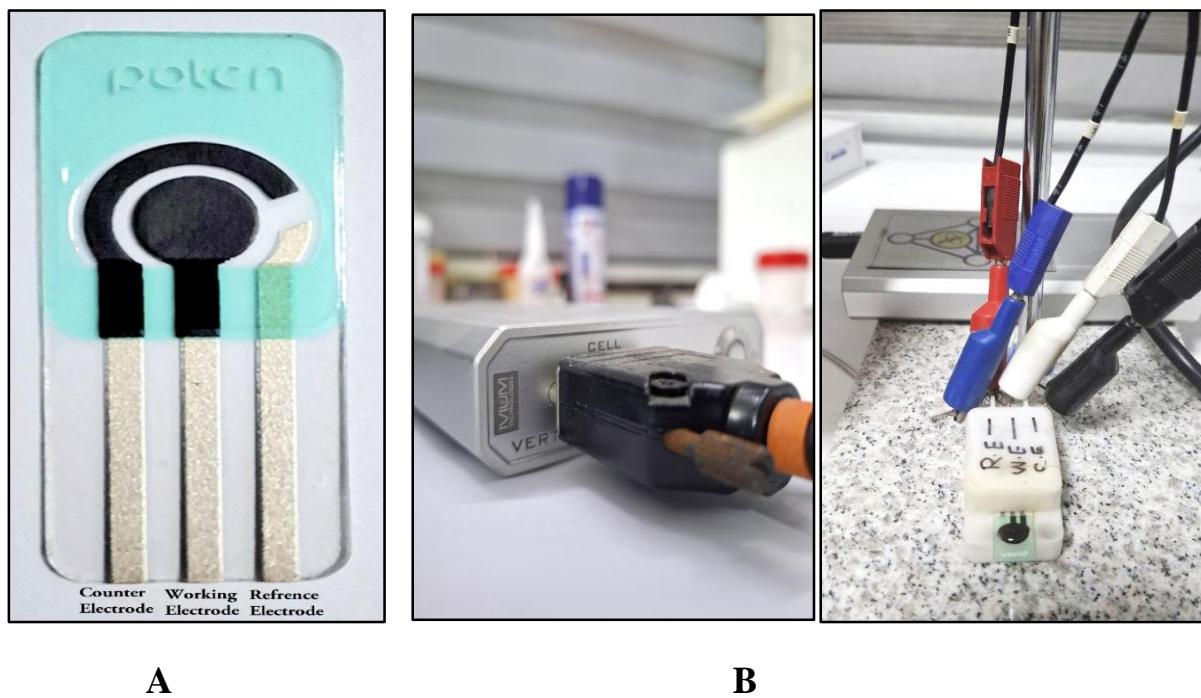


Figure (3-5). Diagram for connecting electrochemical screen-printed electrode(A), and steps of setting up and connecting electrochemical cell(B).

Chapter Four

Results, Discussion and Conclusions

4.1 Introduction

This chapter presents the results and discussions on the effect of indium tin oxide nanoparticles on some morphological, optical, and electrical properties, antibacterial, protective, and gas sensing properties of new blended polymers (PVP-PPY/GO-ITO).

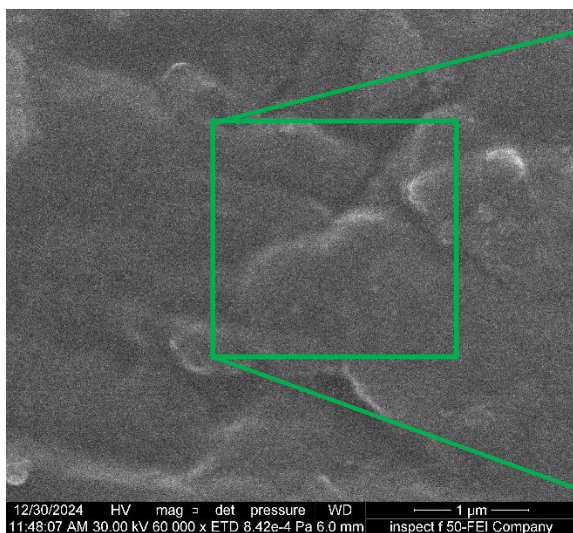
4.2 Structure properties

4.2.1 Morphological properties

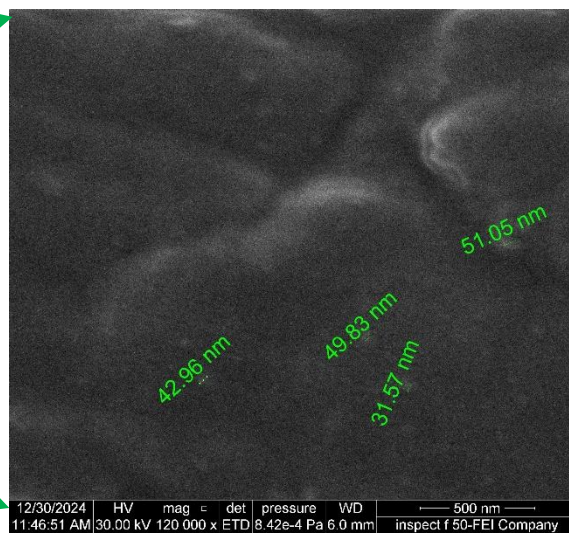
The surface morphology of the pure polymer and the new nanocomposite films was examined using FE-SEM, an effective tool for analyzing nanoscale surfaces, at different magnifications (microscopic and nanoscale) for each sample, as shown in Figure (4-1). The examination was performed under an accelerating voltage of 30.00 kV, using a secondary electron detector (ETD), low pressure, and a 6.4 mm diameter working lens. S1 shows a homogeneous surface of pure PVP-k30 polymer that is rough with some agglomeration and some small cracks. This is a natural feature due to its semi-crystalline nature that results in random rearrangement in the microstructure of the polymer chains [142]. Sample S2 shows a smooth surface of the polymer blend due to the homogeneous mixing of PVP-PPY polymers without aggregations or cracks [143].

Adding graphene oxide to the polymer mixture in the PVP-PPY/GO nanocomposite enhances the smooth surface shape with good homogeneity between the mixed polymers and some GO flakes or their edge presented on the surface of sample S3. Upon the addition of ITO nanomaterial, the GO-ITO effect appeared in sample S4, where it was observed that some particle sizes could be related to ITO due to some irregular particles scattered on the film surface attributed to the conductive phase of PPY polymer, which depends on the diffusion of pyrrole

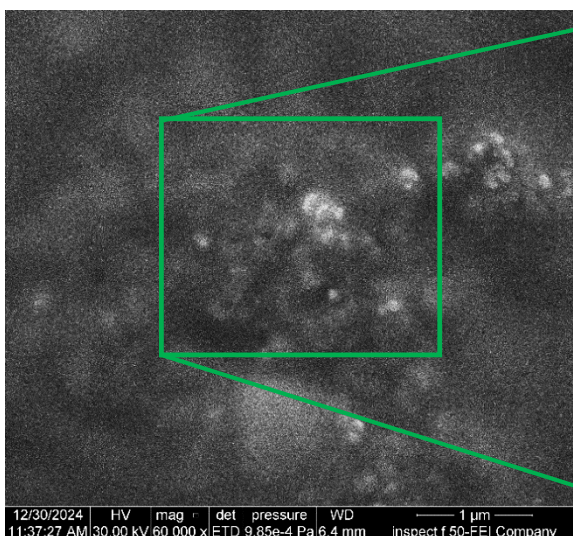
monomer in the PVP matrix. The surface morphology shows smooth regions attributed to the presence of PVP polymer and rough (bumpy) regions, reflecting the formation of complexes and deposition on ITO. This structure is responsible for the high ionic conductivity, a distinctive feature in sensors [144].



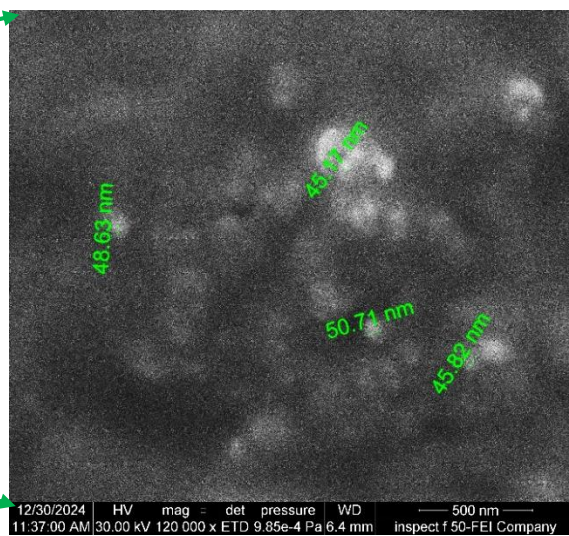
S1



S1



S2



S2

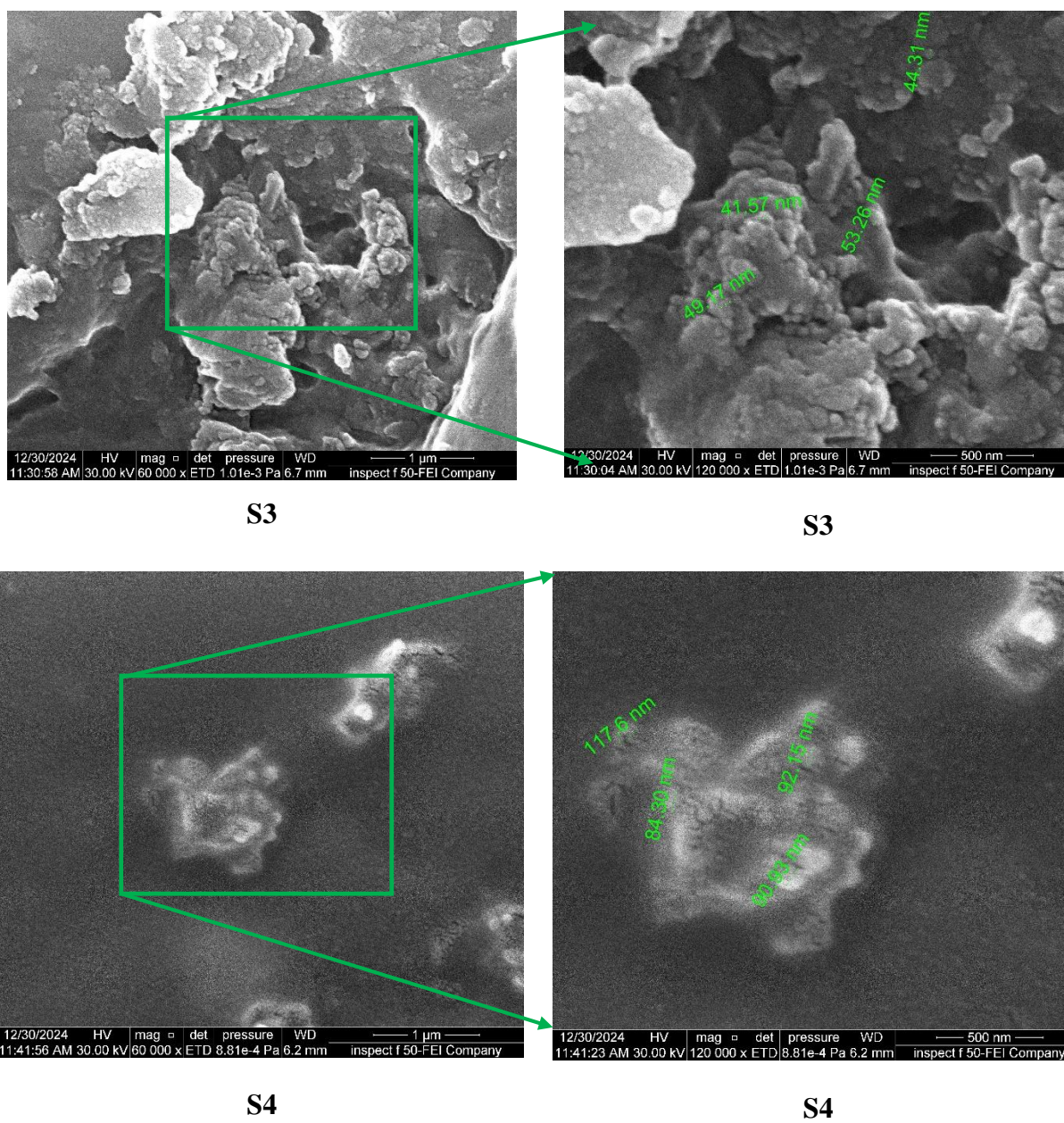


Figure (4-1). FE-SEM images of samples with two different magnifications (left-microsize) and (right-nanosize) .

4.2.2 FTIR measurement

The Fourier transform infrared spectrum is revealed in Figure (4-2) for samples (S1, S2, S3, and S4) representing pure polymer PVP, polymer blend PVP-PPY, PVP-PPY/GO, and PVP-PPY/GO@ITO NCs. S1 revealed a peak at 3019 cm^{-1} , related to C-H stretching. Peaks 1672 cm^{-1} associated with C=O stretching, 1423 cm^{-1} related to the pyrrolidinyl group, and 1214 cm^{-1} linked with C-N vibrations [142,143]. Peaks under 800 cm^{-1} , such as 743 and 667 cm^{-1} , originate from the C-H and N-H out-of-plane degrees of freedom. The addition of PPY results in a broad peak around 3385 cm^{-1} , indicating the presence of hydroxyl (O-H) and amine (N-H) bonds in the sample [147]. The hydroxyl groups could arise from moisture absorption, residual water, solvents, or from the chemical structure of the PVP polymer, which has the ability to absorb water. On the other hand, the amino bonds are attributed to the PPY polymer, which contains nitrogen-rich pyrrole rings [148]. The overlap in absorption between these bonds results in this broad peak, which is attributed to hydrogen bonding between these groups within the mixed polymer structure. This broad absorption indicates strong interactions between the components, which enhances the physical properties of the material. Furthermore, a shift was observed in most of the PVP peaks for the same reason, which is consistent with the results of previous studies [149].

The appearance of similar peaks 1214 , 743 , and 667 cm^{-1} in the polymer and nanocomposite mixture has identical peaks with those associated with the FTIR spectrum of pure PVP-k30 polymer due to its containing strong functional groups that absorb in specific infrared ranges when mixed with PPY polymer, their peaks overlap, or the PVP peaks remain dominant, which makes the overall spectrum similar [150], in addition to the functional groups (hydroxyl and carboxyl) present in graphene oxide, which overlap with the polymer peaks. These are difficult to

distinguish in the spectrum [151]. At the same time, indium and tin oxides are inorganic nanomaterials that do not contain functional groups that absorb in the FTIR range, which explains the absence of new peaks in sample S4 [152].

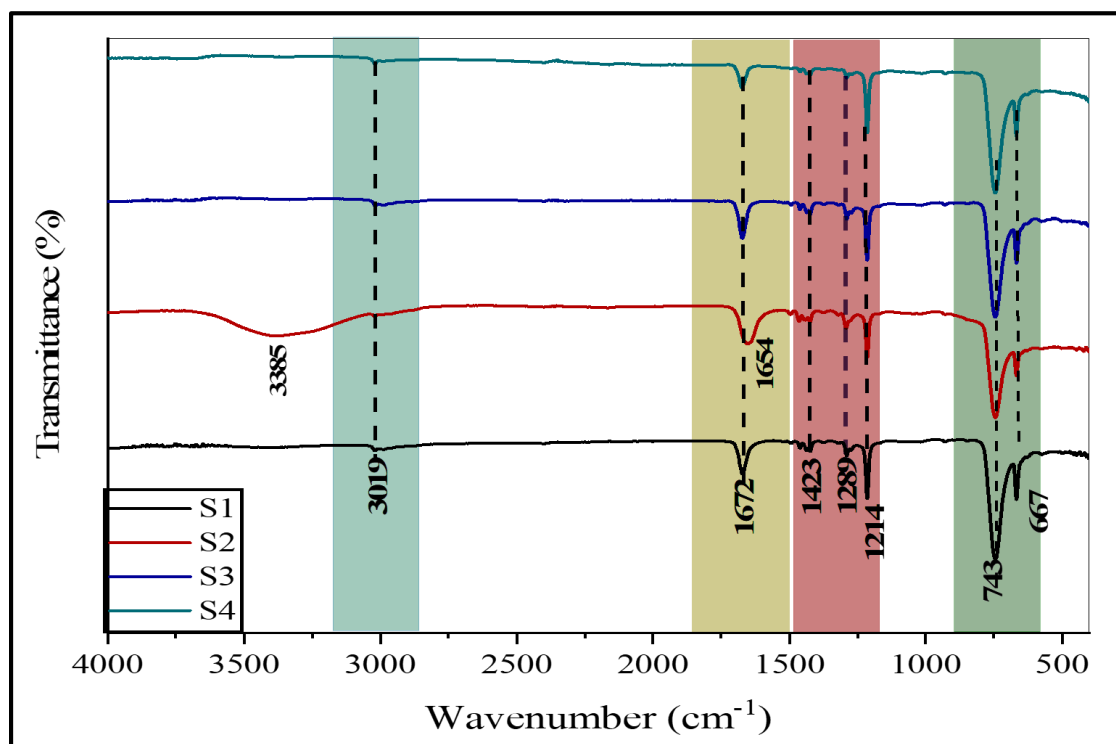


Figure (4-2). Samples FTIR spectra at the wave number.

4.2.3 X-Ray diffraction measurement

Figure (4-3) shows four samples' X-ray diffraction (XRD) patterns to study the effect of incorporating different materials on the structural composition. Sample S1 showed broad peaks at 11.4° and 21.6° , indicating the semicrystalline nature of the PVP polymer [153]. Upon the addition of PPY to sample S2, the spectrum revealed slight shifts in the peak positions (10.9° and 21.9°), indicating an interaction between PVP and PPY without effect on the semicrystalline behavior of PVP polymers [154]. In sample S3, which contains PVP and PPY with graphene oxide (GO), additional

peaks appeared at 22.3° , 29.6° , and 31.2° , indicating new layered interaction and stacking resulting from the presence of GO [155]. Moreover, the introduction of GO in S3 results in the appearance of a sharp peak at $\sim 10^{\circ}$ – 12° (2θ), corresponding to the (002) plane of GO, superimposed on the semicrystalline polymer background, remove the space confirming the successful formation of the PVP-PPY/GO nanocomposite. Sample S4, which represents the (PVP-PPY/GO-ITO) nanocomposite, showed a distinct peak at 22.64° with a decrease in the other peaks, reflecting a change in the structural composition due to the introduction of crystalline ITO phase, which indicates the effective ITO to confirm the successful formation of the PVP-PPY/GO-ITO nanocomposite [156]. These findings demonstrate the progressive structural evolution of semi-crystalline polymers without impact on the main behavior, in contrast, the shifting confirmed the strong impacting on the interfacial interaction of components in the NCs, corroborating the successful synthesis of the hybrid materials. The FTIR results strongly support this finding.

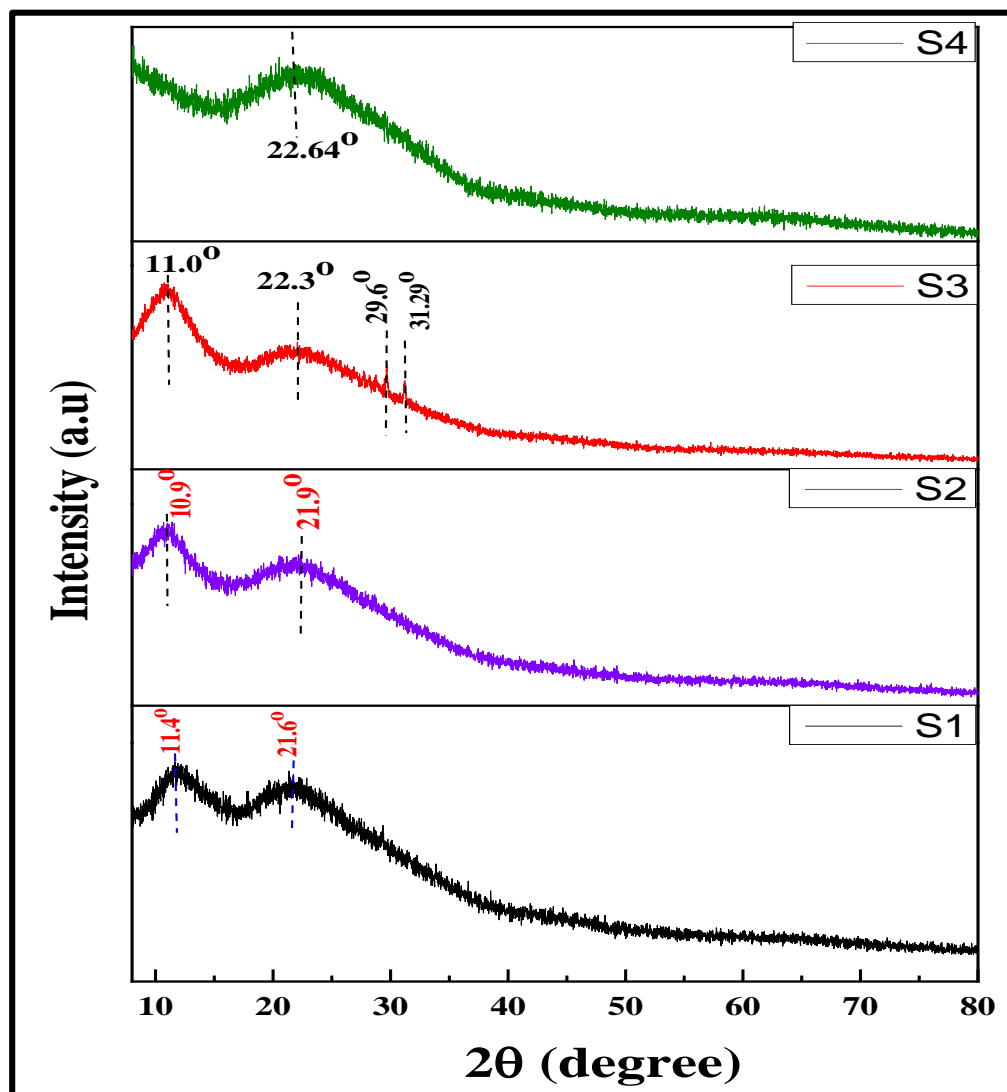


Figure (4-3). XRD patterns for the samples.

There is a significant link between the FE-SEM and XRD, where X-ray diffraction (XRD) reveals changes in the material's atomic arrangement and crystal structure. At the same time, FE-SEM images confirm these changes through direct imaging of the sample surface and high-resolution particle distribution. Sample S1 demonstrates the semicrystalline nature of the PVP k30 polymer through peaks at 11.4° and 21.6° . FE-SEM images confirm this result through a smooth and

homogeneous surface with some cracks resulting from sample drying. In sample S2, peaks 10.9° and 21.9° shift slightly due to the good interaction between the PVP-PPY polymers. FE-SEM images reveal a high homogeneity on the surface without agglomerations or cracks, indicating good overlap of the two polymers. In sample S3, XRD reveals new peaks at 22.3° , 29.6° , and 31.2° , resulting from adding graphene oxide nanoparticles, creating a good stacking pattern across the layers.

FE-SEM confirms the effect of graphene oxide nanosheets on the sample through the appearance of flakes and clusters on the surface, representing the sheets or edges of this nanomaterial, making the surface appear more complex and intertwined. X-ray diffraction (XRD) of sample S4 reveals a clear and strong peak at 22.64° , while the remaining peaks are subdued. This explains the effect of adding indium tin oxide nanoparticles, which significantly changed the structural composition and created a fine final structure. This result was confirmed by scanning electron microscopy (FE-SEM) images, which revealed larger and irregular particles on the surface. This result confirms the effect of indium tin oxide nanoparticles on a less homogeneous surface with significantly improved functional properties.

4.3 Optical Properties

4.3.1 Absorbance

Figure (4-4) illustrates the absorbance of four samples (S1 to S4) over various wavelengths (290-890 nm). Spectrophotometers with double beams were used to measure the films at room temperature for all measurements. A material exhibits greater absorption efficiency at shorter wavelengths (ultraviolet region), whereas an

increase in wavelength reduces absorbance across all samples. This indicates high transparency due to the absence of significant light-absorbing materials in the transparent PVP polymer, such as conjugated double bonds [157]. The maximum absorption peak equal to 1 ($\lambda_{\text{max}}=290$ nm) lies in the range 200-300 nm, i.e., in the ultraviolet (UV) region, which typically corresponds to the following electronic transition $\pi \rightarrow \pi^*$. It occurs in molecules with conjugated double bonds (C=C) and aromatic systems in (PPY) and conjugated π -system in PPY and GO [158,159]. This may result from the interactions between ultraviolet light and functional groups, such as the lactam group [160].

The blend of the PVP-PPY film absorbs about 0.34 of the photons at 390 nm. Sample S2 exhibits more absorbance than S1 across all wavelengths, with a notable enhancement up to 0.70 at lower wavelengths (310 nm) attributed to the conductive PPY polymer, which considerably absorbs light at shorter wavelengths owing to its conjugated double bonds. The donor electrons were excited to the conduction band at these energies; when an electron absorbed a photon with a known energy, it excited the electrons to a higher energy level. In addition, the findings showed that the samples absorbed a significant amount of UV light. Because of this, it is now known that these photons have the energy to interact with atoms. An electron's potential transitions may be studied by looking at the changes in transmitted and absorbed energy, shown by the fundamental absorption in absorbance spectra [161]. The contribution of GO nanosheets also improves the absorption of the photons. In contribution to the GO nanosheets, the absorption has reached a higher value than the PVP and PVP-PPY samples. Here, the interaction between materials and incoming photons will be seen, boosting the absorption of incident light by free electrons. Also, an absorbance of 2.3% per nanoflack is possible in graphene

nanosheets. In sample S4, the nanocomposite PVP- PPY/GO@ITO exhibits the highest absorbance at low wavelengths and adsorbs up to 0.85 at 390 nm compared with all other samples. This is attributable to the addition of ITO conductive nanomaterial. Moreover, another clear sign of the contribution of loading ITO, revealed small peaks or features at 410 and 450 nm, agrees with the literature [162].

The charge carrier's density increased due to its fine-grained dispersion in the matrix, which enhances light absorption across a broad spectrum of wavelengths. Additionally, the synergistic effect between graphene oxide (GO) and ITO significantly amplifies absorption, as all nanomaterials effectively absorb light across varying ranges. In contrast, the absorbance of all NCs was improved in the visible spectrum. Even though the samples showed significant improvement at higher wavenumbers, the absorption values from the photons of all samples started to be steady after 390 nm, where S1 revealed a low absorption of about 0.06, which significantly improved to 0.34 after blending PPY with PVP. This absorption value increased with the contribution of GO to 0.61, and then it was notably enhanced to 0.85 with the loading of ITO.

However, the nanocomposite revealed a gradual reduction in these values with increasing wave number, whereas the polymer sample was studied in detail. The incoming photons lack the energy necessary to interact with atoms at high enough wavelengths, which may explain this phenomenon [163]. In addition, the findings showed that the samples absorbed a significant amount of UV light [31]. Because of this, it is now known that these photons have the energy to interact with atoms. An electron's potential transitions may be studied by looking at the changes in transmitted and absorbed energy, shown by the fundamental absorption in

absorbance spectra [161]. Interestingly, this improvement of absorption behavior was presented in both areas with low and higher wavenumbers, which presented interesting materials in a broad range of wavenumbers for promising applications such as optoelectronic, optical filters, sensors, etc.

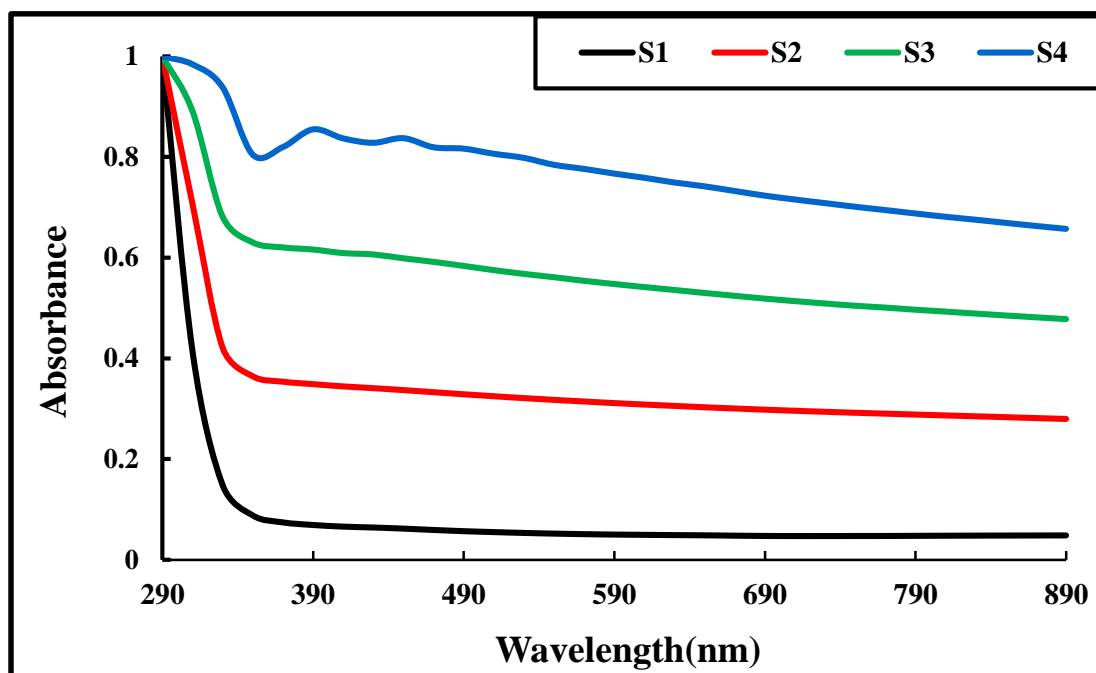
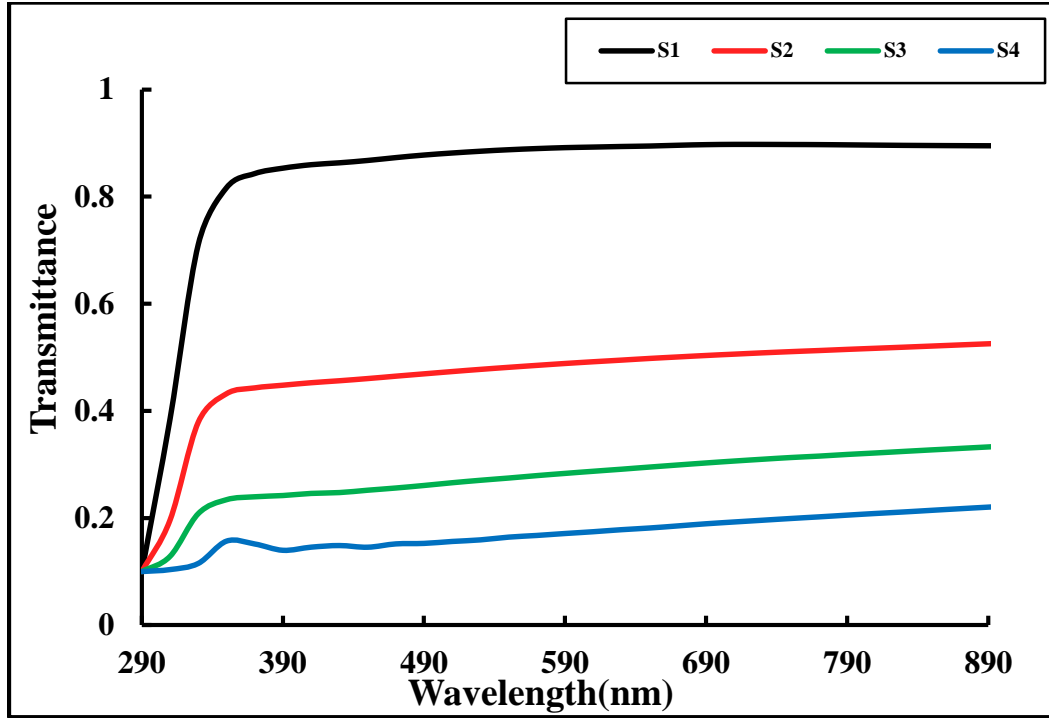


Figure (4-4). The Absorbance Spectra with the Wavelength of S1 to S4 Nanocomposite.

4. 3.2 Transmittance

Figure (4-5) shows how the transmittance (T) spectra vary with sample wavelength. We observe that the transmittance of all samples increases sharply after 290 nm and stays relatively constant beyond 390 nm as the wavelength increases. Results show that GO significantly decreased light transmittance in the PVP-PPY/GO@ITO nanocomposite. This behavior was increased by adding the ITO to the matrix, where an increase in nanomaterials may cause a decrease in

transmittance and an increase in light absorption [164]. Using Equation (2.10), the permeability T is calculated [165].



Figure(4-5). The transmittance spectra of the samples.

4.3.3 Absorption coefficient

Figure (4-6) illustrates the absorption coefficient (α) of the four sample films as a function of photon energy. As the photon energy increased, the absorption coefficient steadily enhanced in value up to 3 eV. This may pertain to the lower electron transition, whereby the energy of the incoming photon in this range was insufficient to elevate the electron from the valence band to the conduction band. S3 demonstrates enhanced absorption relative to S1 and S2, particularly in the intermediate energy range ($\sim 2.8 - 3.8$ eV), with a fast rise seen across all sample

results attributable to significant electron transitions in the conduction band. In sample 4, the homogenous distribution of GO on the ITO surface results in an enhanced density of active sites for absorption.

PPY is near the leading absorption edge, and films and NCs are known to be very absorbent when exposed to the absorption coefficient (α), which is calculated by Equation (2-12) [166].

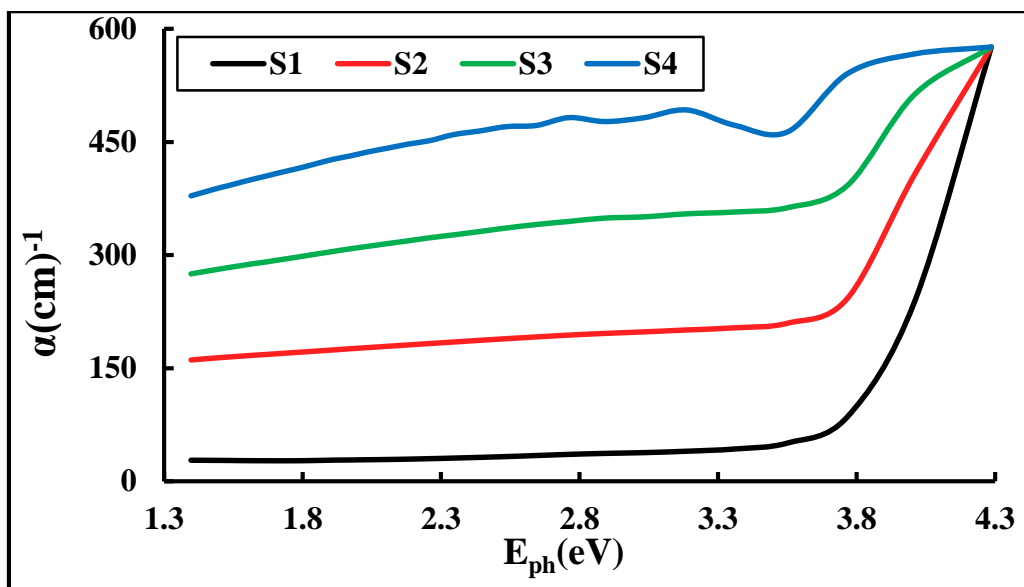


Figure (4-6). The relation between photon energy and the absorption coefficient of samples.

4.3.4 Optical energy gap

Equation (2.13) determines the permitted and prohibited indirect transition band energy gaps. The optical investigation findings of PPY-doped PVP blend polymers indicated the potential for band gap modulation by appropriate doping with the conducting polymer, PPY. The expansive PVP polymer blend film is seen to be transformed into a tiny bandgap polymer blend film via doping with PPY and nanomaterials, which is also an environmentally friendly and biocompatible polymer [167].

Figure (4-7) demonstrates the absorption edge $(\alpha h\nu)^{1/2}$ for samples. Plotting NCs against photon energy and drawing a straight line from the peak to the x-axis at the point where $(\alpha h\nu)^{1/2} = 0$ is used to determine the energy gap for the permitted indirect transition. Using GO and ITO nanoparticles could reveal a reduction in the energy gap values. The formation of site levels in the forbidden energy gap happens in two steps during the transition, during which electrons go from the valence band to the local levels and finally to the conduction band [168].

NCs are heterogeneous (i.e., electronic conduction depends on added concentration). This behavior is explained by adding ITO nanoparticles, which create electronic pathways in the polymer, allowing electrons to cross from the valance band to the conduction band. The results revealed that the forbidden transition of the indirect energy gap for the prohibited transition is identical to the indirect energy gap for the samples, as shown in Figure (4-8). Consequently, the energy gap decreases after the effective contribution of GO and ITO nanomaterials, as presented in table (4-1). Consistent with the same behavior in previous studies, these findings [169]. These results are promising for optoelectronic applications.

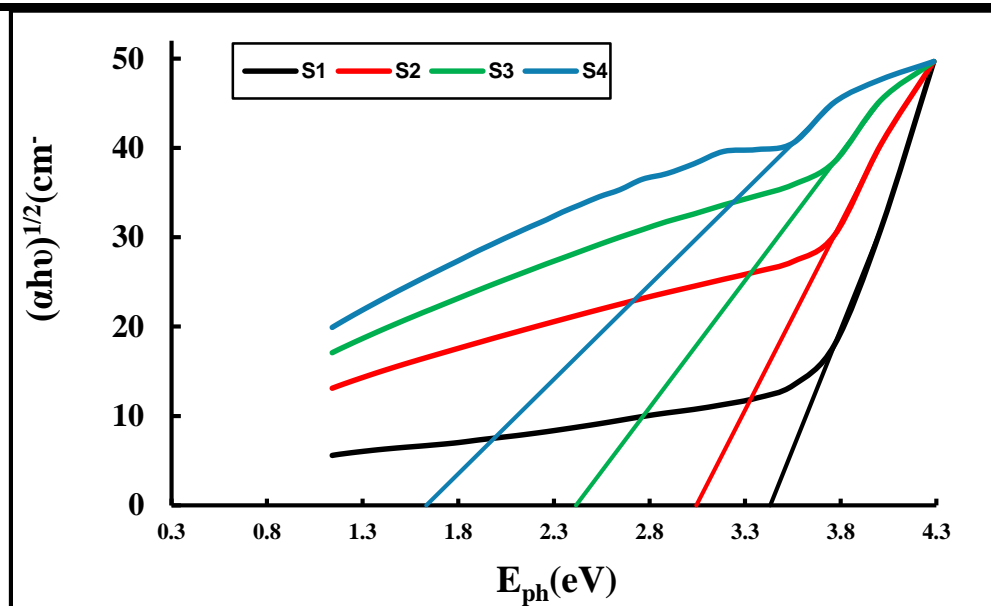


Figure (4-7). The optical energy band gap $(\alpha h\nu)^{1/2}$ of allowed indirect transition for samples versus E_{ph} .

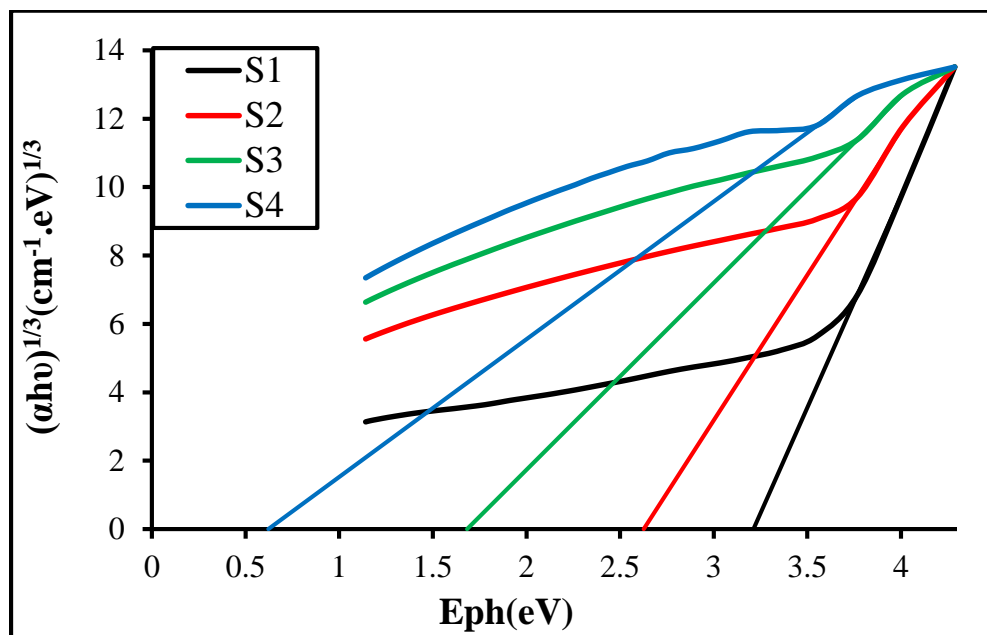


Figure (4-8). The energy band gap $(\alpha h\nu)^{1/3}$ of the forbidden indirect transition for samples versus E_{ph} .

Table (4-1). Energy gap of the indirect allowed and forbidden transitions for the samples.

Samples	Allowed	Forbidden
S1	3.43	3.21
S2	3.04	2.62
S3	2.41	1.68
S4	1.63	0.62

The optical properties of materials, such as light absorption and bandgap, significantly and directly impact enhancing the antibacterial efficacy of photoactive materials, particularly optically active materials (photoactive materials).

These materials contribute to the generation of reactive species capable of inhibiting bacteria. There is a positive correlation between a material's photo activity and its antibacterial efficacy [170]. When optically active materials, such as GO-ITO nanomaterials, absorb light, electrons move between the valence and conduction bands, generating electron-hole pairs (e^-/h^+ pairs). These pairs react with the surrounding water and oxygen to produce active oxygen species such as hydroxyl radicals ($\bullet OH$), superoxide anions ($O_2^{\bullet -}$), and hydrogen peroxide (H_2O_2). The smaller the energy gap, the greater the material's ability to absorb light and produce active species with high efficiency. When hybrid materials such as (GO-ITO) are added, it increases electron transfer and reduces the energy gap, improving light absorption. Consequently, ROS increases, and thus, the active species damage the

bacterial cell wall, destroying proteins and DNA inside the cell, which leads to bacterial inhibition [171,172].

According to the findings of absorbance and transmittance, the prospective applications are as follows: Applications necessitating the absorption of ultraviolet (UV) photons exhibit significant absorption at short wavelengths. It is used in thermal insulation applications because of its high absorption and reduced transmittance at long wavelengths (infrared). In addition to optical protection applications, its medium transmittance in the visible light spectrum makes it appropriate for use as a protective coating or optical insulator for visible light spectrum and photocurrent generation. This combination makes it a versatile material suitable for various optoelectronic sensors, optical filters, etc., and photothermal applications that can kill bacteria.

4.3.5 Refraction index

Figure (4-9) shows the change in refractive index versus wavelength for samples S1, S2, S3, and S4. It is worth noting that the refractive index increased to 2.39 at 310 nm in the UV region for sample S3. The GO-ITO contribution significantly improved the refractive index results in the short wavelength region, reaching 2.67. The remarkable increase in the refractive index is attributed to addition two nanomaterials to the PVP-PPY/GO-ITO nanocomposite of sample S4. The addition of ITO to the NCs is responsible for the remarkable increase in the refractive index, as it improves the crystalline structure of the samples prepared after doping with the nanomaterial and becomes stable at higher wavelengths. The graph shows that as the wavelength of light increases, the refractive index of the NCs decreases [131].

This phenomenon can be explained by the fact that the speed of light decreases with increasing wavelength. As the speed of light decreases, the refractive index decreases. This relationship between wavelength and refractive index in optics is called refractive index dispersion [132]. As the wavelength of light increases, the refractive index of NCs decreases [131]. The refractive index is calculated from Equation (2.14).

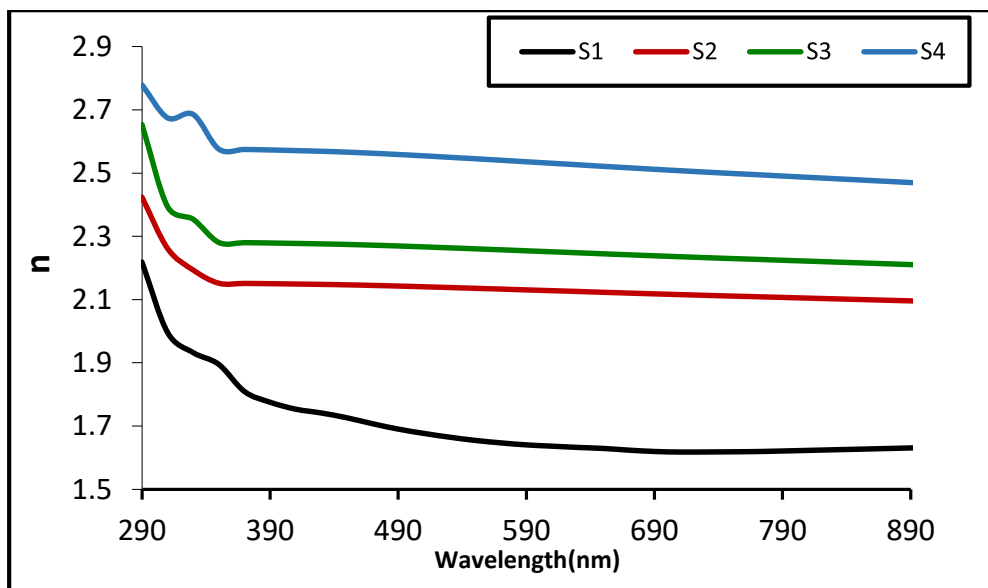


Figure (4-9). The refractive index (n) of S1-S4.

4.3.6 The extinction coefficient

Figure (4-10) reveals the wavelength-dependent behavior of the samples' extinction coefficient (K). As the wavelength of incident light increases in the UV region, the extinction coefficient of the S3 and S4 NCs increases due to the high absorption in this region [129]. Then, the extinction coefficient value of each nanocomposite begins to gradually increase in the visible light region to the near-infrared, i.e., from 400 to 890 nm, which records the highest value, especially for samples S3 and S4. The extinction coefficient

changes with wavelength according to Equation (2.15). These results show that the structure properties adding ITO nanoparticles to the PVP-PPY/GO-ITO nanocomposite significantly improved the behavior of the NCs.

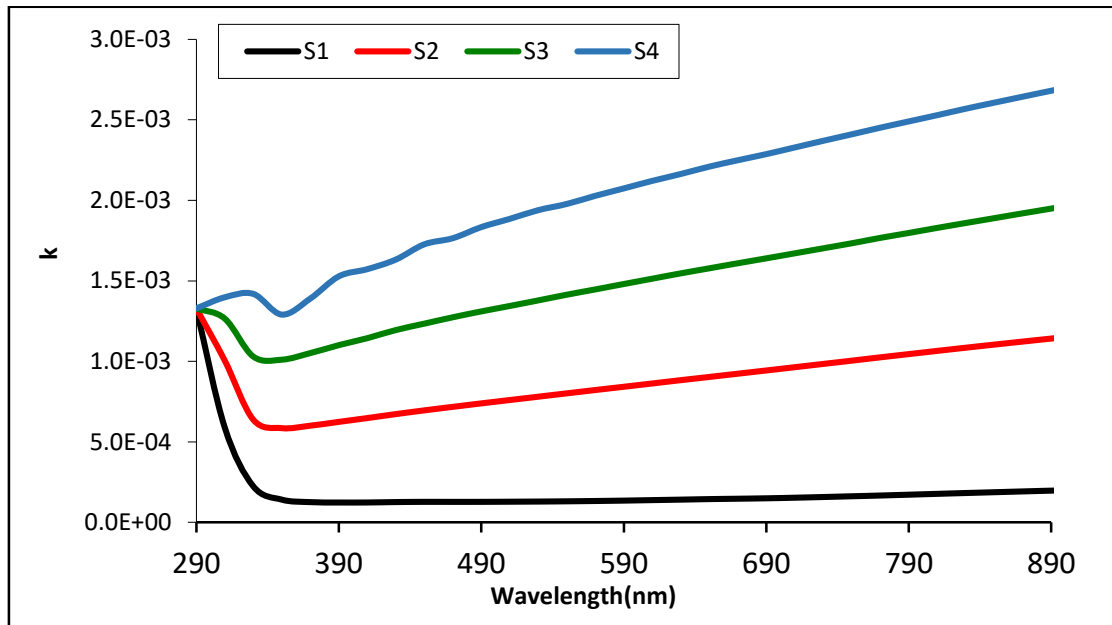


Figure (4-10). Extinction coefficient versus wavelength for samples S1-S4.

4.3.7 The real and imaginary dielectric constant

Figures (4-11) and (4.12) show the variation of the real and imaginary parts of the dielectric constant (ϵ_1) and (ϵ_2), respectively, with wavelength for all samples: S1, S2, S3, and S4. The real part of the dielectric constant resembles the behavior of the refractive index (n), indicating that the values of both curves increase with the increase of nanoparticles [173]. The nature of the curve remained unchanged in almost all samples. However, a shift in the peak position occurred at a wavelength

of 290 nm, accompanied by a stabilization of the values outside this wavelength. An increase was also observed with the incorporation of multiple GO-ITO nanoparticles. This results from the high density of dipoles resulting from the incorporation of nanomaterials, which enhances the optical polarization and

Refractive index. As a result, the real part of the dielectric constant increases, which is agreed upon by researchers [174]. The imaginary component of the dielectric constant of NCs is mainly proportional to the extinction coefficient (k), which is related to the absorption coefficient of the NCs [175]. Figure (2-12) shows the effect of nanoparticles (ITO, GO) on the imaginary component of the dielectric constant (ϵ_2), indicating that the imaginary part of the dielectric constant of NCs increases with the incorporation of different nanoparticles. This increase is attributed to the higher absorption coefficient of the NCs, which consequently enhances the imaginary component of the dielectric constant. Graphene oxide enhances the imaginary dielectric constant values across all wavelengths and causes the curves' fundamental absorption edge (peak) to shift toward 330 nm for the S4 sample.

The incorporation of nanomaterial atoms into the crystal lattice of the blended polymer may lead to the introduction of new energy levels within the forbidden gap, which leads to the enhancement of the polarization of the diode and the increase of the energy absorption ratio of the incident radiation, and thus the increase of the dielectric constant of the imaginary part (ϵ_2) from which the real and imaginary part of the dielectric constant are calculated [176].

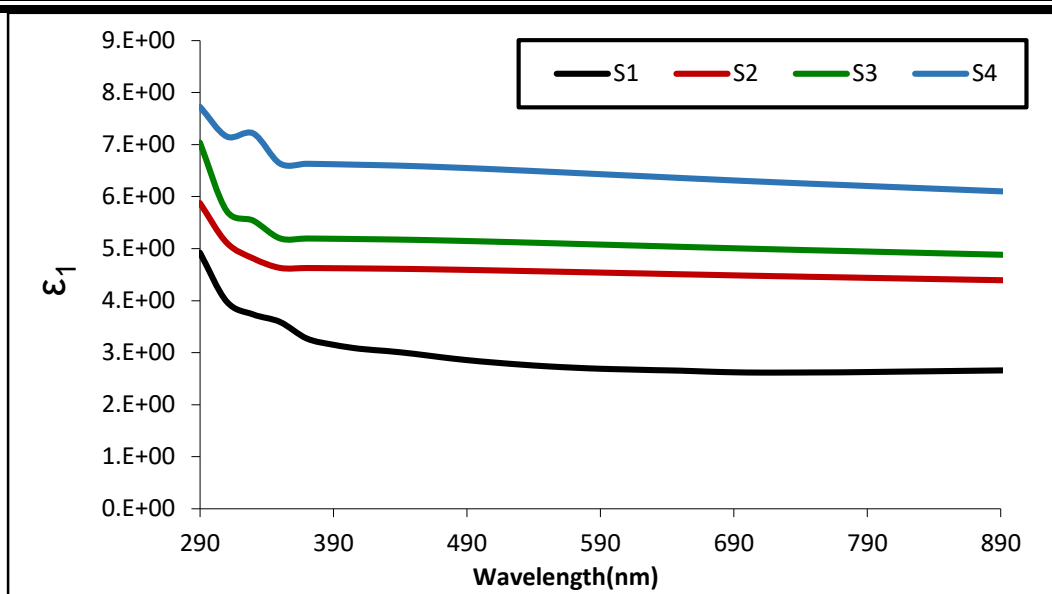


Figure (4-11). Real dielectric constant with wavelength for samples.

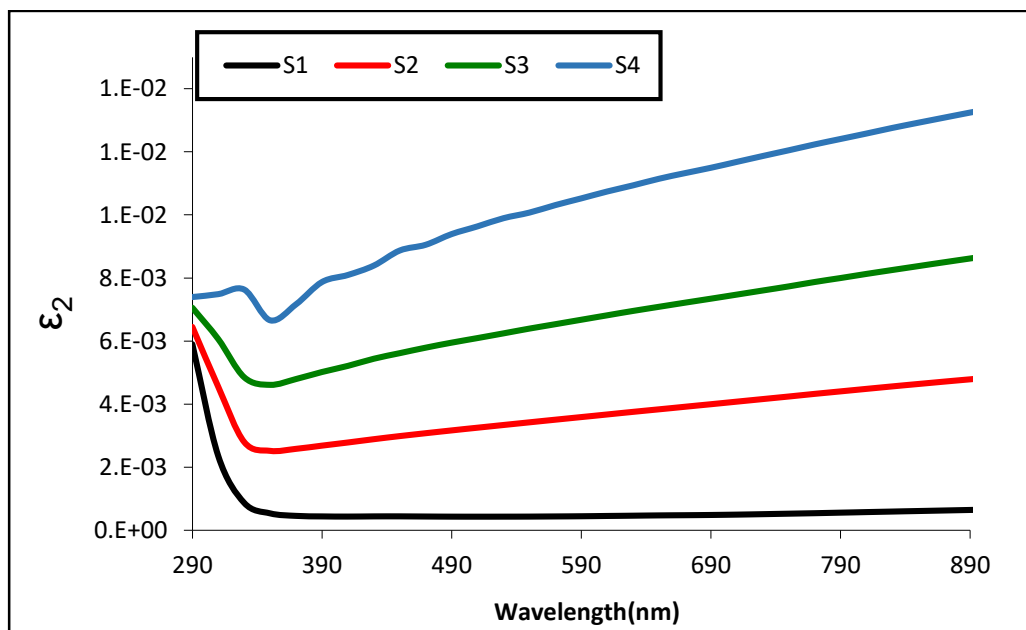


Figure (4-12). Imaginary dielectric constant with wavelength for samples.

4.3.8 Optical conductivity (σ_{op})

Researchers often consider the optical conductivity of a material when studying its optical response through the Equation (2.19). The optical conductivity of all samples, S1, S2, S3, S4 was studied as a function of wavelength, as shown in Figure (4-13), The photoconductivity values at these wavelengths are recorded in Table (4-2). The results reveal that the optical conductivity of samples S3 and S4 increases when different ITO and GO nanoparticles are added. This result is attributed to the formation of localized levels in the energy range, which increases the absorption coefficient and, thus, the optical conductivity of the NCs [177].

Table (4-2). Optical conductivity values at short, medium, and high wavelengths.

Sample	Optical Conductivity (s^{-1})		
ID	290 nm	600 nm	800 nm
S1	2.1E ⁺¹²	1.1E ⁺¹¹	1.0E ⁺¹¹
S2	2.19E ⁺¹²	9.1E ⁺¹¹	8.3E ⁺¹¹
S3	2.93E ⁺¹²	1.6E ⁺¹²	1.5E ⁺¹²
S4	3.6 E ⁺¹²	2.6E ⁺¹²	2.3E ⁺¹²

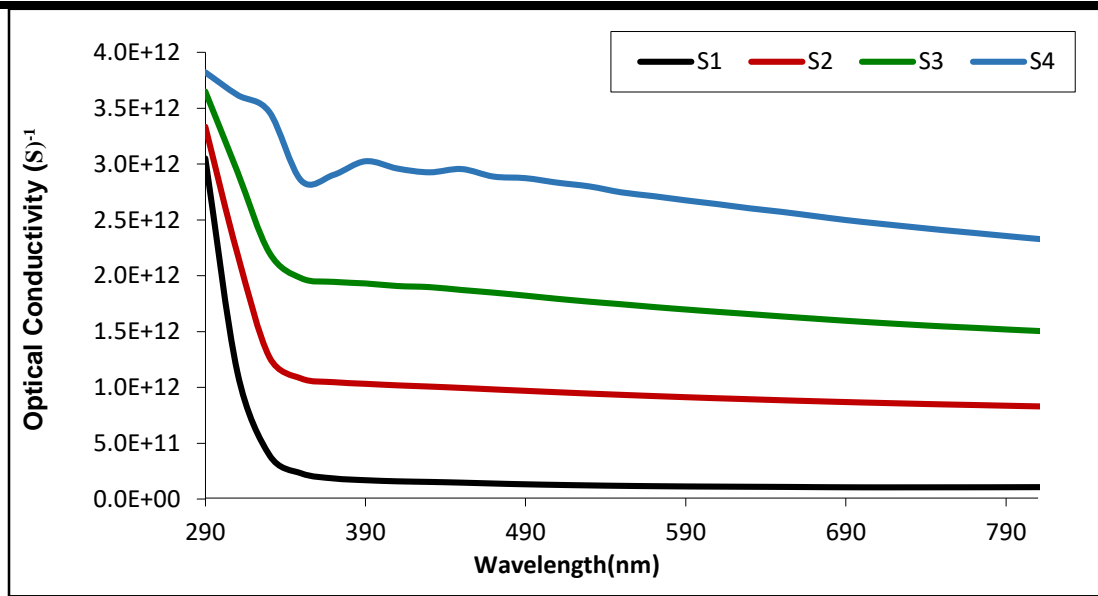


Figure (4-13). Optical conductivity with the incident photon wavelength for samples.

4.4 The A.C electrical properties

4.4.1 Dielectric constant

The A.C. electrical properties of the four samples S1,S2,S3,S4 were studied at frequencies $[1 \times 10^2 - 5 \times 10^6]$ Hz. The dielectric constant is the divided ratio between the dielectric capacitor (C_p) and the vacuum capacitor (C_o), as revealed in Equation (2-22) [178]. In materials, the dielectric constant depends on the chemical composition and the response to an electric field. The prepared films exhibit high dielectric constant values at low frequencies due to surface polarization. Figure (4-14a) shows that sample S1 has the lowest dielectric constant value of 2.16 because the pure PVP polymer is an insulator.

The addition of a conductive polymer such as PPY to the dielectric polymer in sample S2 increases the polarization, thereby enhancing electron conduction and thus improving the electrical properties, with a dielectric constant value of 2.94 [179]. Sample S3 showed an increase in the dielectric constant of 4.07 due to the addition of graphene oxide, which contains polar functional groups that interact with the polymer blend chains and the electric field. The addition of indium tin oxide to sample S4 creates a superior dielectric system compared to all other samples due to the transparency of this nanomaterial, making it a good conductor that interacts strongly with the electric field, thus increasing the dielectric constant of 4.63 [23].

In general, the dielectric constant value decreased with increasing electric field frequency for all four samples due to the short period, which was less than the period required for the molecules to rearrange toward the external electric field. Ionic and electronic polarization strongly affect the dielectric constant because they follow the rotation of the external electric field, which reduces the polarization, thus decreasing the dielectric constant. Meanwhile, the phase difference between the base material and the added nanomaterials led to interface polarization, which improved the dielectric constant, as shown in Figure (4-14b). The polarization resulting from the electrodes depends on the charge composition between the electrodes and the composition and spacing of the samples [180].

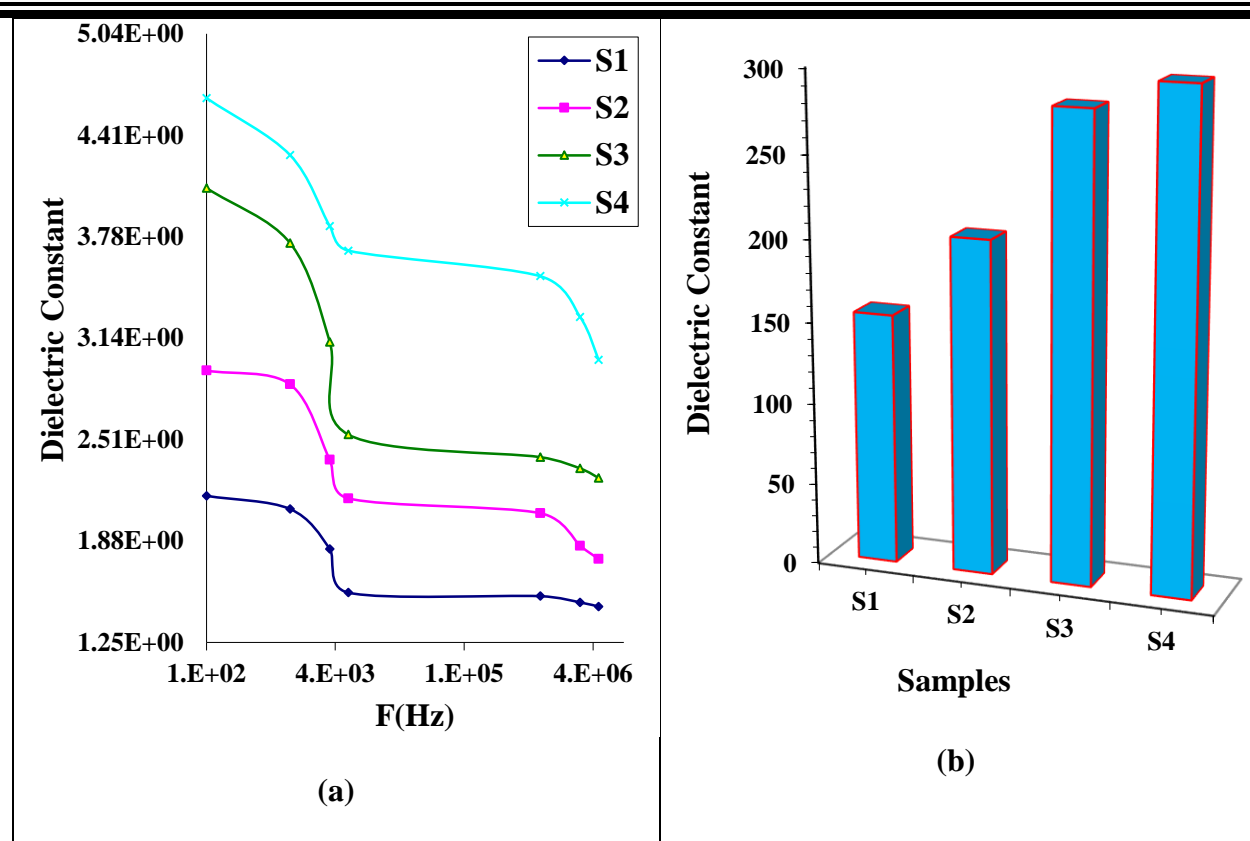


Figure (4-14). The dielectric constant versus (a) frequency and (b) impact of PPY, GO, and GO@ITO nanomaterials in nanocomposites.

4.4.2 The dielectric loss

Figure (4-15a), (4-15b) displays the dielectric loss (ϵ'') values versus the electric field frequency for the four prepared samples that were calculated from Equation (2.23) [181]. At high frequencies, the dielectric loss decreased in all samples due to the polarization effect, which reduced with increasing electric field frequency. The contribution of PPY and nanomaterials to the PVP-PPY/GO @ITO polymer mixture revealed notable improvement in the dielectric loss through the rise in charge carriers, which form a connected complex network in the NCs [182]. The results showed a gradual improvement in the dielectric constant and AC conductivity from sample S1 to S4, resulting from the synergistic integration of conductive polymers and nanomaterials within the PVP matrix. PPY contributed to enhanced polarization

and charge transport, while GO added surface effects and enhanced electric field response due to the zero band gap of graphene [173]. The introduction of ITO into sample S4 resulted in the highest electrical performance due to its high conductivity. This improvement is attributed to increased polarization and the formation of an interconnected charge network, making these materials promising for flexible electronics and sensor applications [183].

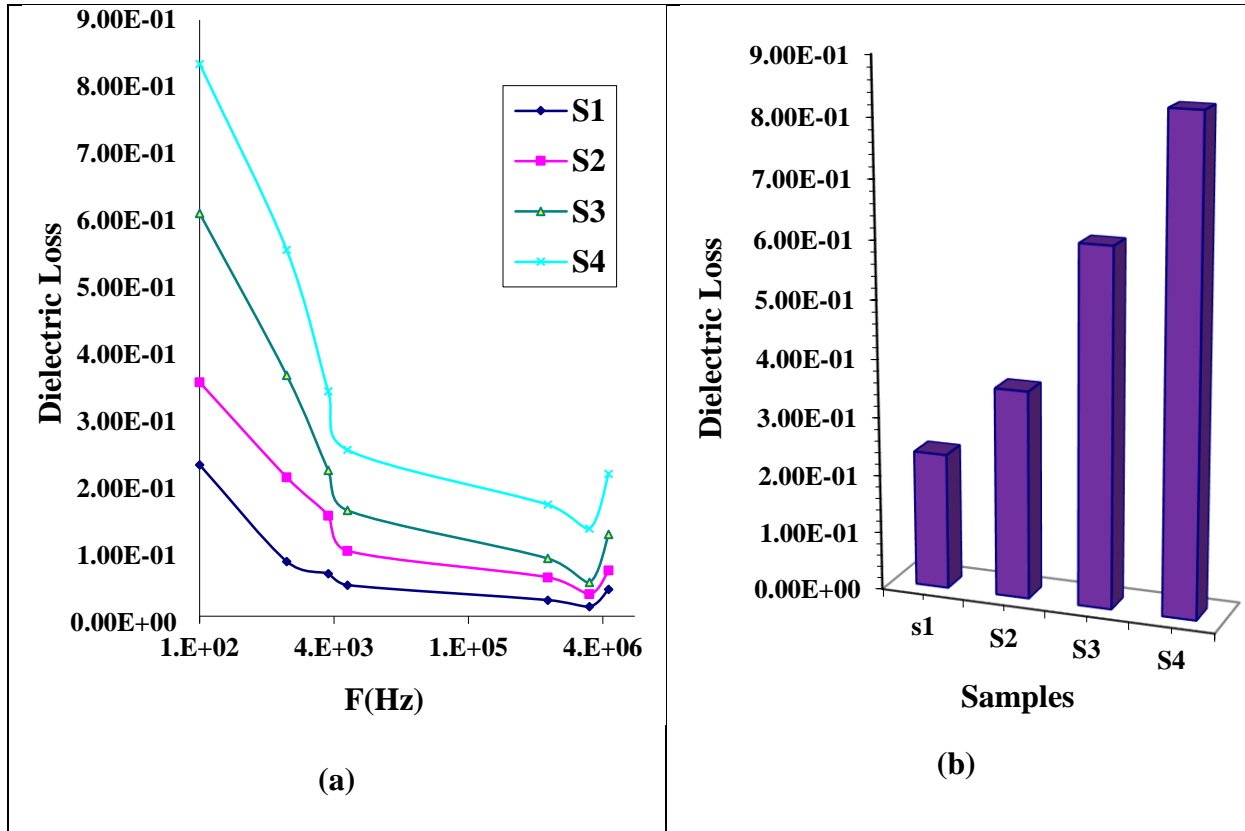


Figure (4-15). Dielectric loss versus (a) frequency and (b) impact of PPY, GO, and GO@ITO nanomaterials in nanocomposites.

4.4.3 Electrical conductivity

The electrical conductivity ($\sigma_{ac}(\omega)$) of the prepared nanocomposite films at room temperature is calculated according to Equation (2.24) [184]. It shows a significant direct enhancement in electrical conductivity for all samples with the

electric field frequency, as shown in Figure (4-16 a). The addition of nanomaterials enhances the increase in electrical conductivity values with high frequency when incorporating PPY, a conductive polymer with a conjugated π -electron system that facilitates electron transport. Whereas the contribution of GO and ITO revealed the most notable improvement due to the synergistic amplification of the polarization of charges and the excitation of a more significant number of charge carriers by creating additional channels to transfer charges from the valence band to the high band in conduction band [185], as displayed in Figure (4-16 b).

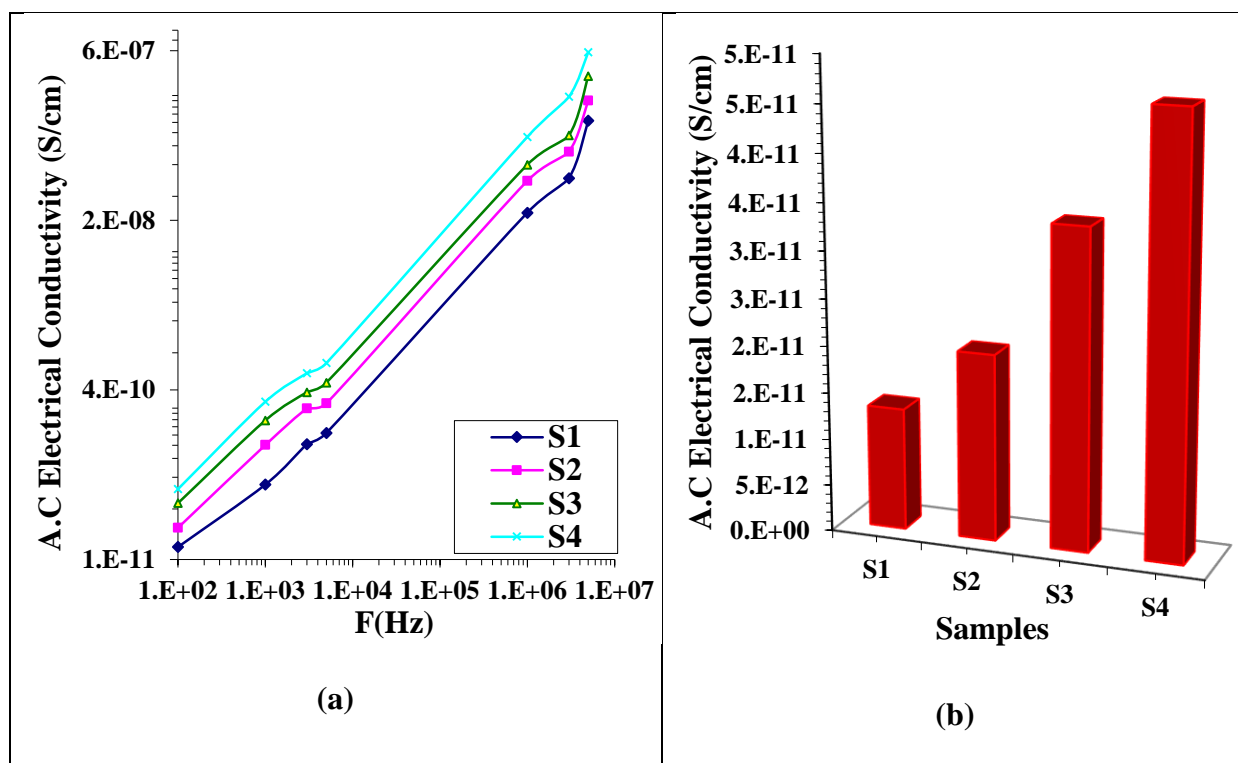


Figure (4-16). Electrical conductivity versus (a) frequency and (b) impact of PPY, GO, and GO@ITO nanomaterials in nanocomposites.

Improving the dielectric properties of the nanocomposite plays a pivotal role in enhancing the efficiency of the sensing system. A high dielectric constant indicates the material's ability to store electrical charge and its rapid response to changes in

the electric field resulting from the adsorption of gases on the sensor surface [186]. This enhances the system's sensitivity to target gases by amplifying signals generated by surface interactions, enabling a clearer and faster response [187]. In addition, a high dielectric constant contributes to reducing the interfacial resistance between the conductive nanoparticles, which improves electrical current transmission within the composite structure and increases the stability of the electrical signal [188]. Thus, improved dielectric properties are an important indicator of the effectiveness of the sensor system and its ability to operate efficiently, even in low-concentration operating conditions or complex environments [189].

4.5 Applications

4.5.1 Oxidizing NO₂ gas and reducing NH₃ gas sensing

Figure (4-17) shows the electrical resistance as a function of time recorded for the prepared nanofilm sensor sample S4 (PVP-PPY/GO@ITO) in less than 10 seconds for open and closed ammonia gas vapor at a constant concentration of 150 ppm utilized in ambient air presented into the test chamber using a needle valve and at different temperatures (25, 150, and 250 °C). A digital multimeter model Vector 70C was responsible for the interface to perform the measurements. Before turning on the gas, the electrical resistance was repeatedly checked and stabilized over time, as the resistance is directly proportional to the operating time of ammonia gas and decreases when the gas is turned off.

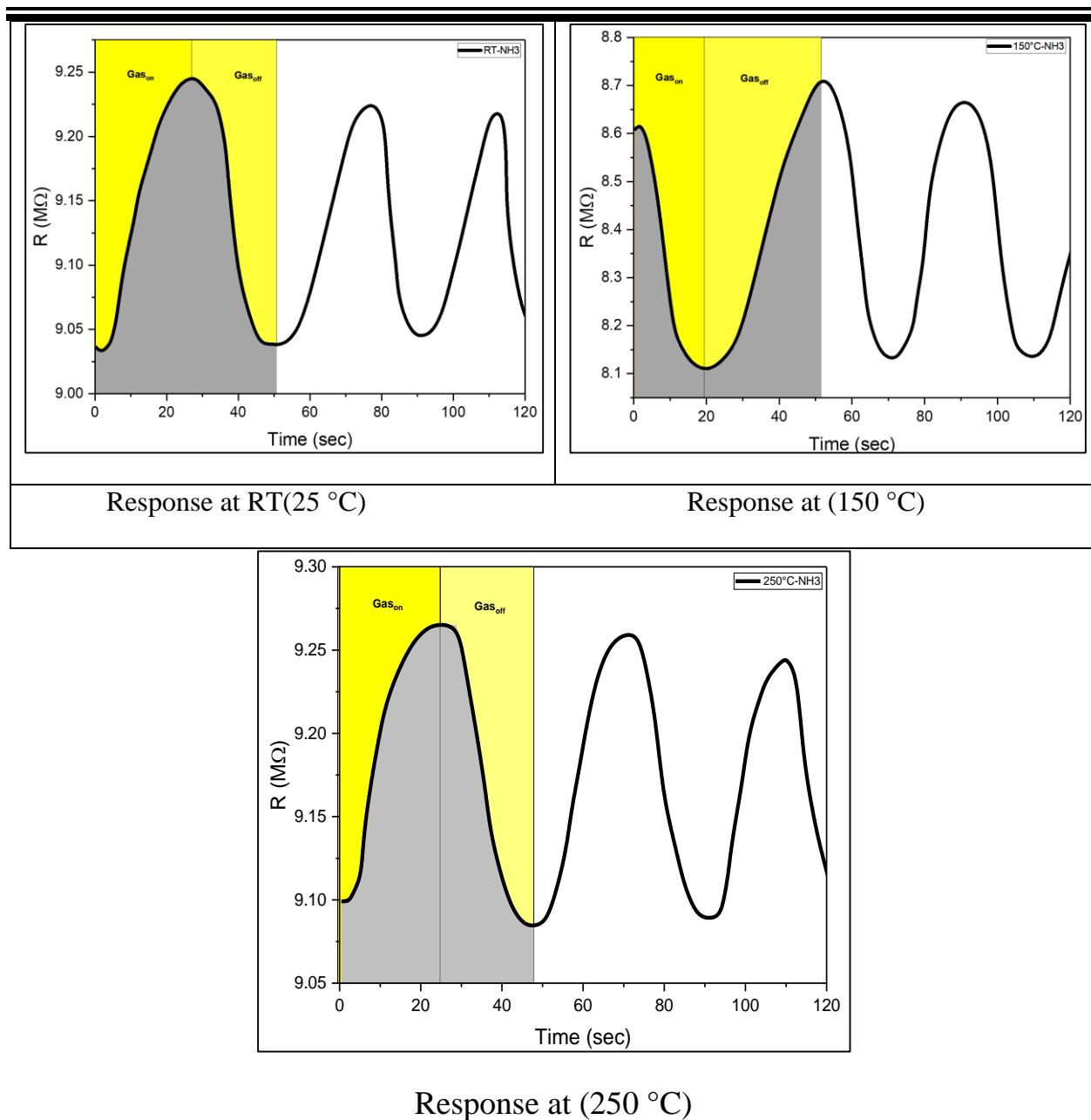


Figure (4-17). Resistance changes versus time of PVP-PPY/GO@ITO sensor upon exposure to NH₃ gas at various operating temperatures RT, 150 and 250 °C.

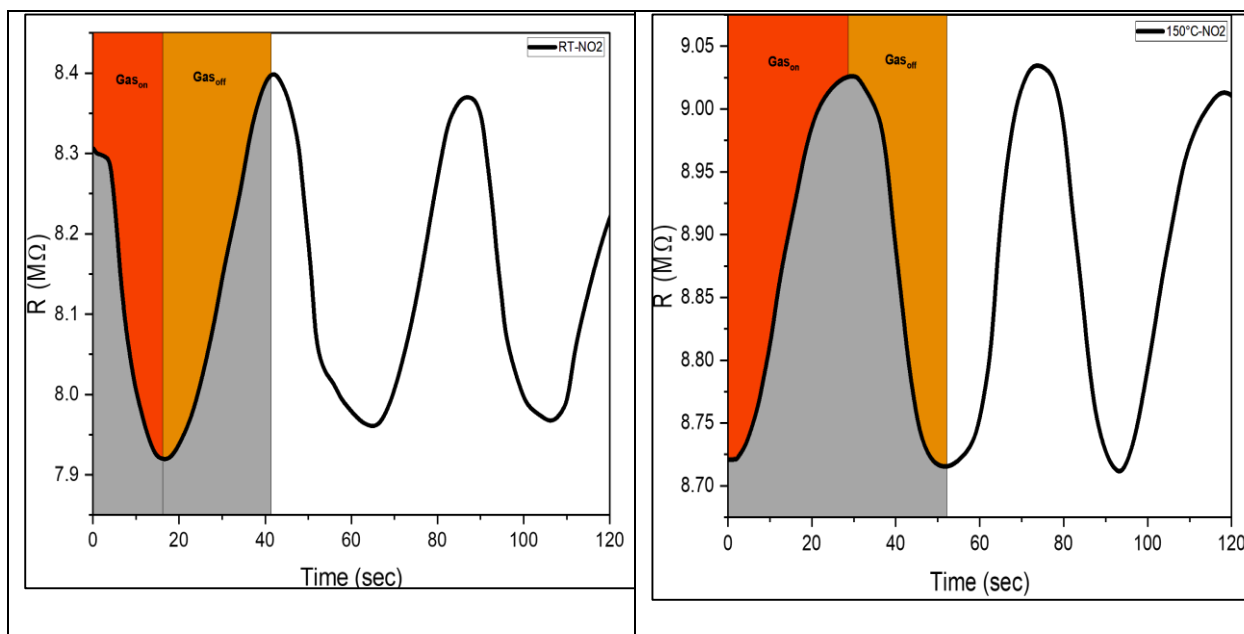
The nanocomposite revealed a behavior as a P-type semiconductor, where the conductive polypyrrole polymer in this nanocomposite also behaves as a P-type semiconductor due to the conjugated structure of the polymer, where the movement of positive charge carriers (holes) results in the formation of its conductivity. When

PPY is exposed to reduced ammonia gas, the doping process occurs, which results in a reduction in the hole concentration and improved electrical resistance [24]. GO contains abundant functional groups, gives a large surface area and thus provides many active sites for gas adsorption. In addition, the electrical noise is lower. Charge fluctuations are easily prevented due to the high-quality graphene network and its properties [189], as well as the conductive and transparent indium tin oxide. That is used to increase the efficiency of the sensing layer through the adsorption or desorption processes of O_2 molecules on the nanocomposite surface film [30].

At RT, the sensor shows the highest resistance value because the reducing gas NH_3 acts to reduce electrons to the conducting polymer PPY by the development effect. This reduces the presence of holes because the sensor behaves as a P-type semiconductor. When the operating temperature rises to $250\text{ }^{\circ}\text{C}$, NH_3 molecules are released very quickly from the surface of the nanocomposite, where the desorbing effect of the PPY polymer decreases, which restores a large part of the original conductivity of the polymer and significantly reduces the electrical resistance [192].

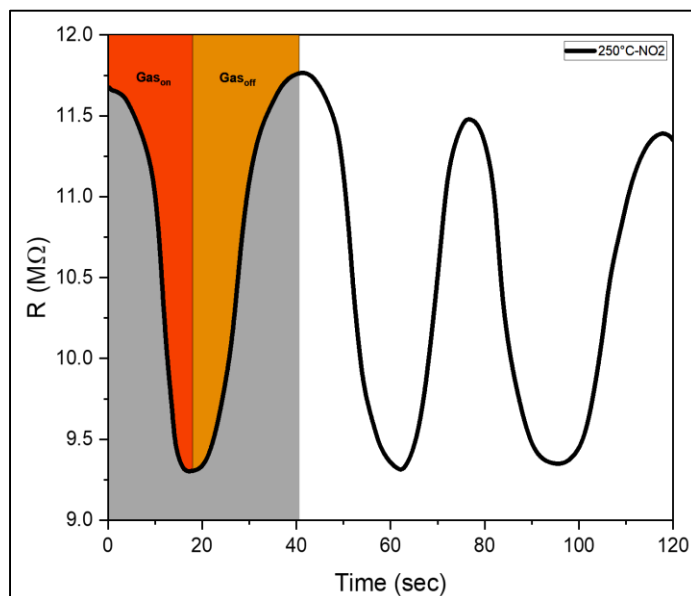
Figure (4-18) illustrates the outcome of the electrical resistance behavior of the oxidized NO_2 gas sensor at a constant concentration of about 150 ppm and different temperatures (25, 150, $250\text{ }^{\circ}\text{C}$) for the PVP-PPY/GO@ITO nanocomposite membrane exhibiting P-type semiconductor behavior. The results showed negative electrical resistance that related to the gas operation time. The resistance increases steadily when the gas is turned off because the oxidized NO_2 gas, when exposed to the P-type semiconductor sensor, works to withdraw the electrons on the sensor surface. Increasing the concentration of holes (positive charge carriers) increased the electrical conductivity. When the gas was turned on, the electrical resistance decreased, and the maximum electrical resistance appeared at $25\text{ }^{\circ}\text{C}$. When the temperature increased, the electrical resistance decreased due to the increasing

movement of charge carriers. These results are consistent with studies that reveal that exposure of the thin polypyrrole membrane to NO_2 gas causes a decrease in resistance [193]. In contrast, graphene sensors exposed to the same oxidizing gas exhibit low resistance at high temperatures, supporting p-type semiconductor behavior. In short, interaction with NO_2 gas increases the number of holes, resulting in a decrease in electrical resistance [194].



Response at RT(25 °C)

Response at (150 °C)



Response at (250 °C)

Figure (4-18). Resistance changes versus time of PVP-PPY/GO@ITO sensor upon exposure to NO₂ gas at various operating temperatures RT, 150 and 250 °C.

Figure (4-19) represents the sensitivity of the PVP-PPY/GO@ITO nanocomposite film towards the reduced NH₃ gas and the oxidized NO₂ gas at a 150 ppm concentration and various temperatures. Table (4-3) shows the details of the sensitivity and different operating temperatures as well as the response time that represents the time taken by the sensor cell to reach a certain percentage of change in the signal at the target gas. In addition to the recovery time, it represents the time the sensor cell takes to return to its original state after removing the gas. The presence of two nanomaterials in the nanocomposite film increased the sensitivity due to the decrease in the size of the particles, thus increasing the carrier that increases the absorption of O₂ and NO₂ gas [195]. 25% was the best sensitivity obtained at a temperature of 250 °C due to increased absorption of the gas molecules onto the nanocomposite surface (chemical adsorption) and electronic exchange. Thus, the response time decreases to 13.05 sec and the recovery time to 21.69 sec.

Followed by sensitivity at 150 °C, which reached 3.67%, and a response time of 23.4 sec. The increase in response time is attributed to chemical reactions that require energy to reach equilibrium, with a recovery time of 20.7 seconds. The lowest sensitivity was recorded at 25 sec, and the response time was 11.07 sec. The recovery time was relatively long, 23.31 sec, due to the adsorbed molecules' slowness in leaving the sensing cell's surface. The low sensitivity values at 150 °C and 25 °C are due to weak adsorption that does not significantly affect electrical conductivity. The maximum sensitivity to NH₃ gas at 150 °C reached 5.81% due to the excellent

interaction between the surface of the nanocomposite film and the gas surface, as ammonia gas works to reduce electrons through strong interaction with PPY, and GO the response time is 15.93 sec. The recovery time is equal to 27.72 sec. When the temperature rises to 250 °C, the sensitivity decreases to 1.73%, which is the least sensitive among the temperatures due to the rapid evaporation of the reducing gas, as the adsorption does not occur effectively because it needs a longer time to react on the nano-surface. The response time of 20.07 sec is higher for the same reason. The recovery time of 19.71 sec is less due to the thermal reaction that quickly removes NH_3 gas molecules from the surface [192].

The increase in the long recovery time is attributed to the ability of NO_2 gas to adhere to the surface of the nanomaterials used in the sensors because the chemical reactions (electron reduction or oxidation) are strong, as the sensor takes a longer time to release the adsorbed molecules and return the film surface to its original state. In addition to the high porosity of PPY, GO may retain gas molecules for a longer period. Thermal stimulation at high temperatures reduces the recovery time by removing the adsorbed molecules and returning the surface to its original state [196].

The contact mechanism between the polymer film and NH_3 gas increases and decreases as the pure PPY polymer sample's response time increases. At the same time, the response time decreases and then increases for the impregnated PPY polymer samples (nanocomposite). The opposite is true for the recovery time, as it decreases and then increases for the PPY polymer sample, while for the nanocomposite film sample, the recovery time increases and then decreases in agreement with the literature [197]. Other factors contribute, such as the ability of the reducing gas to adsorb on the sensor surface and the high polarity of NH_3 gas, which makes it interact strongly with the active material of the PVP-PPY/GO@ITO

film (such as hydrogen bonds or chemical interactions) that make it retain ammonia gas molecules for a longer period compared to NO_2 gas. Moreover, the nanoporous ITO presented the good ability for sensor and other factors that make the recovery time longer [198].

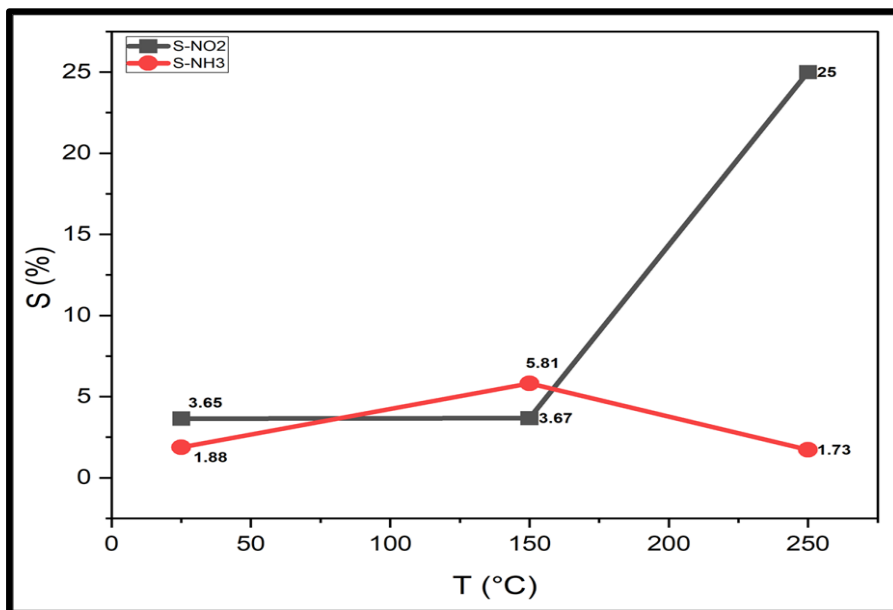


Figure (4-19). The sensitivity versus the various operating temperatures 25, 150 °C, and 250 °C.

Table (4-3). Sensitivity, response time and recovery of the S4 nanocomposite sensor cell at three temperatures based on exposure to NO₂ and NH₃ gases.

T °C	NO ₂			NH ₃		
	Sensitivity %	Response Time(sec)	Recovery Time (sec)	S %	Response Time(sec)	Recovery Time(sec)
25	3.65	11.07	23.31	1.88	15.75	27.72
150	3.67	23.4	20.7	5.81	15.93	27.72
250	25	13.05	21.69	1.73	20.07	19.71

Hybrid nanostructures composed of polypyrrole (PPY), graphene oxide (GO), and indium tin oxide (ITO) play a complementary role in enhancing the gas adsorption efficiency of nano sensors. Polypyrrole (PPY) is a conductive p-type polymer with a π -conjugated electronic network that enables efficient charge transport. When exposed to gases such as ammonia (NH₃), it interacts with them, reducing the number of holes in its structure. This is reflected in a change in electrical resistance, enabling accurate gas detection [199]. On the other hand, graphene oxide (GO) offers a high surface area due to its papery nature and microporous structure [200]. It also contains active functional groups such as –OH and –COOH, which act as effective sites for gas adsorption through hydrogen bonding and electrostatic interactions, increasing the amount of adsorbed molecules and improving sensor performance [201]. Indium tin oxide (ITO) is a transparent, n-type conductive material that enhances the chemical absorption of gases through redox reactions. Its porous nanostructure provides channels that allow gas molecules

to easily pass into the material, enhancing reaction efficiency and response speed [202]. When these materials are combined, a synergistic effect occurs: GO captures gas molecules, PPY converts this reaction into an electrical charge, and ITO accelerates and catalyzes the overall reaction, resulting in a significant improvement in the sensor's sensitivity and response to gases. Table 5 revealed a comparison of the results of this study and literatures.

Table (4-4) presented a comparison of the results between literatures used the similar nanomaterials and nanocomposites used the same materials in this study.

Sensor material	Operating temperature (°C)	Target gas/vapor	Conc. (ppm)	Sensor Sensitivity (%)	Response time (sec)	Recovery time (sec)	Ref.
PVP/CuO	RT	NH ₃	10	23.8%	17	15	[203]
PEO–CMC–PANI/GO@Si₃N₄	100 200	NO ₂	500	6.86	16	19	[29]
PPY	RT	NH ₃	50	77.75%	12	52	[204]
ITO	350	NH ₃ NO ₂	1000 100	2.39 2.14	28 42	140 200	[205]
PPY/MoS₂	150	NO ₂	100	49.8%	120	57	[206]
PVP+PPY/GO-ITO	150 250	NO ₂	150	3.67 25	23.4 13.05	20.7 21.69	The present study
PVP+PPY/GO-ITO	150 250	NH ₃	150	5.81 1.73	15.93 20.07	27.72 19.71	The present study

4.5.2 Antibacterial activity

The agar diffusion test results of samples S1, S2, S3, and S4 in Figure (4-20) proved their success in killing bacteria (Gram-negative *Escherichia coli*) and (Gram-positive *Staphylococcus aureus*). In control samples (S1, pure PVP k30), both bacteria exhibit normal morphology, S1 showed the different inhibition zone of bacteria with a diameter of 6 and 13 mm, respectively, confirming PVP's inherent biocompatibility. The increased after contribution of PPY polymer to 15 and 14 mm, respectively, suggesting PPY-induced stress. S3 (PVP-PPY/GO): GO's sharp edges cause severe mechanical damage that improved up to 17 and 16 mm of inhibition cells, respectively. Interestingly, S4 (PVP-PPY/GO@ITO) boosted the inhibition zone up to 19 and 20 mm, respectively. GO's nanosheet edges puncture membranes (more effective against *E. coli* due to thinner LPS layer) [27].

ITO's photocatalytic activity generates ROS, overwhelming bacterial antioxidant defenses (particularly lethal to *S. aureus* lacking catalase). PPY's positive charge (protonated N⁺) disrupts negatively charged bacterial walls. These significant improvements are related to the contribution of GO-ITO, which is abundant with functional groups assisting in the generation of ROS (e.g., •OH, H₂O₂) under ambient light [177].

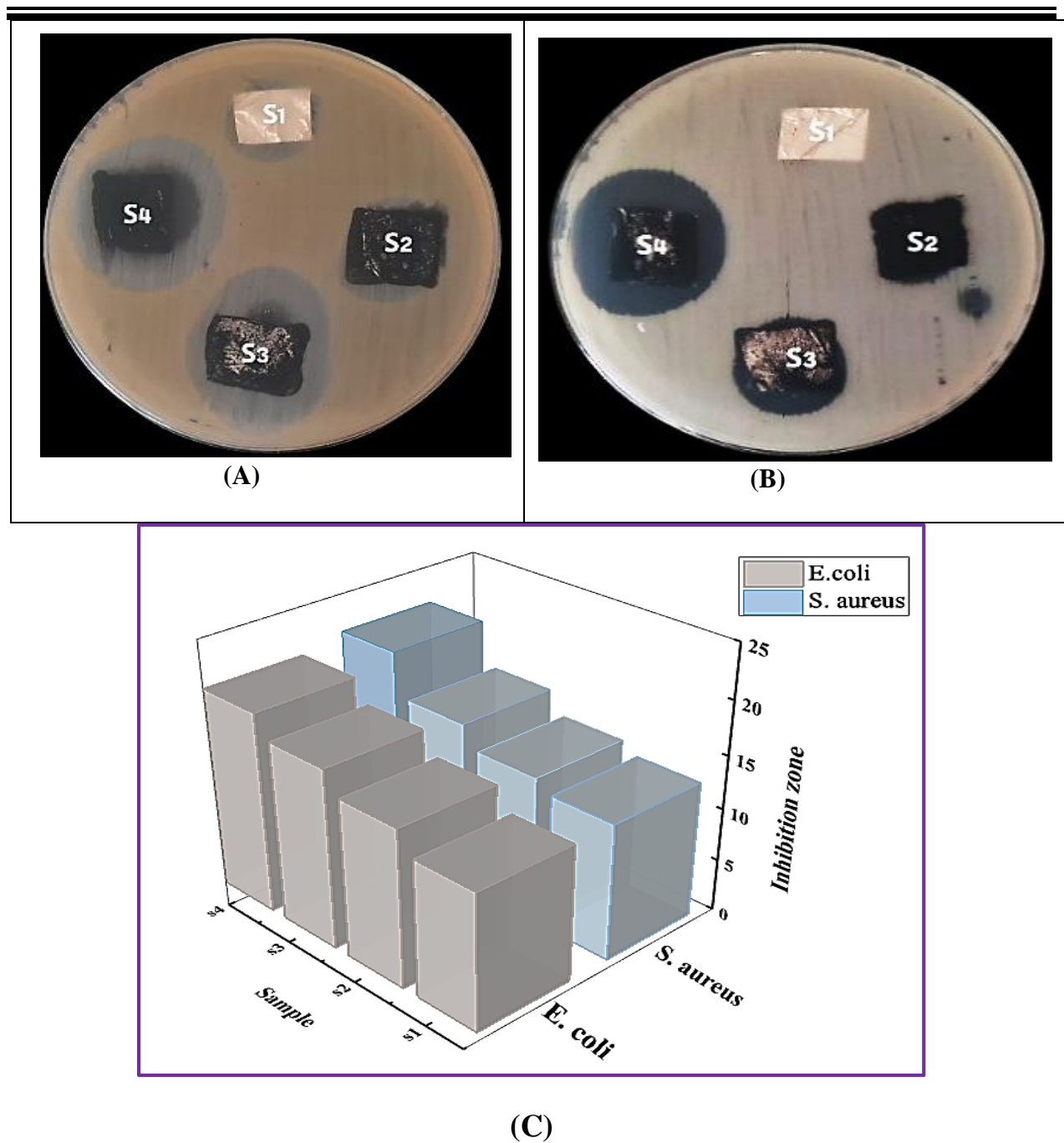


Figure (4-20). Images of the inhibition zones of (A) *E. coli* and (B) *S. aureus*, and (C) comparison diagram of results for samples.

The absorption spectrum revealed the complex ability to strongly absorb light in the visible range (400-460 nm) in sample S4. This absorption enhances the generation of electron-hole (e^-/h^+) pairs, which react with oxygen and water to produce reactive oxygen species (ROS), such as hydroxyl radicals, superoxide anions, and hydrogen peroxide. These oxides destroy the bacterial cell wall through protein oxidation and DNA damage, leading to bacterial death. Thus, it was shown that the main mechanism used to inhibit bacteria by PVP–PPY/GO–ITO nanocomposite is photocatalysis, i.e., through light absorption and generation of reactive oxygen species (ROS). These results are consistent with the results of researchers [208].

FTIR results support the synergistic effect between light absorption, which generates bacteriostatic reactive oxygen species and surface chemical reactivity of functional groups (N-H, O-H, C=C, C=O), which correspond to the peaks 3385 cm^{-1} , and 1672 cm^{-1} that destroy the bacterial cell wall and thus disrupt its vital functions, leading to bacterial killing or inhibition [31]. The mechanism of bacterial inhibition by PVP–PPY/GO–ITO nanocomposite via light-induced ROS generation is shown in Figure (4-21).

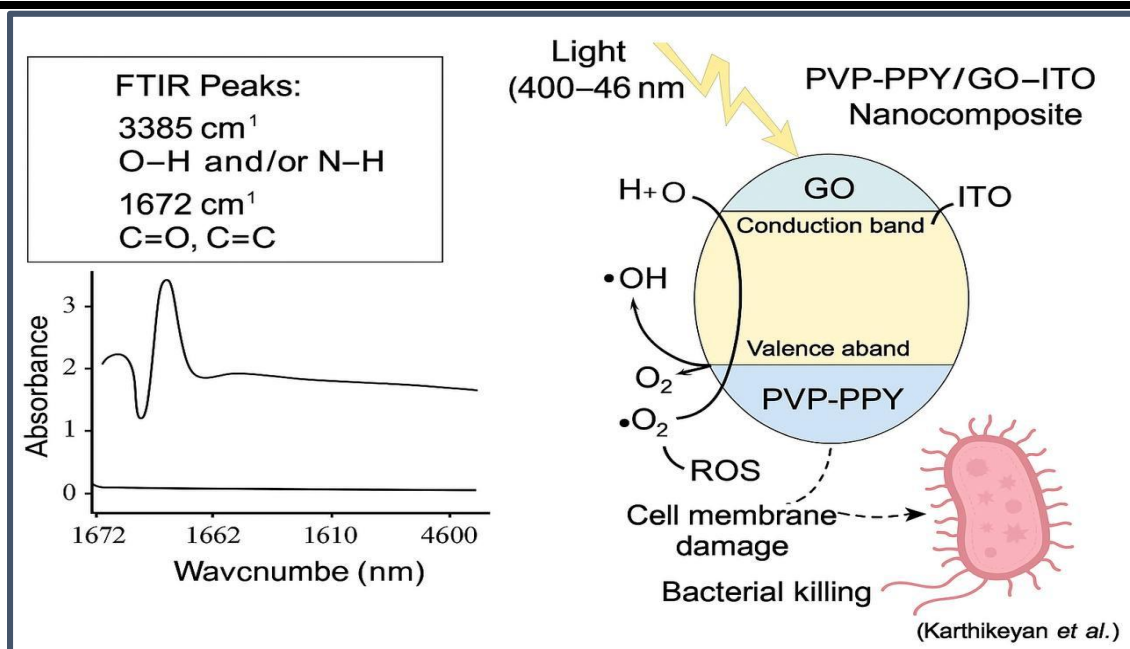


Figure (4-21). Mechanism of bacterial inhibition by PVP-PPY/GO-ITO nanocomposite via light-induced ROS generation (According to UV-Vis and FTIR peaks).

4.5.3 Urea biosensor

4.5.3.1 Cyclic voltammetry properties (CV)

Cyclic voltammetry (CV) is one of the most widely used electrochemical analysis techniques for studying electrochemical reactions and evaluating the performance of electrodes and active materials. This technique relies on applying a linearly varying voltage over a specific range to the working electrode and then reversing it while recording the current generated by redox reactions. This allows for analyzing electron transport mechanisms, diffusion behavior, and surface interactions [21].

This technique was used to study the electrochemical behavior of a PVP+PPY/GO-ITO its efficiency in the non-enzymatic detection of urea. The investigation was conducted in a three-electrode electrochemical system comprising a carbon working electrode, an Ag/AgCl reference electrode, and a carbon auxiliary electrode. A cyclic sweep voltage was applied over a range of -1.0 to +1.0 V while the current generated by the redox reactions was recorded.

Figure (4-22) shows the curves recorded before adding the biocomposite, with relatively low currents. This indicates only the basic behavior of the nanomaterials, without any apparent electrochemical reaction. To accurately analyze the electrochemical performance, the peak current and voltage values were determined before adding urea. The oxidation peak current (I_{pa}), oxidation peak potential (E_{pa}), reduction peak current (I_{pc}), and reduction peak potential (E_{pc}) values were recorded [210] are recorded in Table (4-5). These values demonstrated weak redox peaks attributed to the nanocomposite responses, reflecting the intrinsic electrochemical performance of the modified surface in the absence of the biocomposite. The results showed that increasing the nanocomposite concentration from 5 mg/L to 15 mg/L showed a significant increase in peak currents (I_{pa} and I_{pc}), indicating increased surface electrochemical efficiency and a better response to electron flow. The 15 mg/L concentration, in particular, showed the highest oxidation current (+0.037 mA) and reduction current (-0.060 mA), indicating that it is the optimal choice for further urea response analysis [211] .

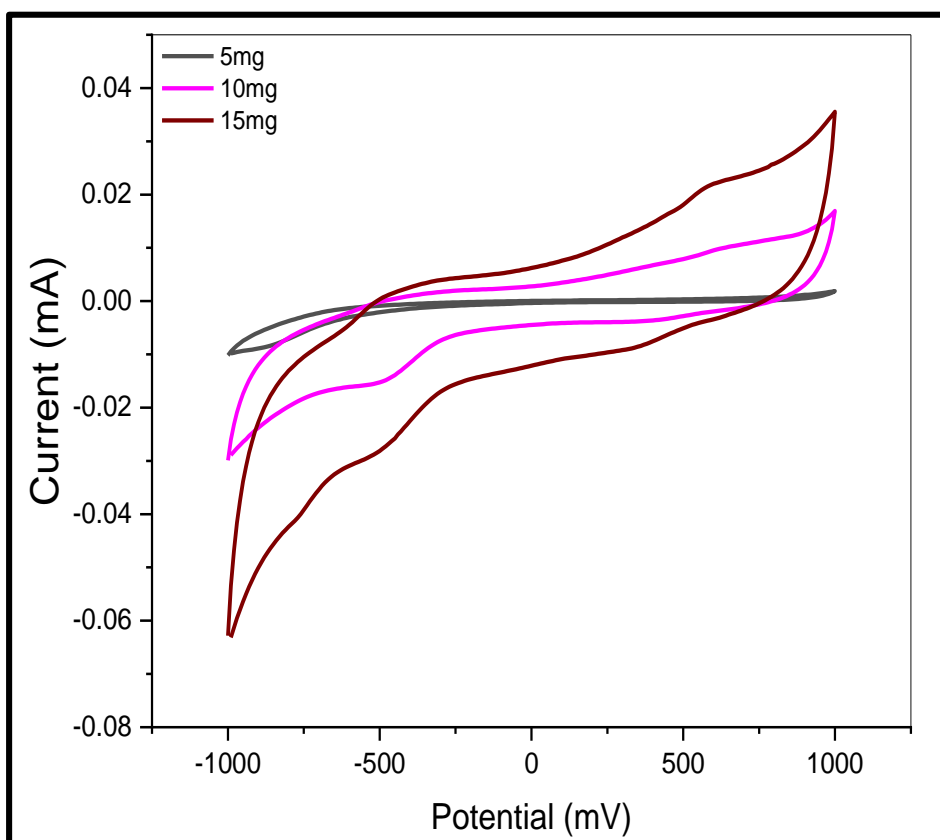


Figure (4-22). Cyclic voltammetry analysis of electrode modified with different ratios of PVP-PPY/GO-ITO nanocomposite before adding urea.

Table (4-5): Peak values of current and voltage for the electrode modified with PVP-PPY/GO-ITO nanocomposite concentrations before adding urea.

Samples	I _{pa} (mA)	E _{pa} (mV)	I _{pc} (mA)	E _{pc} (mV)
5 mg/L	+0.0017	+990	-0.01	-1000
10 mg/L	+0.016	+990	-0.029	-990
15 mg/L	+0.034	+990	-0.06	-990

Figure (4-23) illustrates the addition of a 0.1 M urea solution to the samples. A significant increase in the oxidation currents (I_{pa}) and areduction in the currents (I_{pc}) were observed, with sharper peaks appearing, indicating a direct interaction between the urea molecules and the modified electrode surface, as shown in Table (4-5). This improved response is attributed to the role of the conductive polymer, with PPY enhancing electron transfer, while PVP contributes to improved distribution and stability of the nanostructure. GO is the most effective conductor due to its large surface area and active functional groups (carboxyl and hydroxyl), which facilitate the urea reaction and accelerate charge transfer. Indium tin oxide nanoparticles are a key component in the sensor's performance, acting as a conductive working electrode that provides a solid base for the deposition of the PVP–PPY/GO composite. The high conductivity, chemical stability, and smooth surface properties of ITO contribute to ensuring the stability of the sensing layer and enhancing electron transfer efficiency during electrochemical tests. The interaction of ITO with other active nanocomposite materials also contributes to the non-enzymatic sensing mechanism, which is reflected in the high currents and pronounced peaks observed after the addition of urea [212].

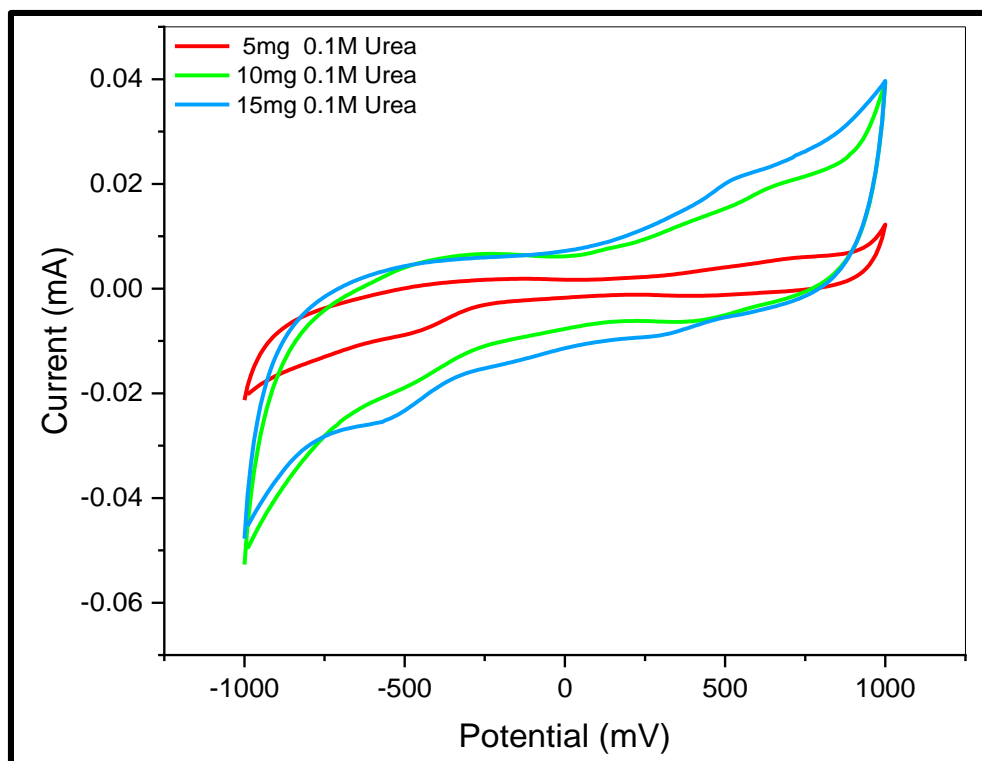


Figure (4-23). Cyclic voltammetry analysis of an electrode modified with different concentrations of PVP-PPY/GO-ITO nanocomposites after adding a 0.1 M concentration of urea.

Table (4-6): Peak current and voltage values for an electrode modified with different concentrations of PVP-PPY/GO-ITO nanocomposites after adding a 0.1 M concentration of urea.

Samples	I _{pa} (mA)	E _{pa} (mV)	I _{pc} (mA)	E _{pc} (mV)
5 mg/L	+0.012	+1000	-0.02	-990
10 mg/L	+0.037	+970	-0.052	-1000
15 mg/L	+0.039	+1000	-0.047	-1000

4.5.3.2 Electrochemical impedance spectroscopy (EIS)

The total impedance of a system is determined by several factors within the electrochemical cell, including the solution resistance, diffusion phenomena, passivation layers, and electron transfer kinetics. The contributions of these factors vary with frequency; at low frequencies, diffusion processes dominate, while at high frequencies, electron transfer kinetics becomes dominant. EIS results are typically presented in two forms: either using a Nyquist plot, where the real part of the impedance (Z_1) is represented on the horizontal axis and the imaginary part ($-Z_2$) on the vertical axis, or using Bode plots to display the total impedance and phase angle versus frequency [48]. Using the Nyquist plot, the total impedance of the system can be derived by analyzing the apparent arc radius, which reflects the charge transfer resistance. In this study, the total impedance was calculated based on the distance between the starting point (at high frequency) and the arc intersection point with the horizontal axis (at low frequency), which represents the sum of the solution resistance and the polymer layer resistance. This analysis helps evaluate the effect of adding materials such as urea on the conductivity and charge transfer efficiency in the system. Therefore, EIS is a sensitive and useful tool for understanding the electrochemical performance of the material [48].

An electrical impedance spectroscopy (EIS) test Figure (4-24) was performed to analyze the performance of PVP+PPY/GO-ITO composite-modified electrodes at different concentrations (5, 10, and 15 mg/L) before and after the addition of a 0.1 M urea solution. The Nyquist plots showed a clear variation in charge transport behavior depending on the nanomaterial concentration [213]. In the 5 mg/L sample, the resistance increased after the addition of urea (Z_1 from 37,630 to 35,810 Ω and

Z_2 from 49,050 to 68,050 Ω), indicating a weak response and limited reactivity, resulting from the lack of active reaction sites. In contrast, the 10 mg sample showed an excellent response; Z_1 decreased from 37,630 to 8,036 Ω and Z_2 from 49,050 to 16,550 Ω after the reaction, indicating a significant improvement in conductivity and electron transfer due to the effective interaction with urea . The sample with the highest concentration (15 mg/L) showed the best electrochemical performance, with Z_1 decreasing from 12,550 to 4,066 Ω and Z_2 from 23,100 to 9,123 Ω after the addition of urea. This jump represents a very effective sensor response and confirms that this concentration provided a good balance between electrical conductivity and the number of active sites, facilitating the urea reaction at the electrode surface and significantly reducing electrochemical resistance. This improved electrode conductivity and electron transfer. This is a direct result of the presence of sufficient nanomaterial to cover the surface and provide numerous active sites [214].

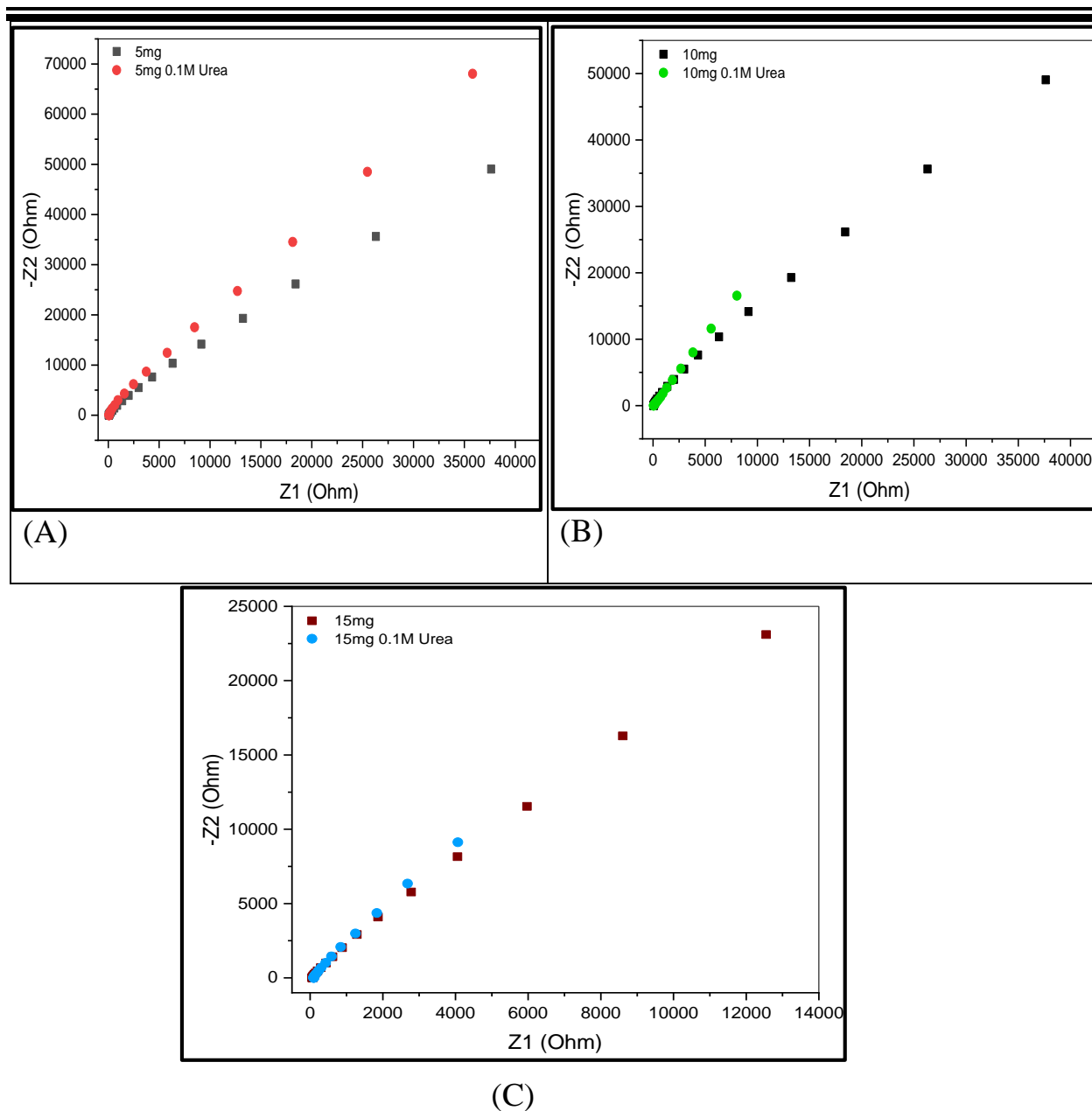


Figure (4-24): Nyquist plots of electrochemical isotherm (EIS) analysis of PVP-PPY/GO composite on ITO substrate with different masses A. 5 mg/L, B. 10 mg/L, C. 15 mg/L showing the change in the isotherm response before and after adding urea at a concentration of 0.1 M.

Based on the CV and EIS results, this sensor can be considered efficient, stable, and fast-responding, and is a promising candidate for real-world applications in the medical or environmental field to accurately monitor urea concentrations without the need to use complex or expensive enzymes.

Chapter Five

Conclusions and Future Works

5.1 Conclusion

1. This study successfully combined hybrid materials to manufacture new NCs with two nanomaterials, exhibiting significant and distinct properties compared to the original PVP polymer using the solution casting method.
2. FTIR analysis revealed favorable physical interactions between the blended polymer components and the nanomaterials.
3. XRD analysis results for (S1-S4) showed an increase in the order of the crystalline structure. The introduction of GO, PPY, and ITO materials caused a change in the interlayer spacing and an increase in structural organization.
4. FE-SEM images showed a homogeneous surface and excellent dispersion of the nanomaterials within the polymer matrix.
5. Improved optical properties, with the optical absorbance increasing from 0.06 to 0.85 after the addition of the nanoparticles at 290nm. The optical band gap decreased from 3.43 to 1.63 eV for the allowed indirect transitions, and from 3.21 to 0.62 eV for the unallowed transitions.
6. The alternating current electrical properties of PVP were significantly enhanced after the addition of PPY, GO, and ITO, with the dielectric constant improving from 154 to 300, and the AC conductivity increasing from 1.31×10^{-11} to 4.64×10^{-11} S. cm⁻¹.
7. The sensitivity of samples to reducing ammonia (NH₃) and oxidizing nitrogen dioxide (NO₂) was tested at different temperatures. The maximum sensitivity to NO₂ gas was 25% at 250°C, while NH₃ recorded a sensitivity of 5.81% at 150°C.
9. Antibacterial test results showed significant improvement after incorporating

two nanomaterials into the S4 sample, from 13 mm to 19 mm for *Escherichia coli* and from 6 to 20 mm for *Staphylococcus aureus*.

8. Electrochemical test results, including cyclic voltammetry (CV) and electrochemical impedance spectroscopy (EIS), indicate that the PVP + PPY / GO-ITO composite-modified sensor at a concentration of 15 mg/L exhibits exceptional performance in the non-enzymatic detection of urea.

9. The CV results for the I_{pa} current improved from +0.034 mA to +0.039 mA after adding 0.1 M urea. The I_{pc} current also improved from −0.047 mA to −0.06 mA for the same reason.

10. EIS (electrical impedance) results showed a significant decrease from 12,550 Ω to 4,066 Ω for the real Z₁ part and from 23,100 Ω to 9,123 Ω for the imaginary Z₂ part after adding 0.1 M urea. This demonstrates a significant improvement in electron transfer.

11. These NCs offer promising biological, electrical, and sensing activity, demonstrating that nanotechnology holds great promise for medical and sensing applications.

5.2 Future Works

1. Study other properties, including the mechanical, rheological, and thermal aspects of these nanocells.
2. Study the effect of different nanomaterials, such as hybrid mixtures containing GOr or SiO₂ instead of GO or ITO, to develop new nanocells for studying optical properties.
3. Study the effect of an additional biodegradable polymer on hybrid nanocells.
4. Study how various environmental factors, including humidity, temperature, and gas time, affect the fabrication of thermal sensors in fields such as biology, chemistry, and gas detection.
5. Study the sensitivity of hybrid nanocells to changes in biological substance concentrations by adding coenzymes.
6. Explore the potential of PVP + PPY /GO@ITO nanocomposite for glucose and cholesterol sensing.

References

References

- [1] A.-K.J. Rashid, E.D. Jawad, B.Y. Kadem, A Study of Some Mechanical Properties of Iraqi Palm Fiber-PVA Composite by Ultrasonic, *Eur. J. Sci. Res.* 61 (2011) 203–209.
- [2] K. Namsheer, C.S. Rout, Conducting polymers: a comprehensive review on recent advances in synthesis, properties and applications, *RSC Adv.* 11 (2021) 5659–5697.
- [3] T. Nezakati, A. Seifalian, A. Tan, A.M. Seifalian, Conductive polymers: opportunities and challenges in biomedical applications, *Chem. Rev.* 118 (2018) 6766–6843.
- [4] A.J. Heeger, Semiconducting and metallic polymers: the fourth generation of polymeric materials, *J. Phys. Chem. B* 105 (2001) 8475–8491.
- [5] H. Bai, G. Shi, Gas sensors based on conducting polymers, *Sensors* 7 (2007) 267–307.
- [6] W. Y. C., Y.H. Wong, B. Ang, A.A. Baharuddin, A.S.M.A. Haseeb, Effects of polymerization oxidants on the fabrication of electrospun PPy/WO₃ composites, *J. Mater. Sci. Mater. Electron.* 34 (2023). <https://doi.org/10.1007/s10854-022-09483-0>.
- [7] R.A. Ghazi, K.H. Al-Mayalee, E. Al-Bermany, F.S. Hashim, A.K.J. Albermany, Impact of polymer molecular weights and graphene nanosheets on fabricated PVA-PEG/GO nanocomposites: Morphology, sorption behavior and shielding application., *AIMS Mater. Sci.* 9 (2022).
- [8] A.M. Aboraia, I.S. Yahia, M. Saad, G. Alsulaim, K.M. Alnahdi, S.A. Alsharif, N.N. Elewa, Y.A.M. Ismail, M. Mostafa khalefa, N. Madkhali, Exploration of the structural rGO thin films and their optical characteristics for optoelectronic device applications, *J. Opt.* (2024) 1–10.
- [9] E. Al-Bermany, B. Chen, Effect of the Functional Groups of Polymers on Their Adsorption Behavior on Graphene Oxide Nanosheets, *Macromol. Chem. Phys.* 224 (2023) 2300101. <https://doi.org/10.1002/macp.202300101>.
- [10] M. Fu, Z. Liu, Y. Duan, F. Zhou, Y. Li, Graphene-based terahertz tunable double-broadband perfect absorber, *Opt. Commun.* 563 (2024) 130534.

References

- <https://doi.org/https://doi.org/10.1016/j.optcom.2024.130534>.
- [11] C. Su, K.P. Loh, Carbocatalysts: graphene oxide and its derivatives, *Acc. Chem. Res.* 46 (2013) 2275–2285.
- [12] H. Kim, a C.M. Gilmore, A. Pique, J.S. Horwitz, H. Mattoussi, H. Murata, Z.H. Kafafi, D.B. Chrisey, Electrical, optical, and structural properties of indium–tin–oxide thin films for organic light-emitting devices, *J. Appl. Phys.* 86 (1999) 6451–6461.
- [13] S.A. Jasim, H.A.J. Banimuslem, F.H. Alsultany, E. Al-Bermany, R.M. Mohammed, Ammonia and nitrogen dioxide detection using ZnO/CNT nanocomposite synthesized by sol–gel technique, *J. Sol-Gel Sci. Technol.* 108 (2023) 734–741.
- [14] L. Torsi, A. Dodabalapur, L. Sabbatini, P.G. Zambonin, Multi-parameter gas sensors based on organic thin-film-transistors, *Sensors Actuators B Chem.* 67 (2000) 312–316.
- [15] S.T. Shishiyanu, T.S. Shishiyanu, O.I. Lupan, Sensing characteristics of tin-doped ZnO thin films as NO₂ gas sensor, *Sensors Actuators B Chem.* 107 (2005) 379–386.
- [16] A. Zamora-Gálvez, E. Morales-Narváez, C.C. Mayorga-Martinez, A. Merkoçi, Nanomaterials connected to antibodies and molecularly imprinted polymers as bio/receptors for bio/sensor applications, *Appl. Mater. Today* 9 (2017) 387–401.
- [17] Cerium oxide nanoparticles: properties, biosynthesis and biomedical application, *RSC Adv.* 10 (2020) 27194–27214.
- [18] C.S. Pundir, S. Jakhar, V. Narwal, Determination of urea with special emphasis on biosensors: A review, *Biosens. Bioelectron.* 123 (2019) 36–50.
- [19] T.M. Uddin, A.J. Chakraborty, A. Khusro, B.M.R.M. Zidan, S. Mitra, T. Bin Emran, K. Dhama, M.K.H. Ripon, M. Gajdács, M.U.K. Sahibzada, Antibiotic resistance in microbes: History, mechanisms, therapeutic strategies and future prospects, *J. Infect. Public Health* 14 (2021) 1750–1766.
- [20] A. Salmanipour, M.A. Karimi, A. Mohadesi, M.A. Taher, S. Shafiei, A Review on Fundamentals and Progress in Urea Biosensors, *Iran. J. Anal. Chem.* 3

References

- (2016) 1–26.
- [21] H. Mudila, P. Prasher, S. Rana, B. Khati, M.G.H. Zaidi, Electrochemical oxidation-reduction and determination of urea at enzyme free PPY-GO electrode, *Carbon Lett.* 26 (2018) 88–94.
- [22] F.L. Rashid, A. Hadi, N.H. Al-Garah, A. Hashim, Novel Phase Change Materials, MgO Nanoparticles, and Water Based Nanofluids for Thermal Energy Storage and Biomedical Applications, *Int. J. Pharm. Phytopharm. Res.* 8 (2018) 46–56.
- [23] A.M. El Nahrawy, A.B.A. Hammad, A.M. Youssef, A.M. Mansour, A.M. Othman, Thermal, dielectric and antimicrobial properties of polystyrene-assisted/ITO: Cu nanocomposites, *Appl. Phys. A* 125 (2019) 1–9.
- [24] X. Zheng, X. Qiao, F. Luo, B. Wan, C. Zhang, Low-cost high-performance NO₂ sensor based on nanoporous indium tin oxide (ITO) film, *Sensors Actuators B Chem.* 346 (2021) 130440.
- [25] A.M. Alsaad, I.A. Aljarrah, A.A. Ahmad, Q.M. Al-Bataineh, A. Shariah, M.A. Al-Akhras, A.D. Telfah, The structural, optical, thermal, and electrical properties of synthesized PEO/GO thin films, *Appl. Phys. A* 128 (2022) 676.
- [26] T. Li, W. Yin, S. Gao, Y. Sun, P. Xu, S. Wu, H. Kong, G. Yang, G. Wei, The combination of two-dimensional nanomaterials with metal oxide nanoparticles for gas sensors: a review, *Nanomaterials* 12 (2022) 982.
- [27] Z. Liu, X. Liu, Z. Cui, Y. Zheng, Z. Li, Y. Liang, X. Yuan, S. Zhu, S. Wu, Surface photodynamic ion sterilization of ITO-Cu₂O/ZnO preventing touch infection, *J. Mater. Sci. Technol.* 122 (2022) 10–19.
- [28] S. Khataee, G. Dehghan, Z. Shaghaghi, A. Khataee, An enzyme-free sensor based on La-doped CoFe-layered double hydroxide decorated on reduced graphene oxide for sensitive electrochemical detection of urea, *Microchim. Acta* 191 (2024) 152.
- [29] R.A. Abdul-Nabi, E. Al-Bermany, Performers of Si₃N₄ Concentrations on Morphology and Electrical Behavior for New Quinary Fabrication PEO-CMC-PANI/GO@Si₃N₄ Nanocomposites for Electronic Devise and Gas Sensor Application, *Silicon* (2024). <https://doi.org/10.1007/s12633-024-03092-8>.

References

- [30] A. Verma, T. Kumar, R. Singhal, An innovative Ag/Cu-doped polypyrrole hybrid nanocomposite gas sensor for superior ammonia detection at room temperature, *Mater. Adv.* 6 (2025) 1869–1882.
- [31] R.A. Abdul-Nabi, E. Al-Bermany, Antibacterial and anticancer potentials of graphene-silicon nitride nanomaterials-enhanced polymer nanocomposites: advanced characterization and optical behavior insights, *J. Biosaf. Biosecurity* 7 (2025) 55–68. <https://doi.org/10.1016/j.jobbb.2025.04.001>.
- [32] S. Gungordu Er, R. Bulatshinghala, S.B. Kizilates, B. Li, R. Ryan, T.A. Tabish, I. Dharmasena, M. Edirisinghe, Multifunctional Conductive Nanofibers for Self-Powered Glucose Biosensors, *Adv. Sci.* (2023).
- [33] A.J. Kalladi, M.T. Ramesan, Green-Synthesized Zinc Oxide/Polyvinyl Alcohol/Cashew Gum/Polypyrrole Nanocomposites With Enhanced Mechanical, Thermal, and Electrical Properties for Nanoelectronics, *J. Appl. Polym. Sci.* (2025) e56686.
- [34] D. Feldman, Polymer history, *Des. Monomers Polym.* 11 (2008) 1–15.
- [35] N.S. Alghunaim, Spectroscopic analysis of PMMA/PVC blends containing CoCl₂, *Results Phys.* 5 (2015) 331–336.
- [36] S.S. Ray, M. Okamoto, Polymer/layered silicate nanocomposites: a review from preparation to processing, *Prog. Polym. Sci.* 28 (2003) 1539–1641.
- [37] D.R. Paul, L.M. Robeson, Polymer nanotechnology: nanocomposites, *Polymer (Guildf)*. 49 (2008) 3187–3204.
- [38] G. Murtaza, S.H. Bukhari, L. Ali, S.Z. Ilyas, A. Hakeem, M.N. Usmani, G. Mustafa, F. Rehman, Effect of polyvinyl alcohol on structural and dielectrical properties of polyaniline, *Dig J Nanomater Biostructures* 14 (2019).
- [39] C.E. Carraher Jr, *Carraher's polymer chemistry*, CRC press, 2017.
- [40] G.M. Patel, V. Shah, J. Bhaliya, P. Pathan, K.M. Nikita, Polymer-based nanomaterials: An introduction, in: *Smart Polym. Nanocomposites*, Elsevier, 2023: pp. 27–59.
- [41] A. Patel, M. Taufik, Advances in nanocomposite material for fused filament fabrication, *Polym. Technol. Mater.* 61 (2022) 1617–1661.

References

- [42] H.W. Starkweather Jr, G.E. Moore, J.E. Hansen, T.M. Roder, R.E. Brooks, Effect of crystallinity on the properties of nylons, *J. Polym. Sci.* 21 (1956) 189–204.
- [43] C.B. Crawford, B. Quinn, Physiochemical properties and degradation, *Microplastic Pollut.* 4 (2017) 57–100.
- [44] F. Wilson, What are the factors affecting permeability of polymers?, *XR Geomembranes Blog* (n.d.).
<https://www.xrgeomembranes.com/blog/geomembrane-chemical-compatibility-vs-permeability-part-2>.
- [45] R. Balint, N.J. Cassidy, S.H. Cartmell, Conductive polymers: Towards a smart biomaterial for tissue engineering, *Acta Biomater.* 10 (2014) 2341–2353.
- [46] J.L. Bredas, G.B. Street, Polarons, bipolarons, and solitons in conducting polymers, *Acc. Chem. Res.* 18 (1985) 309–315.
- [47] J.A.E.H. Van Haare, E.E. Havinga, J.L.J. Van Dongen, R.A.J. Janssen, J. Cornil, J. Brédas, Redox states of long oligothiophenes: two polarons on a single chain, *Chem. Eur. J.* 4 (1998) 1509–1522.
- [48] A. Hamilton, The Formation and Characterisation of a Polypyrrole Based Sensor for the Detection of Urea, (2012).
- [49] X. Zhang, Y. Su, L. Lei, S. Wu, J. Shen, Preparation of a three-dimensional modified graphene oxide via RAFT polymerization for reinforcing cement composites, *Colloids Surfaces A Physicochem. Eng. Asp.* 610 (2021) 125925.
- [50] M. Habeeb, A.-K. Al-Bermany, D. Sabeeh, Effect of Polyacrilamide on the Rheological and Electrical Properties of Polyethylene Glycol, *J. Ind. Eng. Res.* 1 (2015) 33–39.
- [51] L.M. Robeson, Polymer blends, *A Compr. Rev.* 641 (2007).
- [52] D.R. Paul, J.W. Barlow, Polymer blends, *J. Macromol. Sci. Macromol. Chem.* 18 (1980) 109–168.
- [53] K. Suppiah, P.L. Teh, S. Husseinsyah, R. Rahman, Properties and characterization of carboxymethyl cellulose/halloysite nanotube bio-nanocomposite films: Effect of sodium dodecyl sulfate, *Polym. Bull.* 76 (2019)

References

- 365–386.
- [54] E.T. Thostenson, C. Li, T.-W. Chou, Nanocomposites in context, *Compos. Sci. Technol.* 65 (2005) 491–516.
- [55] H.-D. Wu, I.-D. Wu, F.-C. Chang, The interaction behavior of polymer electrolytes composed of poly (vinyl pyrrolidone) and lithium perchlorate (LiClO₄), *Polymer (Guildf)*. 42 (2001) 555–562.
- [56] K.H.H. Al-Attayah, A. Hashim, S.F. Obaid, Fabrication of novel (carboxy methyl cellulose–polyvinylpyrrolidone–polyvinyl alcohol)/lead oxide nanoparticles: structural and optical properties for gamma rays shielding applications, *Int. J. Plast. Technol.* 23 (2019) 39–45.
- [57] S.A. Ingole, A. Kumbharkhane, Temperature dependent Broadband dielectric relaxation study of Aqueous Polyvinylpyrrolidone (PVP K-15, K-30 & K-90) using a TDR, *Phys. Chem. Liq.* 59 (2021) 806–816.
- [58] N. Ismillayli, S. Suprpto, E. Santoso, R.E. Nugraha, H. Holilah, H. Bahruji, A.A. Jalil, D. Hermanto, D. Prasetyoko, The role of pH-induced tautomerism of polyvinylpyrrolidone on the size, stability, and antioxidant and antibacterial activities of silver nanoparticles synthesized using microwave radiation, *RSC Adv.* 14 (2024) 4509–4517.
- [59] A. Yussuf, M. Al-Saleh, S. Al-Enezi, G. Abraham, Synthesis and characterization of conductive polypyrrole: the influence of the oxidants and monomer on the electrical, thermal, and morphological properties, *Int. J. Polym. Sci.* 2018 (2018) 4191747.
- [60] A. Nautiyal, M. Qiao, J.E. Cook, X. Zhang, T.-S. Huang, High performance polypyrrole coating for corrosion protection and biocidal applications, *Appl. Surf. Sci.* 427 (2018) 922–930.
- [61] D.P. Dubal, Z. Caban-Huertas, R. Holze, P. Gomez-Romero, Growth of polypyrrole nanostructures through reactive templates for energy storage applications, *Electrochim. Acta* 191 (2016) 346–354.
- [62] Y. Wang, R. Song, L. Li, R. Fu, Z. Liu, B. Li, High crystalline quality conductive polypyrrole film prepared by interface chemical oxidation polymerization method, *Appl. Sci.* 12 (2021) 58.

References

- [63] J. George, C.S. Menon, Electrical and optical properties of electron beam evaporated ITO thin films, *Surf. Coatings Technol.* 132 (2000) 45–48.
- [64] V. Laxmi, D. Tyagi, A. Parveen, L. Singh, Z. Ouyang, Silicon/graphene–ITO multiple heterojunctions and 1D PhC waveguide-based photodetection for mid-NIR IPE with high responsivity, *Opt. Commun.* 530 (2023) 129142.
- [65] J. Qu, J. Wang, H. Zhang, J. Wu, X. Ma, S. Wang, Y. Zang, Y. Huang, Y. Ma, Y. Cao, Toxicokinetics and systematic responses of differently sized indium tin oxide (ITO) particles in mice via oropharyngeal aspiration exposure, *Environ. Pollut.* 290 (2021) 117993.
- [66] O.M. Løvvik, S. Diplas, A. Romanyuk, A. Ulyashin, Initial stages of ITO/Si interface formation: In situ x-ray photoelectron spectroscopy measurements upon magnetron sputtering and atomistic modelling using density functional theory, *J. Appl. Phys.* 115 (2014).
- [67] L. Premvardhan, L.A. Peteanu, P.-C. Wang, A.G. MacDiarmid, Electronic properties of the conducting form of polyaniline from electroabsorption measurements, *Synth. Met.* 116 (2001) 157–161.
- [68] D.R. Dreyer, S. Park, C.W. Bielawski, R.S. Ruoff, The chemistry of graphene oxide, *Chem. Soc. Rev.* 39 (2010) 228–240.
- [69] S. Chuah, Z. Pan, J.G. Sanjayan, C.M. Wang, W.H. Duan, Nano reinforced cement and concrete composites and new perspective from graphene oxide, *Constr. Build. Mater.* 73 (2014) 113–124.
- [70] A.K. Al-shammari, E. Al-Bermany, Polymer functional group impact on the thermo-mechanical properties of polyacrylic acid, polyacrylic amide-poly (vinyl alcohol) nanocomposites reinforced by graphene oxide nanosheets, *J. Polym. Res.* 29 (2022) 351.
- [71] B.Z. Molino, J. Fukuda, P.J. Molino, G.G. Wallace, Redox polymers for tissue engineering, *Front. Med. Technol.* 3 (2021) 669763.
- [72] P. Watts, G. Long, M.E. Meek, Chloroform, World Health Organization, 2004.
- [73] P.R. Griffiths, Fourier transform infrared spectrometry, *Science* (80-.). 222 (1983) 297–302.

References

- [74] W.S. Lau, Infrared characterization for microelectronics, World scientific, 1999.
- [75] G.G. Wallace, P.R. Teasdale, G.M. Spinks, L.A.P. Kane-Maguire, Conductive electroactive polymers: intelligent polymer systems, CRC press, 2008.
- [76] I. Ferreira, J. Ferreira-Strixino, M.L. Castilho, C.B.L. Campos, C. Tellez, L. Raniero, Characterization of *Paracoccidioides brasiliensis* by FT-IR spectroscopy and nanotechnology, *Spectrochim. Acta Part A Mol. Biomol. Spectrosc.* 152 (2016) 397–403.
- [77] J.J. Ojeda, M. Dittrich, Fourier transform infrared spectroscopy for molecular analysis of microbial cells, *Microb. Syst. Biol. Methods Protoc.* (2012) 187–211.
- [78] A.A. Bunaciu, E.G. UdriŞtioiu, H.Y. Aboul-Enein, X-ray diffraction: instrumentation and applications, *Crit. Rev. Anal. Chem.* 45 (2015) 289–299.
- [79] W.H. Bragg, W.L. Bragg, The reflection of X-rays by crystals, *Proc. R. Soc. London. Ser. A, Contain. Pap. a Math. Phys. Character* 88 (1913) 428–438.
- [80] A.S. Ilyushin, M. V Kovalchuk, The 100th anniversary of the discovery of X-ray diffraction, (2012).
- [81] C. Kittel, D.F. Holcomb, Introduction to solid state physics, *Am. J. Phys.* 35 (1967) 547–548.
- [82] A. Monshi, M.R. Foroughi, M.R. Monshi, Modified Scherrer equation to estimate more accurately nano-crystallite size using XRD, *World J. Nano Sci. Eng.* 2 (2012) 154–160.
- [83] S.L. Erlandsen, C. Frethem, Y. Chen, Field emission scanning electron microscopy (FESEM) entering the 21st century: nanometer resolution and molecular topography of cell structure, *J. Histotechnol.* 23 (2000) 249–259.
- [84] N. Munir, M. Hanif, D.A. Dias, Z. Abideen, The role of halophytic nanoparticles towards the remediation of degraded and saline agricultural lands, *Environ. Sci. Pollut. Res.* 28 (2021) 60383–60405.
- [85] O. Stenzel, *The physics of thin film optical spectra*, Springer, 2015.
- [86] M.S. Braga, O.F. Gomes, R.F.V.V. Jaimes, E.R. Braga, W. Borysow, W.J.

References

- Salcedo, Multispectral colorimetric portable system for detecting metal ions in liquid media, in: 2019 4th Int. Symp. Instrum. Syst. Circuits Transducers, IEEE, 2019: pp. 1–6. <https://doi.org/10.1109/INSCIT.2019.8868861>.
- [87] F. Yuan, C. Ouyang, M. Yang, W. Shi, W. Ren, Y. Shen, Y. Wei, X. Deng, X. Wang, Regulating the Mechanical and Optical Properties of Polymer-based Nanocomposites by Sub-Nanowires, *Angew. Chemie Int. Ed.* 62 (2023) e202214571.
- [88] R. Badry, M.A. Hegazy, I.S. Yahia, H. Elhaes, H.Y. Zahran, M.A. Ibrahim, Effect of zinc oxide on the optical properties of polyvinyl alcohol/graphene oxide nanocomposite, *Biointerface Res. Appl. Chem* 13 (2023) 2022.
- [89] V. Oliker, The ray tracing and energy conservation equations for mirror systems with two reflecting surfaces, *Comput. Math. with Appl.* 26 (1993) 9–18.
- [90] A.N. Alias, Z.M. Zabidi, A.M.M. Ali, M.K. Harun, M.Z.A. Yahya, Optical characterization and properties of polymeric materials for optoelectronic and photonic applications, *Int. J. Appl. Sci. Technol.* 3 (2013).
- [91] J. Mistrik, S. Kasap, H.E. Ruda, C. Koughia, J. Singh, Optical Properties of Electronic Materials: Fundamentals and Characterization, in: *Nat. Commun.*, Springer US, 2017: pp. 1–1. https://doi.org/10.1007/978-3-319-48933-9_3.
- [92] J. Tauc, A. Menth, D.L. Wood, Optical and magnetic investigations of the localized states in semiconducting glasses, *Phys. Rev. Lett.* 25 (1970) 749–752. <https://doi.org/10.1103/PhysRevLett.25.749>.
- [93] A.H.A. Darwesh, P.A. Mohammed, S.M. Mamand, S.A. Hussen, S.B. Aziz, M.A. Brza, R.M. Abdullah, W.O. Karim, Investigation of structural and optical characteristics of biopolymer composites based on polyvinyl alcohol inserted with PbS nanoparticles, *Coatings* 13 (2023) 578.
- [94] V.N. Suryawanshi, A.S. Varpe, M.D. Deshpande, Band gap engineering in PbO nanostructured thin films by Mn doping, *Thin Solid Films* 645 (2018) 87–92.
- [95] K.L. Chopra, P.D. Paulson, V. Dutta, Thin-film solar cells: an overview, *Prog. Photovoltaics Res. Appl.* 12 (2004) 69–92.

References

- [96] A. Kirschning, W. Solodenko, K. Mennecke, Combining enabling techniques in organic synthesis: continuous flow processes with heterogenized catalysts, *Chem. Eur. J.* 12 (2006) 5972–5990.
- [97] N.A. Azahari, N. Othman, H. Ismail, Biodegradation studies of polyvinyl alcohol/corn starch blend films in solid and solution media, *J. Phys. Sci.* 22 (2011) 15–31.
- [98] A.J. Braihi, J.K. Ahmed, D. abbass Kadham, Preparing medical (Polyvinyl Alcohol-Iodine) as a pressure sensor and investigating its physical properties, *Int. J. Pharm. Phytopharm. Res.* 7 (2017) 34–41.
- [99] H. Fröhlich, *Theory of dielectrics: dielectric constant and dielectric loss*, (No Title) (1949).
- [100] A. Muheisin, Study of electrical conductivity for amorphous and semi crystalline polymers filled with Lithium Fluoride Additive, (2009).
- [101] Y. Tao, B. Yan, D. Fan, N. Zhang, S. Ma, L. Wang, Y. Wu, M. Wang, J. Zhao, H. Zhang, Structural changes of starch subjected to microwave heating: A review from the perspective of dielectric properties, *Trends Food Sci. Technol.* 99 (2020) 593–607.
- [102] D. Klemperer, F.E. Karasz, Electrical Properties of Polymers, *J. Elastoplast.* 4 (1972) 180–210.
- [103] A.A. Al-Muntaser, R.A. Pashameah, A. Saeed, R. Alwafi, E. Alzahrani, S.A. AlSubhi, A.Y. Yassin, Boosting the optical, structural, electrical, and dielectric properties of polystyrene using a hybrid GNP/Cu nanofiller: novel nanocomposites for energy storage applications, *J. Mater. Sci. Mater. Electron.* 34 (2023) 678.
- [104] S. Christie, E. Scorsone, K. Persaud, F. Kvasnik, Remote detection of gaseous ammonia using the near infrared transmission properties of polyaniline, *Sensors Actuators, B Chem.* 90 (2003) 163–169. [https://doi.org/10.1016/S0925-4005\(03\)00036-4](https://doi.org/10.1016/S0925-4005(03)00036-4).
- [105] A. Kimleang Khun, *Linköping Studies in Science and Technology Synthesising Metal Oxide Materials and Their Composite Nanostructures for Sensing and Optoelectronic Device*, 2015.

References

- [106] K. Al-heuseen, A.I. Aljameel, R.K. Hussein, Synthesis and characterization of Cu-Doped ZnO nanostructures for UV sensing application, *BMC Chem.* 18 (2024) 1–9. <https://doi.org/10.1186/s13065-024-01141-2>.
- [107] G.F. Fine, L.M. Cavanagh, A. Afonja, R. Binions, Metal oxide semi-conductor gas sensors in environmental monitoring, *Sensors* 10 (2010) 5469–5502. <https://doi.org/10.3390/s100605469>.
- [108] Waleed Khalid Mahmood, Effect of Silver Nanoparticles on Single Walled Carbon Nanotubes Gas Sensor Parameters, University of Baghdad College of Science, 2018.
- [109] J. Wuloh, E.S. Agorku, N.O. Boadi, Modification of metal oxide semiconductor gas sensors using conducting polymer materials, *J. Sensors* 2023 (2023) 7427986.
- [110] A.I. Liapis, D.W.T. Rippin, The simulation of binary adsorption in activated carbon columns by using estimates of diffusional resistance within the carbon particles derived from batch experiments, *Chem. Eng. Sci.*; (United Kingdom) 33 (1978).
- [111] G. Korotcenkov, B.K. Cho, Metal oxide composites in conductometric gas sensors: Achievements and challenges, *Sensors Actuators B Chem.* 244 (2017) 182–210.
- [112] D.W. Kang, S.E. Ju, D.W. Kim, M. Kang, H. Kim, C.S. Hong, Emerging porous materials and their composites for NH₃ gas removal, *Adv. Sci.* 7 (2020) 2002142.
- [113] A. Klerke, C.H. Christensen, J.K. Nørskov, T. Vegge, Ammonia for hydrogen storage: challenges and opportunities, *J. Mater. Chem.* 18 (2008) 2304–2310.
- [114] K.E. Wyer, D.B. Kelleghan, V. Blanes-Vidal, G. Schauburger, T.P. Curran, Ammonia emissions from agriculture and their contribution to fine particulate matter: A review of implications for human health, *J. Environ. Manage.* 323 (2022) 116285.
- [115] K.A. Hunter, P.S. Liss, V. Surapipith, F. Dentener, R. Duce, M. Kanakidou, N. Kubilay, N. Mahowald, G. Okin, M. Sarin, Impacts of anthropogenic SO_x, NO_x and NH₃ on acidification of coastal waters and shipping lanes, *Geophys.*

References

- Res. Lett. 38 (2011).
- [116] Q.S. KAREEM, Preparation of polymeric (polyaniline/graphene) Thin film and study its response for some organic materials as electronic applicatio, University of Basrah College of Education for Pure Sciences, 2020.
- [117] T.L.M.J. (2012), VEHICLE POLLUTION CONTROL IN EUROPE: THE LOCAL AND GLOBAL, Budid. AYAM RAS PETELUR (Gallus Sp.) 21 (1990) 99–104.
- [118] Y. Atassi, M. Tally, Electrochemical polymerization of anilinium hydrochloride, ArXiv Prepr. ArXiv1307.5668 (2013).
- [119] D.Y. Nadargi, A. Umar, J.D. Nadargi, S.A. Lokare, S. Akbar, I.S. Mulla, S.S. Suryavanshi, N.L. Bhandari, M.G. Chaskar, Gas sensors and factors influencing sensing mechanism with a special focus on MOS sensors, J. Mater. Sci. 58 (2023) 559–582.
- [120] A.D. Pogrebnjak, C.-H. Kong, R.F. Webster, R.D. Tilley, Y. Takeda, K. Oyoshi, O. V Bondar, V. V Buranich, S. V Konstantinov, L.S. Baimoldanova, Antibacterial effect of au implantation in ductile nanocomposite multilayer (TiAlSiY) N/CrN coatings, ACS Appl. Mater. Interfaces 11 (2019) 48540–48550.
- [121] V. Ravikumar, I. Mijakovic, S. Pandit, Antimicrobial activity of graphene oxide contributes to alteration of key stress-related and membrane bound proteins, Int. J. Nanomedicine 17 (2022) 6707.
- [122] T.D. Tavares, J.C. Antunes, J. Padrão, A.I. Ribeiro, A. Zille, M.T.P. Amorim, F. Ferreira, H.P. Felgueiras, Activity of Specialized Biomolecules against Gram-Positive and Gram-Negative Bacteria, Antibiotics 9 (2020) 314. <https://doi.org/10.3390/antibiotics9060314>.
- [123] M. autista Cases, Design and characterization of an antibacterial coating on ITO surfacesB, (2024).
- [124] M. Cacaci, C. Martini, C. Guarino, R. Torelli, F. Bugli, M. Sanguinetti, Graphene oxide coatings as tools to prevent microbial biofilm formation on medical device, Adv. Microbiol. Infect. Dis. Public Heal. Vol. 14 (2020) 21–35.

References

- [125] Z.L. Wang, Zinc oxide nanostructures: growth, properties and applications, *J. Phys. Condens. Matter* 16 (2004) R829.
- [126] J.L. Nouwen, A. van Belkum, H.A. Verbrugh, Determinants of *Staphylococcus aureus* nasal carriage, *Neth. J. Med.* 59 (2001) 126–133.
- [127] S. Rodriguez-Mozaz, M.J. Lopez de Alda, D. Barceló, Biosensors as useful tools for environmental analysis and monitoring, *Anal. Bioanal. Chem.* 386 (2006) 1025–1041.
- [128] P.A. Serra, *Biosensors, BoD–Books on Demand*, 2010.
- [129] D. Grieshaber, R. MacKenzie, J. Vörös, E. Reimhult, Electrochemical biosensors-sensor principles and architectures, *Sensors* 8 (2008) 1400–1458.
- [130] X. Wang, J. Zhou, H. Wang, Bioreceptors as the key components for electrochemical biosensing in medicine, *Cell Reports Phys. Sci.* 5 (2024).
- [131] A.J. Taylor, P. Vadgama, Analytical reviews in clinical biochemistry: the estimation of urea, *Ann. Clin. Biochem.* 29 (1992) 245–264.
- [132] J.-H. Lee, W.A. El-Said, B.-K. Oh, J.-W. Choi, Enzyme-free glucose sensor based on Au nanobouquet fabricated indium tin oxide electrode, *J. Nanosci. Nanotechnol.* 14 (2014) 8432–8438.
- [133] M. Arain, A. Nafady, Z.H. Ibupoto, S.T.H. Sherazi, T. Shaikh, H. Khan, A. Alsalmeh, A. Niaz, M. Willander, Simpler and highly sensitive enzyme-free sensing of urea via NiO nanostructures modified electrode, *RSC Adv.* 6 (2016) 39001–39006.
- [134] K.C. Nicolaou, T. Montagnon, Molecules that changed the world, *Clin. Pharmacol. Pharmacokinet.* 14 (2008).
- [135] W.K. Mahmood, T.M. Rashid, M.I. Rahmah, A.M. Jasim, M.Q. Fahem, M.S. Jabir, D.A. Abid, R.A. Majed, D.M. Awaid, H.M. Yosif, Empowering NO₂ detection: synthesis of highly responsive Au/Cu-doped iron oxide nanoparticles as gas sensors through laser ablation, *Plasmonics* (2024) 1–10.
- [136] K.I. Abdul Wahid, C. Chaker, H. Chaker, Ni-doped SnO₂ thin films for NO₂ gas sensing application, *Sensors Actuators A Phys.* 360 (2023) 114498. <https://doi.org/10.1016/j.sna.2023.114498>.

References

- [137] H.H. Bahjat, R.A. Ismail, G.M. Sulaiman, M.S. Jabir, Magnetic Field-Assisted Laser Ablation of Titanium Dioxide Nanoparticles in Water for Anti-Bacterial Applications, *J. Inorg. Organomet. Polym. Mater.* 31 (2021) 3649–3656. <https://doi.org/10.1007/s10904-021-01973-8>.
- [138] K.S. Khashan, F.A. Abdulameer, M.S. Jabir, A.A. Hadi, G.M. Sulaiman, Anticancer activity and toxicity of carbon nanoparticles produced by pulsed laser ablation of graphite in water, *Adv. Nat. Sci. Nanosci. Nanotechnol.* 11 (2020) 35010.
- [139] M.A. Jihad, F.T.M. Noori, M.S. Jabir, S. Albukhaty, F.A. AlMalki, A.A. Alyamani, Polyethylene glycol functionalized graphene oxide nanoparticles loaded with nigella sativa extract: a smart antibacterial therapeutic drug delivery system, *Molecules* 26 (2021) 3067.
- [140] M. Zlatař, D. Escalera-López, M.G. Rodríguez, T. Hrbek, C. Götz, R. Mary Joy, A. Savan, H.P. Tran, H.N. Nong, P. Pobedinskas, Standardizing OER electrocatalyst benchmarking in aqueous electrolytes: comprehensive guidelines for accelerated stress tests and backing electrodes, *ACS Catal.* 13 (2023) 15375–15392.
- [141] M.M. Radhi, H.N. Abdullah, M.S. Jabir, E.A.J. Al-Mulla, Electrochemical effect of ascorbic acid on redox current peaks of CoCl_2 in blood medium, *Nano Biomed. Eng* 9 (2017) 103–106.
- [142] S. Ravulapalli, K.T.B. Padal, B.R. Kumar, Structural and optical properties of PVP/PEO blends doped with CNTs, *Emergent Mater.* 6 (2023) 1923–1933.
- [143] M. Das, D. Sarkar, Development of room temperature ethanol sensor from polypyrrole (PPy) embedded in polyvinyl alcohol (PVA) matrix, *Polym. Bull.* 75 (2018) 3109–3125.
- [144] S. Diaham, F. Saysouk, M.-L. Locatelli, Improvement of the electrical properties of polyimide films with silicon nitride nanoparticles, in: 2017 IEEE 12th Nanotechnol. Mater. Devices Conf., IEEE, 2017: pp. 60–61.
- [145] H. Liu, B. Zhang, H. Shi, Y. Tang, K. Jiao, X. Fu, Hydrothermal synthesis of monodisperse Ag_2Se nanoparticles in the presence of PVP and KI and their application as oligonucleotide labels, *J. Mater. Chem.* 18 (2008) 2573–2580.

References

- <https://doi.org/10.1039/b719207j>.
- [146] K.M. Koczkur, S. Mourdikoudis, L. Polavarapu, S.E. Skrabalak, Polyvinylpyrrolidone (PVP) in nanoparticle synthesis, *Dalt. Trans.* 44 (2015) 17883–17905. <https://doi.org/10.1039/c5dt02964c>.
- [147] S. Bose, T. Kuila, M.E. Uddin, N.H. Kim, A.K.T. Lau, J.H. Lee, In-situ synthesis and characterization of electrically conductive polypyrrole/graphene nanocomposites, *Polymer (Guildf)*. 51 (2010) 5921–5928.
- [148] G. Sowmiya, G. Velraj, Design of hollow nanosphere structured polypyrrole/Sn and SnO₂ nanoparticles by COP approach for enhanced electron transport behavior, *J. Inorg. Organomet. Polym. Mater.* 30 (2020) 5217–5223.
- [149] Y. Srivastava, I. Loscertales, M. Marquez, T. Thorsen, Electrospinning of hollow and core/sheath nanofibers using a microfluidic manifold, *Microfluid. Nanofluidics* 4 (2008) 245–250. <https://doi.org/10.1007/s10404-007-0177-0>.
- [150] I.S. Elashmawi, E.M. Abdelrazek, A.Y. Yassin, Influence of NiCl₂/CdCl₂ as mixed filler on structural, thermal and electrical properties of PVA/PVP blend, *Br. J. Appl. Sci. Technol.* 4 (2014) 4263–4279.
- [151] N.F. Norapandi, N. Salim, K.F. Chong, N.H.A. Bakar, Structural evaluation of graphene oxide/Zinc oxide nanocomposite for corrosion mitigation, *Mater. Today Proc.* 75 (2023) 58–62.
- [152] N. Poad, S.N. Demon, M. Yahya, N. Bidin, Optical characteristics of ITO/NTCDA film for defence technology application, *Int. J. Curr. Res. Sci. Eng. Technol* 1 (2018) 262.
- [153] W. El Hotaby, H. Sherif, B. Hemdan, W. Khalil, S. Khalil, Assessment of in situ-prepared polyvinylpyrrolidone-silver nanocomposite for antimicrobial applications, *Acta Phys. Pol. A* 131 (2017) 1554–1560.
- [154] H. Vijeth, S.P. Kumar, L. Yesappa, M. Niranjana, M. Vandana, H. Devendrappa, Influence of nickel oxide nanoparticle on the structural, electrical and dielectric properties of polypyrrole nanocomposite, in: *AIP Conf. Proc.*, AIP Publishing, 2019.
- [155] S.A. Soomro, I.H. Gul, H. Naseer, S. Marwat, M. Mujahid, Improved

References

- performance of CuFe₂O₄/rGO nanohybrid as an anode material for lithium-ion batteries prepared via facile one-step method, *Curr. Nanosci.* 15 (2019) 420–429.
- [156] M. Thirumoorthi, J.T.J. Prakash, Structure, optical and electrical properties of indium tin oxide ultra thin films prepared by jet nebulizer spray pyrolysis technique, *J. Asian Ceram. Soc.* 4 (2016) 124–132.
- [157] P.W. Davis, T.S. Shilliday, Some optical properties of cadmium telluride, *Phys. Rev.* 118 (1960) 1020.
- [158] F.M. Ahmed, S.M. Hassan, Optical and AC electrical properties for polypyrrole and polypyrrole/graphene (ppy/gn) nanocomposites, *Iraqi J. Phys.* 19 (2021) 72–78.
- [159] Q.V. Thi, N.T. Tung, D. Sohn, Synthesis and characterization of graphene-polypyrrole nanocomposites applying for electromagnetic microwave absorber, *Mol. Cryst. Liq. Cryst.* 660 (2018) 128–134.
- [160] A.I. Alawi, E. Al-Bermany, R.S. Alnayli, M.M. Sabri, N.M. Ahmed, A.K.J. Albermany, Impact of SiO₂–GO hybrid nanomaterials on opto-electronic behavior for novel glass quinary (PAAm–PVP–PVA/SiO₂–GO) hybrid nanocomposite for antibacterial activity and shielding applications, *Opt. Quantum Electron.* 56 (2024) 429. <https://doi.org/10.1007/s11082-023-06070-3>.
- [161] A.P. Indolia, M.S. Gaur, Optical properties of solution grown PVDF–ZnO nanocomposite thin films, *J. Polym. Res.* 20 (2013) 1–8. <https://doi.org/10.1007/s10965-012-0043-y>.
- [162] R. Anandan, J. Rajendran, M. Piraviperumal, Synergistic Influence of the Deposition Method, Postdeposition Annealing, and Textured Substrates on the Properties of ITO Thin Films, *ACS Appl. Electron. Mater.* 4 (2022) 5506–5518. <https://doi.org/10.1021/acsaelm.2c01126>.
- [163] P. Phukan, D. Saikia, Optical and Structural Investigation of CdSe Quantum Dots Dispersed in PVA Matrix and Photovoltaic Applications, *Int. J. OfPhotoenergy* 2013 (2013). <https://doi.org/http://dx.doi.org/10.1155/2013/728280>.

References

- [164] E. Fortunati, F. Luzi, D. Puglia, R. Petrucci, J.M. Kenny, L. Torre, Processing of PLA nanocomposites with cellulose nanocrystals extracted from *Posidonia oceanica* waste: Innovative reuse of coastal plant, *Ind. Crops Prod.* 67 (2015) 439–447. <https://doi.org/10.1016/j.indcrop.2015.01.075>.
- [165] P.B. Allen, *Elementary Solid State Physics: Principles and Applications* by MA Omar, (1975).
- [166] M. Jothibas, C. Manoharan, S. Johnson Jeyakumar, P. Praveen, Study on structural and optical behaviors of In_2O_3 nanocrystals as potential candidate for optoelectronic devices, *J. Mater. Sci. Mater. Electron.* 26 (2015) 9600–9606.
- [167] M.M. Abdi, H.N.M. Ekramul Mahmud, L.C. Abdullah, A. Kassim, M. Zaki Ab. Rahman, J.L.Y. Chyi, Optical band gap and conductivity measurements of polypyrrole-chitosan composite thin films, *Chinese J. Polym. Sci.* 30 (2012) 93–100.
- [168] A.M. Kadim, K.H. Abass, A.J. Alrubaie, Structure and optical properties of Ag content polymeric blend, in: *AIP Conf. Proc.*, AIP Publishing, 2022.
- [169] M.T. Hasan, B.J. Senger, C. Ryan, M. Culp, R. Gonzalez-Rodriguez, J.L. Coffer, A. V Naumov, Optical band gap alteration of graphene oxide via ozone treatment, *Sci. Rep.* 7 (2017) 1–8.
- [170] H.A. Foster, I.B. Ditta, S. Varghese, A. Steele, Photocatalytic disinfection using titanium dioxide: spectrum and mechanism of antimicrobial activity, *Appl. Microbiol. Biotechnol.* 90 (2011) 1847–1868.
- [171] H. Liu, F. Xing, Y. Zhou, P. Yu, J. Xu, R. Luo, Z. Xiang, P. Maria, M. Liu, U. Ritz, Materials & Design Nanomaterials-based photothermal therapies for antibacterial applications, *Mater. Des.* 233 (2023) 112231. <https://doi.org/10.1016/j.matdes.2023.112231>.
- [172] S. Yougbaré, C. Mutalik, D.I. Krisnawati, H. Kristanto, A. Jazidie, M. Nuh, T.-M. Cheng, T.-R. Kuo, Nanomaterials for the photothermal killing of bacteria, *Nanomaterials* 10 (2020) 1123.
- [173] A.I. Alawi, E. Al-Bermay, Newly Fabricated Ternary PAAm-PVA-PVP Blend Polymer Doped by SiO_2 : Absorption and Dielectric Characteristics for

References

- Solar Cell Applications and Antibacterial Activity, *Silicon* 15 (2023) 5773–5789. <https://doi.org/10.1007/s12633-023-02477-5>.
- [174] A.I. Alawi, E. Al-Bermany, R.S. Alnayli, M.M. Sabri, N.M. Ahmed, A.K.J. Albermany, Impact of SiO₂–GO hybrid nanomaterials on opto-electronic behavior for novel glass quinary (PAAm–PVP–PVA/SiO₂–GO) hybrid nanocomposite for antibacterial activity and shielding applications, *Opt. Quantum Electron.* 56 (2024) 429.
- [175] S.S. Aljelawy, E. Al-Bermany, A.R. Abdulridha, Opto-electrical dielectrics and conductivity behavior of vinyl polymers reinforced with chitosan@ graphene oxide nanomaterials for optoelectronic and biological activity, *Eur. Phys. J. Plus* 140 (2025) 94.
- [176] K. Abdali, K.H. Abass, E. Al-Bermany, E.M. Al-robayi, A.M. Kadim, Morphological, Optical, Electrical Characterizations and Anti-Escherichia coli Bacterial Efficiency (AECBE) of PVA/PAAm/PEO Polymer Blend Doped with Silver NPs., *Nano Biomed. Eng.* 14 (2022).
- [177] A.K. Hassan, H. Hamidinezhad, E. Al-Bermany, Antibacterial activity and optical behavior for restoration of micro and nano dental fillers using functional graphene nanosheets with polymethyl methacrylate, *Nano Biomed. Eng.* (2024).
- [178] A.R. Blythe, D. Bloor, *Electrical properties of polymers*, Cambridge university press, 2005.
- [179] S. Jha, V. Bhavsar, K.P. Sooraj, M. Ranjan, D. Tripathi, Investigation of the effect of in-situ grown PPy on low frequency dielectric properties and other properties of PVA-PVP blend film, *J. Adv. Dielectr.* 11 (2021) 2150020.
- [180] A.A. Kareem, J.M. Hassan, H.W. Abdulallah, Effect of SiC particles on dielectrically properties of epoxy reinforcement by (bi-directional) glass fiber, *J Mat Sci Eng* 4 (2015) 1–3.
- [181] M. South, S. Ozonoff, W.M. McMahon, Repetitive behavior profiles in asperger syndrome and high-functioning autism, *J. Autism Dev. Disord.* 35 (2005) 145–158. <https://doi.org/10.1007/s10803-004-1992-8>.
- [182] A.A. Mustikasari, M. Diantoro, N. Mufti, R. Suryana, The effect of nano ZnO

References

- morphology on structure, dielectric constant, and dissipation factor of CA-nano ZnO/ITO films, *J. Neutrino J. Fis. Dan Apl.* 10 (2018) 59–68.
- [183] A.I. Alawi, E. Al-Bermany, Exploring the impact of silicon nanoparticles on polymer nanocomposites: Advancements in fabrication techniques and exciting applications in solar cells, photoelectronic, and sensors, in: *AIP Conf. Proc.*, 2025: p. 060007. <https://doi.org/10.1063/5.0254334>.
- [184] H. Hitha, S. Kuriakose, M. John, A. Jose, T. Varghese., Dependence of dielectric parameters and AC conductivity on frequency in polycrystalline NiWO₄, in: *AIP Conf. Proc.*, 2020: p. 050005. <https://doi.org/10.1063/5.0016852>.
- [185] S.S. Basha, M. Gnanakiran, B.R. Kumar, K.V. Bhadra, M. Reddy, M. Rao, Synthesis and spectral characterization on PVA/PVP: GO based blend polymer electrolytes, *Rasayan J. Chem* 10 (2017) 1159–1166.
- [186] Z.J. Kadhim, E. Al-Bermany, A.A. Shaher, N.A. Al-Ali, K. Abdali, A.N. Tuama, Probing the Physical and Antibacterial Features of SiO₂@MoS₂ Nanoparticle-Embellished PEO/Sodium Alginate/PVA Matrix for Sunscreens, Energy Storage, Food Preservation, and Unique Plasmonic Applications, *Plasmonics* (2025). <https://doi.org/10.1007/s11468-025-03055-8>.
- [187] A.A. Al-Muntaser, R.A. Pashameah, E. Alzahrani, S.A. AlSubhi, S.T. Hameed, M.A. Morsi, Graphene nanoplatelets/TiO₂ hybrid nanofiller boosted PVA/CMC blend based high performance nanocomposites for flexible energy storage applications, *J. Polym. Environ.* 31 (2023) 2534–2548.
- [188] Z.J. Kadhim, A.A. Shaher, K. Abdali, N.A. Al-Ali, E. Al-Bermany, A.N. Tuama, Insights into the Microstructure, Optical, Dielectric, and Biological Features of HA@MoS Reinforced PEO/SA Nanocomposite Films for Optoelectronics, Sunscreens, Energy Storage, and Bactericidal Applications, *J. Inorg. Organomet. Polym. Mater.* (2025). <https://doi.org/10.1007/s10904-025-03805-5>.
- [189] Y. Yan, G. Yang, J.-L. Xu, M. Zhang, C.-C. Kuo, S.-D. Wang, Conducting polymer-inorganic nanocomposite-based gas sensors: a review, *Sci. Technol. Adv. Mater.* 21 (2020) 768–786.

References

- [190] M. Bazzaoui, J.I. Martins, E. Machnikova, E.A. Bazzaoui, L. Martins, Polypyrrole films electrosynthesized on stainless steel grid from saccharinate aqueous solution and its behaviour toward acetone vapor, *Eur. Polym. J.* 43 (2007) 1347–1358.
- [191] J.Y. Zhou, J.L. Bai, H. Zhao, Z.Y. Yang, X.Y. Gu, B.Y. Huang, C.H. Zhao, L. Cairang, G.Z. Sun, Z.X. Zhang, Gas sensing enhancing mechanism via doping-induced oxygen vacancies for gas sensors based on indium tin oxide nanotubes, *Sensors Actuators B Chem.* 265 (2018) 273–284.
- [192] Y. Abbas, A.A. Hasan, Dielectric and gas sensing properties of in situ electrochemically polymerized PPy-MgO-WO₃ nanocomposite films, *Iraqi J. Sci.* (2021) 2915–2933.
- [193] S.T. Navale, A.T. Mane, M.A. Chougule, R.D. Sakhare, S.R. Nalage, V.B. Patil, Highly selective and sensitive room temperature NO₂ gas sensor based on polypyrrole thin films, *Synth. Met.* 189 (2014) 94–99.
- [194] C. Piloto, M. Notarianni, M. Shafiei, E. Taran, D. Galpaya, C. Yan, N. Motta, Highly NO₂ sensitive caesium doped graphene oxide conductometric sensors, *Beilstein J. Nanotechnol.* 5 (2014) 1073–1081.
- [195] R. Savu, M.A. Ponce, E. Joanni, P.R. Bueno, M. Castro, M. Cilense, J.A. Varela, E. Longo, Grain size effect on the electrical response of SnO₂ thin and thick film gas sensors, *Mater. Res.* 12 (2009) 83–87.
- [196] T. Alizadeh, L.H. Soltani, Reduced graphene oxide-based gas sensor array for pattern recognition of DMMP vapor, *Sensors Actuators B Chem.* 234 (2016) 361–370.
- [197] N. Karmakar, R. Fernandes, S. Jain, U. V Patil, N.G. Shimpi, N. V Bhat, D.C. Kothari, Room temperature NO₂ gas sensing properties of p-toluenesulfonic acid doped silver-polypyrrole nanocomposite, *Sensors Actuators B Chem.* 242 (2017) 118–126.
- [198] A.R. Cadore, E. Mania, A.B. Alencar, N.P. Rezende, S. De Oliveira, K. Watanabe, T. Taniguchi, H. Chacham, L.C. Campos, R.G. Lacerda, Enhancing the response of NH₃ graphene-sensors by using devices with different graphene-substrate distances, *Sensors Actuators B Chem.* 266 (2018) 438–

References

- 446.
- [199] K. Arun, S. Sen, K.K. Sunisha, S. Sankar, M.T. Ramesan, Impact of nanosilicon on the structural, thermal and electrical behaviour of polypyrrole nanocomposites for gas sensing applications, *J. Inorg. Organomet. Polym. Mater.* 34 (2024) 2190–2202.
- [200] S.S. Al-Abbas, R.A. Ghazi, A.K. Al-shammari, N.R. Aldulaimi, A.R. Abdulridha, S.H. Al-Nesrawy, E. Al-Bermany, Influence of the polymer molecular weights on the electrical properties of Poly (vinyl alcohol)–Poly (ethylene glycols)/Graphene oxide nanocomposites, *Mater. Today Proc.* 42 (2021) 2469–2474.
- [201] E. Al-Bermany, B. Chen, Preparation and characterisation of poly(ethylene glycol)-adsorbed graphene oxide nanosheets, *Polym. Int.* 70 (2021) 341–351. <https://doi.org/10.1002/pi.6140>.
- [202] S. Sankar, M.T. Ramesan, Synthesis, characterization, conductivity, and gas-sensing performance of copolymer nanocomposites based on copper alumina and poly (aniline-co-pyrrole), *Polym. Eng. Sci.* 62 (2022) 2402–2410.
- [203] H.U. Khan, M. Tariq, M. Shah, M. Iqbal, M.T. Jan, Inquest of highly sensitive, selective and stable ammonia (NH₃) gas sensor: Structural, morphological and gas sensing properties of polyvinylpyrrolidone (PVP)/CuO nanocomposite, *Synth. Met.* 268 (2020) 116482.
- [204] 蘇平貴, Flexible NH₃ sensors fabricated by in situ self-assembly of polypyrrole, 340 (2009) 4415–19P.
- [205] A. V Almaev, V. V Kopyev, V.A. Novikov, A. V Chikiryaka, N.N. Yakovlev, A.B. Usseinov, Z.T. Karipbayev, A.T. Akilbekov, Z.K. Koishybayeva, A.I. Popov, Ito thin films for low-resistance gas sensors, *Materials (Basel)*. 16 (2022) 342.
- [206] K. Zhao, Y. Shi, M. Cui, B. Tang, C. Zheng, Q. Chen, Y. Hu, Flexible Resistive Gas Sensor Based on Molybdenum Disulfide-Modified Polypyrrole for Trace NO₂ Detection, *Polymers (Basel)*. 16 (2024) 1940.
- [207] M.A. Salam, F.H. Alsultany, E. Al-Bermany, M.M. Sabri, K. Abdali, N.M. Ahmed, E. Al-Bermany, M.M. Sabri, K. Abdali, N.M. Ahmed, Impact of

References

- graphene oxide nanosheets and polymethyl methacrylate on nano/hybrid-based restoration dental filler composites: ultrasound behavior and antibacterial activity., *J. Ultrasound* null (2024) null. <https://doi.org/10.1007/s40477-023-00855-8>.
- [208] R.M. Ahmed, E. Al-Bermamy, Tuning the optical absorption and band gap of hydrogel methylcellulose loaded using hybrid Fe₃O₄@GO nanomaterials for optoelectronic and antibacterial activity, *J. Opt.* (2024). <https://doi.org/10.1007/s12596-024-02204-2>.
- [209] T. Ahuja, D. Kumar, Recent progress in the development of nano-structured conducting polymers/nanocomposites for sensor applications, *Sensors Actuators B Chem.* 136 (2009) 275–286.
- [210] J. Chen, D.L. Officer, J.M. Pringle, D.R. MacFarlane, C.O. Too, G.G. Wallace, Photoelectrochemical solar cells based on polyterthiophenes containing porphyrins using ionic liquid electrolyte, *Electrochem. Solid-State Lett.* 8 (2005) A528.
- [211] S. Mangrio, A. Tahira, I.A. Mahar, M. Parveen, A.A. Hullio, D.A. Solangi, A. Khawaja, M.A. Bhatti, Z.A. Ibupoto, A.B. Mallah, Electrochemical non-enzymatic urea sensing using polyvinylpyrrolidone derived highly electrocatalytic NiCo₂O₄ nanowires, *J. Nanoparticle Res.* 25 (2023) 195.
- [212] W. Wu, L. Yang, S. Chen, Y. Shao, L. Jing, G. Zhao, H. Wei, Core–shell nanospherical polypyrrole/graphene oxide composites for high performance supercapacitors, *Rsc Adv.* 5 (2015) 91645–91653.
- [213] R. BOUKHERROUB, Carbon-based Materials: Application in Electrochemical Sensing, (2016).
- [214] A.N. Kozitsina, T.S. Svalova, N.N. Malysheva, A. V Okhokhonin, M.B. Vidrevich, K.Z. Brainina, Sensors based on bio and biomimetic receptors in medical diagnostic, environment, and food analysis, *Biosensors* 8 (2018) 35.

الخلاصة

تجذب المواد النانوية الهجينة اهتمامًا متزايدًا لقدرتها على تحسين الأداء الوظيفي للأنظمة القائمة على البوليمرات، مما يجعلها منافسًا قويًا للتطبيقات المتقدمة في مجالي الإلكترونيات والطب الحيوي. في هذه الدراسة، طُوّرت مركبات نانوية هجينة جديدة تعتمد على مصفوفة بولي فينيل بيروليدون (PVP K30) ممزوجة ببولي بايرون (PPY)، وهو بوليمر موصل، ومعرّزة بجسيمات نانوية من أكسيد الجرافين (GO) وأكسيد قصدير الإنديوم (ITO). تم تحضير عينات تحتوي على نسب بوليمر مختلفة، تمثل 90% من PVP و10% من PPY لتحسين خصائص البوليمر المخلوط، أُدخلت أولًا جسيمات نانوية من أكسيد الجرافين بنسبة 1%، ثم أُضيفت مواد نانوية هجينة تتكون من صفائح نانوية من أكسيد الجرافين وأكسيد قصدير الإنديوم بنسبة 1% لكل منهما. صُنعت هذه المركبات النانوية باستخدام تقنية صب المحلول، مع تعزيز عملية التشتت بالتحريك الميكانيكي والموجات فوق الصوتية.

دُرست العينات باستخدام العديد من التقنيات التحليلية، حيث أظهرت نتائج تحليل الأشعة تحت الحمراء لتحويل فورييه (FTIR) لأغشية العينات تفاعلات فيزيائية قوية. أظهر حيود الأشعة السينية (XRD) السلوك شبه البلوري لـ PVP، والذي تأثر بشدة بمساهمة الجسيمات النانوية. أظهرت صور المجهر الإلكتروني الماسح بالانبعاث الميداني (FESEM) سطحًا متجانسًا وتشتتًا ممتازًا للجسيمات النانوية داخل مصفوفة البوليمر. أظهرت نتائج مطيافية الأشعة فوق البنفسجية والمرئية تحسنًا كبيرًا في الامتصاصية، حيث زادت من 0.06 إلى 0.85 بعد مساهمة جسيمات GO-ITO النانوية في البوليمرات الممزوجة، مما يدل على فعالية استخدام جسيمين نانويين بدلاً من واحد. انخفضت فجوة الطاقة الضوئية بشكل ملحوظ من 3.43 إلى 1.63 إلكترون فولت للتحولات غير المباشرة المسموح بها ومن 3.21 إلى 0.62 إلكترون فولت للتحولات غير

المباشرة المحظورة. تم تحسين معامل الامتصاص، ومعامل الانكسار، ومعامل الخمود، وثابت العزل الحقيقي والخيالي، والموصلية الضوئية بإضافة جسيمات نانوية من أكسيد الانديوم والقصدير (GO-ITO) إلى البوليمرات الممزوجة. تم قياس ثابت العزل الكهربائي للتيار المتردد، والفقد، والموصلية في نطاقات ترددية مختلفة، مما كشف عن تحسينات ملحوظة. تحسن ثابت العزل الكهربائي بشكل ملحوظ من 2.16 إلى 4.63، وتحسنت الموصلية الكهربائية للتيار المتردد بشكل ملحوظ من 1.31×10^{-11} إلى 4.64×10^{-11} سيمنز لكل سنتيمتر.

يهدف هذا العمل إلى دراسة إمكانيات هذه المواد النانوية المطوّرة في ثلاثة تطبيقات رئيسية، بما في ذلك نظام استشعار لاختزال غاز الأمونيا (NH_3) وأكسدة غاز ثاني أكسيد النيتروجين (NO_2) بحساسية تصل إلى 25% بعد إضافة بوليمرات PPY الموصلة والمواد النانوية، والتي توفر مواقع امتصاص ممتازة لجزيئات الغاز. تُقدّم هذه المواد النانوية أنشطة كهروكيميائية واستشعارية واعدة لاختزال الأمونيا وأكسدة ثاني أكسيد النيتروجين، مما يُتيح تطبيقات واسعة. علاوة على ذلك، أظهرت الأغشية الصلبة المجففة جيدًا نشاطًا مضادًا للبكتيريا فائقًا، مع زيادة مناطق التثبيط بنسبة 53.8% ضد المكورات العنقودية الذهبية و46.1% ضد الإشريكية القولونية. أشارت الدراسات الكهروكيميائية قياس الفولتميتر الدوري (CV) ومطيافية المعاوقة الكهروكيميائية (EIS) إلى أن المستشعر الحيوي النانوي PVP-PPY/GO-ITO أظهر أداءً استثنائيًا في الكشف غير الإنزيمي عن اليوريا. ولوحظت استجابة واضحة بعد إضافة 0.1 مول من المذيب الحيوي لليوريا، تميز بزيادة كبيرة في تيارات الأكسدة والاختزال وانخفاض حاد في قيم المقاومة، وخاصة عند تركيز مركب نانوي يبلغ 15 ملغ/لتر. وتسلسل هذه النتائج الضوء على حداثة وتعدد وظائف المتراكبات النانوية المطورة، مما يُظهر إمكانيات قوية في الأجهزة الإلكترونية البصرية المرنة، والطلاءات المضادة

للبكتيريا، وهندسة الأنسجة، وتطبيقات الاستشعار، وتلبية الاحتياجات المجتمعية الحالية في القطاعات الصحية والبيئية والطبية.



جمهورية العراق
وزارة التعليم العالي والبحث العلمي
جامعة بابل
كلية التربية للعلوم الصرفة
قسم الفيزياء

كفاءة المتراكبات النانوية الهجينة ذات أساس أكسيد الكرافين في التطبيقات الفيزيائية والبيولوجية

رسالة مقدمة

الى مجلس كلية التربية للعلوم الصرفة في جامعة بابل وهي جزء من متطلبات
نيل درجة الماجستير في التربية / الفيزياء

من قبل الطالبة

رند وليد عبد السادة حسن

بكالوريوس في الفيزياء

جامعة بابل ٢٠٢٢ م

بإشراف

أ.د إحسان ضياء جواد البيرماني

٢٠٢٥ م

١٤٤٧ هـ